

Inkjet Printed Thin films and Graphene Nanohybrid Photodetectors and Sensors

By

Brent K. Cook

Submitted to the Department of Physics and Astronomy and the Graduate
Faculty of the University of Kansas in partial fulfillment of the requirements
for the degree of Doctor of Philosophy.

Chair: Dr. Judy Wu

Dr. Hui Zhao

Dr. Wai-Lun Chan

Dr. Stephen Sanders

Dr. Jack Porter

Date Defended: April 29, 2020

The Thesis Committee for Brent K. Cook
certifies that this is the approved version of the following thesis:

Inkjet Printed Thin films and Graphene Nanohybrid Photodetectors and Sensors

Chair: Dr. Judy Wu

Date Approved: May 20, 2020

Abstract

The discovery of two-dimensional (2D) atomic materials, starting with graphene in 2004, and now including MoS₂, WS₂, and hBN, has led to great interest in their potential use in microelectronic devices. These atomic dimension materials have unique properties that differ considerably from the three-dimensional (3D) materials that currently dominate in the construction of microelectronics and are based primarily on complementary metal-oxide semiconductors (CMOS). The 2D atomic materials are typically under a nanometer in thickness, for example graphene is ~0.3 nm in thickness, while they can have lateral dimension on the order of centimeters. The atomic thickness of the 2D atomic materials results in a strong quantum confinement on the charge carriers, leading to novel electronic structures that differ fundamentally from their 3D counterparts. In graphene the carbon atoms form a periodic honeycomb lattice, which exhibits a linear energy dispersion of density of states described by a modified Dirac equation. This results in the energy band structure called a "Dirac-cone." In this configuration the conduction and valence bands meet at a "Dirac point," without having a gap between the two bands. This so-called "zero bandgap" configuration leads to a Fermi energy of graphene, that is, the highest occupied energy level of the charges, that can be continuously tuned under an electric potential from dominate positive charge carriers (holes) to negative charge carriers (electrons), enabling a bipolar conductivity. The charges in graphene are massless fermions near the Dirac point with a fermi velocity of $\sim 10^6$ m/s and, hence, graphene has an extremely high charge carrier mobility of $15000 \text{ cm}^2 \text{ V}^{-1} \text{ s}^{-1}$ at room temperature. In addition, graphene also exhibits a minimal quantum conductance and a half integer quantum hall conductance. These unique properties of graphene make it ideal to combine with nanostructures (nanostructure/graphene) to form nanohybrids for the exploration of new electronics beyond CMOS through a combination of the

quantum confinement effects in both graphene and the nanostructures. Examples of these new nanohybrids include quantum dots (QDs), nanowires (NWs), nanoparticles (NPs) or their mesoporous thin films combined with graphene.

These nanostructures act as a sensitizer for graphene such that they lend their ability to generate excitons (electron-hole pairs) through external excitation such as light. They could also generate an electric field through mechanical deformation or molecule attachment in the nanostructure. The excitons then can equivalently produce an electric gating effect on graphene. The electric gating is driven by the interface built-in electric field determined by the electronic band edge alignment of the nanostructure with graphene. This causes charge transfer of either a hole or electron across the nanostructure/graphene interface. This will leave one charge trapped in the sensitizer for an exciton lifetime of a millisecond or more, which is orders of magnitude longer than typical for larger 3D devices, which do not benefit from the charge quantum confinement. The transferred charge may make multiple trips between the source and drain electrodes in the graphene device as a result of a short transit time (t_{transit}) that is inversely related to the carrier mobility in graphene. This enables an external quantum efficiency (EQE) or “gain” up to 10^{10} in nanostructure/graphene nanohybrid devices, in contrast to the capped $\text{EQE} \leq 1$ of conventional semiconductor electronics. This thesis is motivated by the extraordinary properties of these atomic and nanoscale materials. The goal is to explore nanohybrids and their nanocomposites using QDs (ZnO QDs, PbS QDs, FeS₂ QDs), ZnO NWs and ZnO NP-network films as sensitizers for graphene. The objectives of this thesis include: (1) to achieve a control of the sensitizer morphology and nanostructure/graphene interfaces for high device performance using inkjet printing; and (2) to further develop inkjet printing for on-chip generation of the nanostructure/graphene nanohybrid devices and circuits that are multi-functional, low-cost and scalable. The ultimate goal is to achieve

nanohybrid optoelectronic devices and sensors that are high performance, flexible, wearable and self-powered.

Acknowledgments

I would like to thank my mother and grandparents who let me learn to handle things on my own. Though my family had no idea what physics was, they simply let me pursue my fascination with the topic, which I myself knew nothing about it only through chemistry and calculus did I obtain some exposure. My intention was never to get a Masters or PhD, but through always wanting learn more and taking every class that was offered I found myself led to a PhD in physics. I am truly great full, as the alternative would have been working as a MCAT instructor in physics, which would never have satisfied my urge to learn more. I initially thought that I would not be able to get a PhD in physics because I had been rejected by all the graduate schools I initially applied to during my undergraduate schooling. Looking back at my old personal statements I realize that what I wanted to learn was so vague and simplistic with no higher purpose other than fascination, I can see why I was rejected. However, over time I've learned more and now I can say that I gained far more than what I set out to achieve. I've become a little bit more self-aware having to constantly critique and work with colleagues with vastly different backgrounds and ambitions, which has opened my view of the world from international relations to geopolitics. I also learned that my drive is directly proportional to the type of people around me and my interest to the topic, which I did not expect. My goals from here are as they were before, pursue what interest me, though that seems rather naïve and simplistic I have my reasons, at least now I can do that with a broader more sophisticated view. Lastly, I would like to thank my advisor Dr. Judy Wu, Dr. Stephen Sanders, and collaborators Dr. Qingfeng Liu, Dr. Maogang Gong, Dr. Dan Ewing with the Kansas City National Security Campus for all the help and opportunities, and Dr. Redeker and Mrs. Redeker for the Redeker Fellowship that has assisted me greatly through my graduate school education.

Table of Contents

Chapter 1 Introduction	1
1.1 Current Microelectronics and Devices Beyond CMOS	1
1.2 Emerging Atomic Materials, Nanostructures and Graphene Nanohybrids.....	3
1.3 Advantages of Graphene Nanohybrids and Nanostructured Thin Films	5
1.4 Printed Thin-Films and Graphene Nanohybrid Photoconductors	11
1.5 Remaining Issues in Development of Printed Thin-Films and Graphene Nanohybrids	15
Chapter 2 Experimental.....	18
2.1 Material Synthesis	18
2.1.1 Graphene Synthesis and Cleaning/Transfer Process.....	18
2.1.2 Zinc Oxide Nanowire Hydrothermal Growth	19
2.1.3 Zinc Oxide, Lead Sulfide, and Iron Sulfide Quantum Dot Synthesis.....	19
2.1.4 Zinc Oxide and Tungsten Oxide Precursor Inks.....	21
2.2 Device Fabrication	22
2.2.1 Electrodes.....	22
2.2.2 ZnO Nanowire/Graphene Nanohybrid UV Photodetector Fabrication	23
2.2.3 Inkjet Printed ZnO and WO ₃ Precursor/Composite Ink UV Photodetector	25
2.2.4 Inkjet Printed Multiwavelength Photodetector	31
2.3 Material Characterization.....	32
2.3.1 Light Absorption of Nanostructures through Transmission Spectroscopy.....	32
2.3.2 Molecular Structure Characterized via Raman Spectroscopy	33
2.3.3 Micron Scale Morphology Observed through Scanning Electron Microscopy	33
2.3.4 Atomic Lattice Spacing Measured Through Transmission Electron Microscopy ..	34

2.3.5	Surface Topology Mapped Through Atomic Force Microscopy	34
2.3.6	Photovoltaic Characterization	34
2.3.7	ZnO Nanowires and Graphene Nanohybrid Crystallinity	35
2.3.8	Printed Highly Crystalline ZnO and ZnO/GnP and Polymorphous Structures	41
2.3.9	Crystallinity of Printed WO ₃ Films and Morphology	48
2.3.10	Graphene and Quantum Dot Nanohybrids Crystal Structures	54
Chapter 3 Inkjet Printed and Hydrothermally Grown ZnO/Graphene Nanohybrids		57
3.1	Printed Zinc Oxide Nanostructures with and without Graphene for UV Photodetectors	
	57	
3.2	Zinc Oxide Nanowires/Graphene Nanohybrid UV Photodetectors	61
3.3	ZnO Nanowire/Graphene Strain and Stress Sensor	65
Chapter 4 Inkjet Printing WO₃ and ZnO Nanocomposite Films		73
4.1	Inkjet Printing WO ₃ via Surface Texturing SiO ₂ with ZnO QDs	73
4.2	Heat Assisted Printing of WO ₃ Precursor and ZnO Precursors	79
4.3	Inkjet Printed Graphene Nanoplatelets/ZnO Precursor for UV Photodetection	81
Chapter 5 Inkjet Printing Quantum Dots on Graphene for Single and Multiwavelength Photodetectors		86
5.1	Single Quantum Quantum Dot and Graphene Photodetectors	86
5.2	Inkjet Printed Quantum Dots for Multiwavelength Pixelated Photodetection	89
Chapter 6 Conclusions and Future Work and Prospects		97
References		100

List of Figures

Figure 1.1.1 (a) the size reduction of transistor nominal feature size and gate length as a function of year and (b) and cost and lithography cost of the transistor as a function of year [3].	3
Figure 1.2.1 The different low dimensional structures derived from graphite from 0D, 1D, and 2D are shown in (a), (b), and (c), respectively [12].	4
Figure 1.2.2 In (a) is the Fermi energy below the Dirac point indicating p-type and (b) when the Fermi energy is above the Dirac point for n-type.	5
Figure 1.3.1 Diagram of graphene/nanostructure heterostructure on a substrate under a voltage bias.	7
Figure 1.3.2 (a) Bulk metal-oxide with oxygen absorbed onto the surface and (b) a nanostructure approaching the Debye length. (c) Electron multiplication from recapturing of electrons localized by oxygen.	10
Figure 1.4.1. In (a) and (b) is a depiction of the contact angle of a droplet on a hydrophobic and hydrophilic surface, respectively.	12
Figure 2.2.1 (a) Schematic of the hydrothermal solution synthesis of ZnO NWs on graphene with a seeded and seedless layer. (b) Schematic device diagram of the ZnO NW/graphene heterojunction nanohybrid UV detector, and (c) the band edge electronic structures of the graphene with respect to ZnO [60, 61].	25
Figure 2.2.2 Schematic of inkjet printing with two types of inks of (a) ZnOPr and (b) ZnOPrQDs [57].	26
Figure 2.2.3 A schematic of the inkjet printer setup and the printed WO ₃ Pr ink on the SiO ₂ surface which has coagulated are shown in (a) and (b), respectively. In (c) is the SiO ₂ surface treated with ZnO QDs for texturing followed with printing of the WO ₃ Pr ink into a continuous film. Lastly, in	

(d) the printed WO ₃ UV detector design with Au electrodes using ZnO QDs texturing layer at room-temperature (~22 °C) to 50 °C [42].	27
Figure 2.2.4 The conditions for printing WO ₃ Pr at no heating, optimal heating, and over heating are depicted in (a), (b) and (c), respectively [59].	29
Figure 2.2.5 The inkjet printed ZnO precursor/Graphene nanoplatelet ink (ZnOPrGnP) on a heated SiO ₂ /Si surface with deposited Au electrodes.	30
Figure 2.2.6 Schematic diagram of printing of ZnO (black), PbS (blue) QDs and FeS ₂ (red) NCs on graphene channels defined between two nearest neighbor Au electrodes on SiO ₂ (500 nm)/Si substrates [53].	32
Figure 2.3.1 The optical transmittance of graphene and Raman spectra with (black) and without (red) a ZnO seed layer are shown in (a) and (b), respectively [60].	37
Figure 2.3.2 The SEM images of the graphene layer without (a) and with (b) a seed layer are shown. In addition, the SEM images of ZnO NW nanowire growth on graphene on the respective layers are shown in (c, d) and (d, f). Where (c) is the ZnO NWs at a 60° tilt without a seedlayer and (e) is the top view of the respective ZnO NWs, similarly, the same tilt and magnification are shown for the ZnO NWs with a seed layer in (d) and (f) [60].	38
Figure 2.3.3 (a) Representative TEM image of a seedless grown ZnO NW. Inset is enlarged framed area at the bottom of ZnO NW. b) Representative TEM images of a seeded-grown ZnO NW. c-d) HRTEM image of the framed areas of the same ZnO NW in b) on its (c) bottom (Box A) and (d) tip stem (Box B). (e) TEM image of the root part of a seeded–grown ZnO NW and (f) HRTEM image of the framed area in (e) [60].	39
Figure 2.3.4 The TEM images of the ZnO QDs used is depicted in (a) with a histogram of their size distribution in (b) [57].	41

Figure 2.3.5 SEM images of (a)-(b) a single layer ZnO films printed from the ZnOPr ink at different magnifications, respectively; and (c)-(d) a single layer of ZnO films printed from the ZnOPrQDs ink at the scales to (a) and (b), respectively [57].	42
Figure 2.3.6 (a, c) TEM and (b, d) HRTEM images of a single layer of printed ZnO using (a, b) ZnOPr and (c, d) ZnOPrQDs inks [57].	43
Figure 2.3.7 (a) Absorption and (b) PL spectra of the printed ZnOPr and ZnOPrQDs samples [57].	44
Figure 2.3.8 The optical images for ZnO/GnP concentration can be see in (a) 0 mM, (b) 5 mM, (c) 20 mM, and (d) 30 mM concentration and there respective SEM images can be seen in (e), (f), (g) and (h) [58].	45
Figure 2.3.9 (a) Raman spectrum of the 20 mM ZnO/GnP film and (b), (c), and (d) Raman maps of graphene 2D peak for GnP/ZnO nanocomposite samples of 5 mM, 20 mM, and 30 mM GnP concentrations, respectively [58].	45
Figure 2.3.10 The Raman spectrum of ZnO at different concentrations of GnP of 5 mM, 20 mM, and 30 mM [58].	47
Figure 2.3.11 The transmission as a function of wavelength is shown for ZnO and ZnO/GnP at the different GnP concentrations of 5 mM, 20 mM and 30 mM [58].	47
Figure 2.3.12 Printing three scans of the WO ₃ Pr ink at (a) room-temperature (b) 40 °C (c) 50 °C (d) 60 °C (e) 70 °C and (f) 80 °C. The ink concentration was at a con 0.02 M [59].	48
Figure 2.3.13 SEM images of the printed films on substrates heated to (a) 40 °C, (b) 50 °C, and (c) 60 °C, respectively [59].	49

Figure 2.3.14 SEM images of WO ₃ films and optical images of their corresponding printed WO ₃ Pr films of (a) and (b) at 0.01M; (c) and (d) at 0.02M, and (e) and (f) at 0.03M. All samples have three printing scans and the 50 °C substrate temperature [59].	50
Figure 2.3.15 Three printed scans of different concentrations of WO ₃ precursor ink at (a) 0.01 M (b) 0.02 M, (c) 0.03 M with thicknesses, 100-150 nm, 150-200 nm, and 400 nm, respectively, at printing temperature of 50 °C [59].	51
Figure 2.3.16 Optical images of the WO ₃ samples printed between Au electrodes of ~ 300 μm spacing on: (a) regular SiO ₂ /Si wafer at room temperature; (b) and (c) on ZnO QDs textured SiO ₂ /Si substrates at room temperature and 50 °C, respectively; (d)-(f) are the zoom-in optical images of the same samples in (a)-(c), respectively. All samples were printed using the same printing parameters and subjected to annealing at 500 °C for 2 hours in air to form crystalline WO ₃ [42].	52
Figure 2.3.17 (a) and (b) are the SEM images after the 500 °C annealing of printed WO ₃ Pr films on ZnO QDs texturing layer at room-temperature; whereas (c) and (d) include the SEM images of WO ₃ samples through a similar process except the WO ₃ Pr printing was carried out at 50 °C. The scale bars are 1 μm in (a) and (c) and 5 μm (b) and (d) [42].	53
Figure 2.3.18 The optical transmission and the Raman spectrum for the WO ₃ /ZnO QDs layer film are depicted in (a) and (b), respectively [42].	54
Figure 2.3.19 (a) Optical absorption spectra of ZnO QDs (black), PbS QDs (blue), and FeS ₂ NCs (red). TEM images of the (b) ZnO QDs, (c) PbS QDs, and (d) FeS ₂ NCs, respectively, with their HRTEM images as the insets [53].	56
Figure 3.1.1 (a) The dark current and illuminated (UV light intensity of 0.52 mW/cm ²) current as function of the bias voltage of ZnO films printed using ZnOPr (red) and ZnOPrQDs (black) inks;	

(b) Spectral UV responsivity under a UV power of $5.84 \mu\text{W}$ as a function of voltage; (c) The photoresponsivity divided by the maximum responsivity and (d) the ratio of the photoresponsivity of ZnOPrQDs with respect to ZnOPr [57]. 58

Figure 3.1.2 (a) The ZnOPr has a rise and fall time 16 s and 14 s, and (b) the ZnOPrQDs shows a rise and fall time of 55 s and 84 s, respectively, both films were tested at a 5 V bias [57]. 59

Figure 3.1.3 In (a) is the spectral curve for the ZnO/graphene nanohybrid film and (b) the dynamic temporal response, while in (c) is the dynamic response as a function of light intensity and (d) the photocurrent and photoresponsivity as a function of light intensity [55]. 61

Figure 3.2.1 The I-V characteristics curves in dark and under illumination of UV of 340 nm wavelength and $8.98 \pm 1.56 \mu\text{W}$ power for ZnO NW/graphene nanohybrids obtained from (a) seedless (black) and seeded (red) hydrothermal growth, respectively. The spectral of seeded sample is shown in (b) and the dynamic response of the two samples are shown in (c) seedless and (d) seeded [60]. 63

Figure 3.2.2 Schematic description of the photo-induced charge doping in graphene as a consequence of photo-induced charge transfer from the ZnO NWs to graphene in the ZnO NWs/graphene nanohybrids grown in (a) the seedless process and (b) the seeded one [60]. 64

Figure 3.3.1 Schematic of pressure chamber and mechanical spring apparatus for pressure and compressive force on device are shown in (a). In (b) is a diagram of how the Dirac voltage is shifted under stress/strain of nanowires. 66

Figure 3.3.2 In (a) is the change in conductance with respect to the initial conductance ($\Delta \sigma / \sigma_0$) as a function of air pressure for ZnO NWs/Gr and ZnO film/graphene devices. In (b) is the I-V characteristic curves for different magnitude of mechanical strain with an inset showing the sensitivity of the device for the given range of forces. In (c) is the dynamic response as a function

of force with the inset showing schematic of spring apparatus and finally in (d) is a zoom in image for the rise and fall time. 68

Figure 3.3.3 (a) Schematic of spring setup for applying mechanical pressure on device, (b) schematic of how piezo-potential induced under deformation, and (c) the dynamic response under different vertical compressive forces. (d) Dynamic response and inset showing zoom in image for the measurement of rise/fall time depiction. 69

Figure 3.3.4 In (a) is the schematic of homemade bending setup and in (b) is the Dirac point shift as a consequence of bending. In (c) and (d) is the dynamic response comparison of change in current for 27 mm for up-down bending and for bending radii of 55 mm and 27 mm, respectively, with the inset showing a zoom in images for depiction of rise/fall time. In (e) is the change in current as a function of strain induced with the inset showing plot of change in current as a function of bending radius, while in (f) is the dynamic response for the high frequency down bending for large number of cycles. 71

Figure 3.3.5 (a) Schematic of NWs on PET/Gr substrate at no bend situation (Top) and energy diagram of graphene along with IV characteristic curve (down). Similarly, (b) Down bending schematics (c) Up bending schematics. 72

Figure 4.1.1 In (a) and (b) depict the IV curves and dynamic photoresponse of the room-temperature printed sample on ZnO QDs layer, respectively, whereas (c) and (d) include the IV curves and dynamic photoresponse of the sample printed on ZnO QDs layer at 50 °C. The incident light wavelength was 360 nm and its intensity $\sim 7.2 \pm 1.3 \mu\text{W}$ [42]. 74

Figure 4.1.2 Depicted in (a) is a printed WO_3 precursor on a ZnO QDs textured SiO_2 surface at room-temperature and (b) at 50 °C. The profile was performed by making scratches and performing a profile to obtain the approximate depth of the films [42]. 75

Figure 4.1.3 Atomic force micrograph of ZnO QDs seed layer printed on the SiO ₂ /Si substrate with surface roughness of approximately 9.39 nm [42].	76
Figure 4.1.4 Dynamic performance of WO ₃ device on ZnO QDs texture SiO ₂ wafer printed at (a) room temperature and (b) at 50 °C, respectively [42].....	76
Figure 4.1.5 The rise-time of the room-temperature surface printed device (black), and the heated printing at 50 °C (red) as a function of power [42].....	77
Figure 4.1.6 The responsivity as a function of power for room-temperature printed WO ₃ precursor sample on ZnO QDs layer is shown in (a) along with the spectral (b). Similarly, the intensity as a function of power and spectral for WO ₃ precursor ink printed on ZnO QDs layer at 50 oC is depicted in (c) and (d), respectively [42].	78
Figure 4.2.1 The current-voltage and dynamic characteristic curves for the 50 °C are shown in (a) and (b), respectively, along with the responsivity as a function of power and wavelength in (c) and (d), respectively. Note that in (a) the dark current is scaled by 1000 for clarity [59].....	79
Figure 4.3.1 (a) Photocurrent as a function of the bias voltage and (b) responsivity measured on ZnO/GnP nanocomposited films with 0, 5 mM, 20 mM and 30 mM GnP concentrations, respectively. (c) Dynamic UV photoresponse (340 nm) at a 5V bias of the same four samples in (a), and (d) the extracted rise and fall times from (c) for the four samples [58].....	82
Figure 4.3.2 Detectivity as a function of voltage of the ZnO/GnP film at different concentrations of GnP 0 mM, 5 mM, 20 mM, and 30 mM [58].	83
Figure 4.3.3 In (a) the photoresponsivity as a function of power of the ZnO/GnP nanocomposite photodetectors with 0 mM 5 mM, 20 mM and 30 mM GnP concentrations. Similarly, we have the (b) spectral photoresponse comparing the best result to pure ZnO, (c) dynamic photoresponse, and	

(d) dark current and photocurrent as a function of time before and after the UTA treatment. PMMA passivation was applied to the sample after UTA [58]. 85

Figure 5.1.1 In (a) is the device schematic for ZnO QDs printed on graphene for a graphene field-effect transistor, and (b) shows the charge transfer schematic for the device. In (c) and (d) is the ZnO QDs right after fabrication and after aging, respectively [21]. 87

Figure 5.1.2 (a) Dynamic performance of the ZnO QDs after aging (black), partial aging (red), and after fabrication (blue), and (b) is the red and blue curves zoomed in on. In (c) is the dynamic performance with the rise and fall times, and (d) the spectral curve and the transmission of the ZnO QDs [21]. 88

Figure 5.1.3 (a) photoresponsivity (solid lines) and gain (dashed lines) as a function UV light intensity at a 340 nm wavelength at different V_{sd} of 1, 5, and 10 V. (b) photoresponsivity and gain as a function of different light intensities with changing V_{sd} and (c) the D^* as a function of UV light intensity and V_{sd} [21]. 89

Figure 5.2.1 Dynamic photoresponse to light “On” and “off” on (a) ZnO-QD/graphene; (b) PbS-QD/graphene, and (c) the FeS₂-NC/graphene photoconductor channels. (d) photocurrents as a function of the bias voltage in the three channels [53]. 92

Figure 5.2.2 The photoresponsivity as a function of power is depicted in (a), (b) and (c) along with the normalized spectral curve shown in (d) [53]. 93

Figure 5.2.3 (a) Energy band edge diagram of a ZnO/PbS/Graphene tandem structure, and a graphic shown in (b). In (c) are the current-voltage characteristic curves, (d) dynamic response to 900 nm, (e) 340 nm and (f) spectral photoresponse of the tandem device from 330 – 900 nm. Inset of (f): positive photoresponse (from black to blue) at a longer wavelength illumination when only

PbS-QD layer is active and negative photoresponse at shorter wavelength (blue) illumination when both ZnO-QD and PbS-QD layers are active [53]. 96

Chapter 1

Introduction

The discussion of the current state of microelectronics and the benefits and shortcomings of complementary metal-oxide semiconductors (CMOS) will be discussed in Section 1.1, followed by a discussion of the new atomic and nanoscale materials that could improve CMOS in Section 1.2. The next section, Section 1.3, will discuss the physics advantages and structural nanoengineering required to fully optimize printed films and quantum dots (QDs). The printed films will include graphene combined with other nanomaterials through Van der Waals attraction and metal-oxide thin films. The graphene and ZnO heterostructures will also be printed, These heterostructures are useful for forming Schottky heterojunctions, which will also be discussed. Next, in Section 1.4 is a discussion on the performance of inkjet printing photodetectors and the approaches used to create these films through surface texturing, heat assisted printing, QD inks and composite inks. Lastly, in Section 1.5 discusses the issues encountered and resolved with inkjet printing precursor films and quantum dots on SiO_2/Si and graphene. This section finishes with a proposal for a future study that might help address the remaining issues for realizing practical, ink-jet nanocircuit printing.

1.1 *Current Microelectronics and Devices Beyond CMOS*

Complimentary Metal-Oxide Semiconductors (CMOS), which were first discovered in 1958 but then saw rapid incorporation into electronic devices in the early 1970's, have resulted in a dramatic reduction of the cost and size of transistors. This has led to smaller and computationally

more powerful digital electronics [1, 2]. Prior to the development of CMOS devices, the control of current in computers was performed using vacuum tubes, which were both extremely bulky and power consuming. The current control with CMOS is done by combining adjacent n-type and p-type metal-oxide semiconductors, which results in pn junctions. The combination of elemental Si and metal-oxide semiconductors has resulted in the development of metal-oxide field-effect transistors (MOSFET), which are four-contact devices with a source, drain, gate, and substrate bias. The source and drain are n-type or p-type Si and the substrate is the opposite type, which creates pn junctions. The pn junctions form an energy barrier that prevents current from flowing freely, however by applying a gate to the channel through a metal-oxide dielectric layer the energy barrier can be reduced. These devices can be constructed with spatial dimensions on the order of nanometers, and by using better lithography techniques the MOSFET size can be reduced exponentially, as shown in the log scale graph in **Figure 1.1.1a**. Ironically, the better lithography techniques results in a reduction of transistor cost but an exponential increase in fabrication cost (**Figure 1.1.1b**) [3]. CMOS at this point in time benefits from being a well matured field of technology enabling an era of smart technology, which is technology that can respond to its environment and adjust accordingly. Examples include smart phones, watches, TVs, etc. Smart devices are now being implemented in gas sensors, photodetectors, and strain and stress sensors for industry and military applications. However, CMOS sensors have limitations since they rely on a strict integrated circuit (IC) fabrication process, which has a thermal budget of approximately 450-500 °C and the compatible materials, include but are not limited to, SiO₂, SiN, Si, poly-Si, and Al [4]. Furthermore, CMOS photosensors rely on filters, cooling, and lattice matching between layers to develop the CMOS structures for specific applications. In addition, CMOS lacks conformability and flexibility to stress/strain and lacks a high sensor area. Moreover, they require

high power amplification to see the sensor signals and as a result are often very bulky sensors, which restricts their applicability.

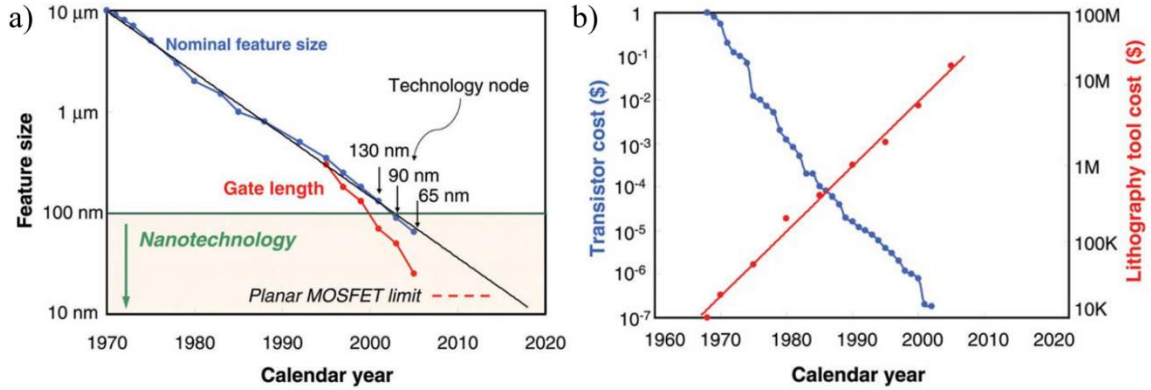


Figure 1.1.1 (a) the size reduction of transistor nominal feature size and gate length as a function of year and (b) and cost and lithography cost of the transistor as a function of year [3].

1.2 Emerging Atomic Materials, Nanostructures and Graphene Nanohybrids

Over the past couple of decades new novel materials have been discovered that can be considered 0D, 1D, and 2D materials. For example, these new materials include the bucky ball and graphene quantum dots (0D materials), nanowires and carbon nanotubes (1D materials), and MoS₂, WS₂, hBN and graphene (2D materials) [5, 6]. These novel materials offer a unique extension of CMOS in terms of sensitivity, selectivity, flexibility, and low power consumption. In the first case, 0D nanostructures such as quantum dots offer high sensitivity as a result of their large surface to volume ratio. The quantum dots also have bandgap tunability resulting from quantum charge confinement in the x-y-z axis, as well as being printable, sprayable, and drop casted [7, 8]. The 1D materials have a large aspect ratio and can be used to form carbon nanotube and nanowire meshes, nanowire wire arrays, and nanowire networks, which makes them ideal for gas sensing, flexible sensor fabrics, and photodetectors [9-11]. Lastly, the 2D materials confine charges to a plane and have thicknesses less than a nanometer. The 2D materials consist of many different types of

materials, including semi-metals (graphene) [12], insulators (hBN) [5], transition-metal dichalcogenides (WS_2 , bP) [13, 14], and semiconductors (MoS_2) [15, 16]. The 2D materials have wide applications, for example hBN is an insulator with a bandgap as wide as ~ 6 eV [5], while bP is considered a semiconductor with a bandgap of 2 eV [5, 14]. Other materials such as WS_2 and MoS_2 have shown excellent photoconductor properties in combination with graphene. Graphene, which was discovered in 2004 through mechanically cleaving graphite, is a single atomic layer of carbon atoms arranged in a honeycomb lattice that exhibits extraordinary high-charge mobility, has an extreme surface-to-volume ratio, is highly flexible, is durable, and is largely chemically inert [12]. In addition, graphite can also give rise to other nanostructures such as 0D, 1D nanostructures such as carbon bucky balls and carbon nanotubes as depicted in **Figure 1.2.1a-b**.

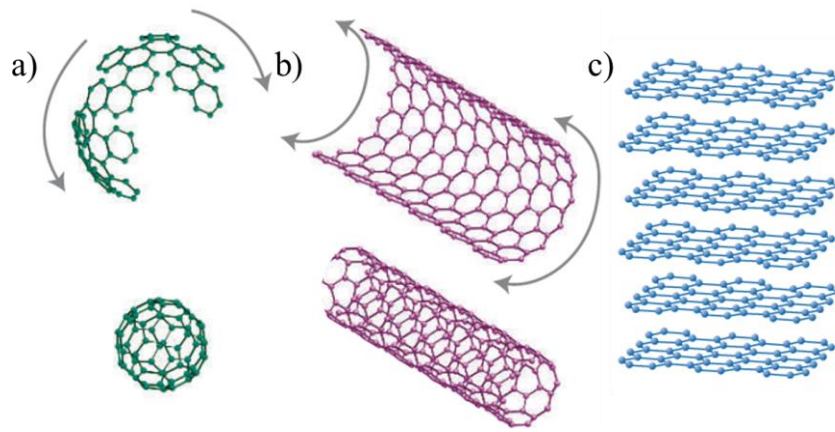


Figure 1.2.1 The different low dimensional structures derived from graphite from 0D, 1D, and 2D are shown in (a), (b), and (c), respectively [12].

Graphene on its own has unique properties that results from how the electrons interact with the single layer honeycomb lattice. This interaction with the honeycomb lattice gives rise to what is known as a Dirac cone bandgap diagram, as shown in **Figure 1.2.2**. The cone shape of the energy band band diagram has some key features. First, the conduction and valence band meet at a point called the Dirac point meaning graphene has no bandgap. Second, the Dirac point corresponds to

a neutral doping of graphene. That is, if the Fermi energy, E_f , which is the lowest occupied energy state of the electron, is below the Dirac point, then the graphene is considered to be hole-doped or p-type meaning positive charges are the dominant charge carriers (**Figure 1.2.2a**). However, if the Fermi energy is above the Dirac point the graphene is said to be n-type meaning electrons are the dominant charge carriers. Third, the atomically thin structure of graphene allows it to feel the full effect from dopants on the surface or through electrostatic doping. This allows the Fermi energy to be tuned to the Dirac point or away from it in either direction. Finally, this band structure, which results from the electron wavefunction interacting with the honeycomb lattice, results in high charge mobility. This is the greatest advantage graphene has for photoconductive gain.

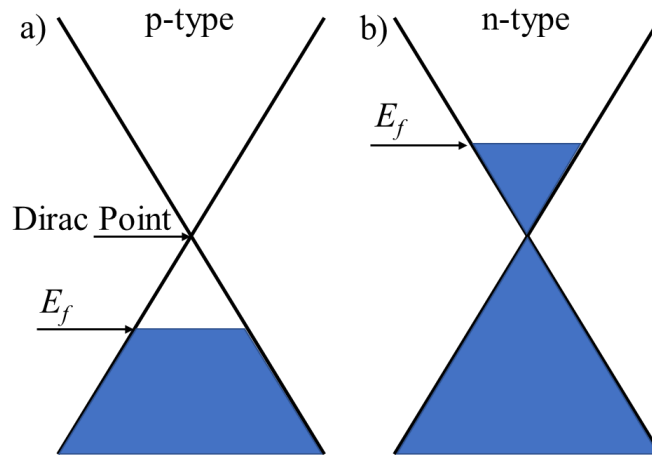


Figure 1.2.2 In (a) is the Fermi energy below the Dirac point indicating p-type and (b) when the Fermi energy is above the Dirac point for n-type.

1.3 Advantages of Graphene Nanohybrids and Nanostructured Thin Films

The graphene nanohybrids and nanoscale dimensions of semiconductors of metal-oxides, such as ZnO and WO₃, take advantage of the high charge mobility of graphene, long exciton lifetime caused by charge confinement, and surface charge depletion effect. In the case of graphene, the

charge mobility is approximately $10,000 \text{ cm}^2 \cdot \text{V}^{-1} \cdot \text{s}^{-1}$, which is an order of magnitude greater silicon ($1,400 \text{ cm}^2 \cdot \text{V}^{-1} \cdot \text{s}^{-1}$) [12, 17, 18] and five orders of magnitude better than found for ZnO ($\sim 0.2\text{-}6 \text{ cm}^2 \cdot \text{V}^{-1} \cdot \text{s}^{-1}$) [19, 20]. In addition, graphene is atomically thin, which makes graphene easily doped with charges on the surface from nanostructures like QDs or nanowires (NWs). The combination of these two traits of graphene allows for a high performance graphene nanohybrid photoconductor to be obtained.

A photoconductor is a device where, under exposure to specific wavelengths of light, a change in current occurs through the conductor. This change in current is called the photocurrent, I_{ph} , and is defined as the difference of the current with the light on, I_{on} , from the current in the dark, I_{dark} . The ratio of the photocurrent to the dark current is the on/off ratio $I_{on/off}$, the equations for these quantities are given by

$$I_{on/off} = \frac{I_{on} - I_{dark}}{I_{dark}} = \frac{I_{ph}}{I_{dark}}. \quad (1)$$

The light exposure that causes this change in photocurrent has a power, P , and the photocurrent divided by the power of the light is called the photoresponsivity, R . As a result, the photoresponsivity is proportional to the photocurrent and inversely proportional to the light power as given by equation (2). The higher photoresponsivity is therefore obtained when there is a large photocurrent for a small amount of light power. From the photoresponsivity it is possible to obtain the external quantum efficiency, EQE, sometimes referred to as the gain, G , which is the number of electrons per photon obtained from the device. The EQE can be calculated by multiplying by the energy of the photon, $E_{ph} = \hbar\omega$, divided by the elementary charge, q , where \hbar and ω are Planck's constant and the frequency of the light, respectively. In addition, the gain can also be calculated by the life time, t_{life} , of the charge in the channel divided by the transit time defined, with $t_{transit} =$

$L^2/\mu V$. Here L , μ , V are the channel length, charge mobility, and voltage bias, respectively. The mobility originates from graphene, and length of the channel is the distance between the two electrodes biased by a voltage as depicted in **Figure 1.3.1**. Equation (3) shows how these quantities are related.

$$R = \frac{I_{on} - I_{dark}}{P} = \frac{I_{ph}}{P} \quad (2)$$

$$G = R \frac{\hbar\omega}{q} = \frac{t_{life}}{t_{transit}} \quad (3)$$

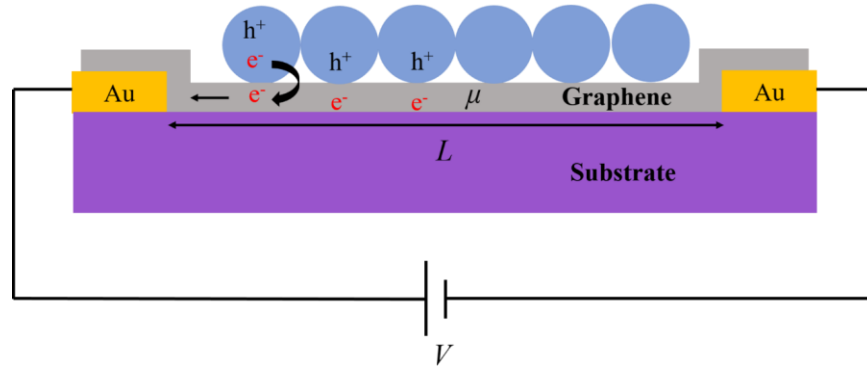


Figure 1.3.1 Diagram of graphene/nanostructure heterostructure on a substrate under a voltage bias.

The gain thus can be greatly enhanced with graphene nanohybrids by growing or depositing nanostructures or quantum dots on the surface. For example, when a photon is absorbed by a quantum dot an electron is excited from its bound state in the valence band to its free state in the conduction band, thus allowing it to contribute to the overall conductivity. The electron will transfer from the quantum dot to the graphene quantum dot interface and result in a trapped charge called a hole in the quantum dot. The hole now exerts an electric field on graphene that causes the Fermi level of graphene to change, this effect is known as electrostatic gating of graphene. Since light caused the gating of graphene it is therefore called photogating. As a result, not only did

graphene gain a charge that is now contributing to the conduction of graphene but also a gate is now being applied to graphene which further changes its conductivity and will result in a gain. This gain depends on the lifetime of the charge in the quantum dot, which usually can be on the order of a microsecond. Since the transit time in graphene can be on the order of a nanosecond, a gain on the order of 10^3 is achievable. However a larger gain can be achieved by decreasing the channel length so that the transit time can be reduced. In addition, the Fermi energy of graphene can be adjusted to the Dirac point of graphene through electric gating, which is where graphene has the lowest noise current. As a result, a large photocurrent and thus a large photoresponsivity can be obtained, this combined with the short transit time can result in a gain of up to 10^{10} . The larger photoresponsivity and low noise current are also generally used to characterize the detectivity, D^* , of the photoconductor given by

$$D^* = R \sqrt{\frac{A}{I_n^2}}, \quad (4)$$

where A , and $\overline{I_n^2}$, is the area of the channel and the noise current, respectively. The detectivity can be increased by either through low noise or a large photoresponsivity. By tuning to a low noise, a detectivity on the order $10^{14} \text{ cm} \cdot \text{Hz}^{1/2} \cdot \text{W}^{-1}$ was obtained with graphene and ZnO QDs [21]. This high detectivity that which can be obtained by solely using a low noise material such as ZnO, which can achieve detectivities of $\sim 10^{11} \text{ cm} \cdot \text{Hz}^{1/2} \cdot \text{W}^{-1}$.

In the case of ZnO or WO₃ and many other metal oxide semiconductors used as photodetectors there are alternatives for optimizing photoresponsivity and detectivity without having a graphene interface. These arise from the existence of dangling bonds that result from oxygen vacancies that are typically present in metal oxides. For example, ZnO will often loosely capture oxygen from the air by the transfer of an electron to the oxygen molecule. This results in the localization of the

electron and creates a charge depletion region in ZnO that penetrates approximately 11 nm into the material (**Figure 1.3.2a-b**). The distance at which this depletion region forms is known as the Debye length, L_D , and it is caused by the electric field of the electron. The expression for the Debye length is given by

$$L_D = \sqrt{\frac{\epsilon k_B T}{q^2 n}}, \quad (5)$$

where ϵ , k_B , T , q , and n are the dielectric constant, Boltzmann constant, temperature, elementary charge, and charge carrier concentration, respectively [22, 23]. At room temperature ZnO has a dielectric constant of approximately $\epsilon \sim 7.52 \times 10^{-11}$ F/m and $n \sim 10^{17} \text{ cm}^{-3}$, which gives a Debye length of ZnO to be approximately $L_D \sim 10$ nm. This Debye length means that ZnO nanowires and nanoparticles with a diameter on the order of 20 nm can have the entire structure charge depleted [22-24]. To recapture this localized charge there must be generated an electron-hole pair by exciting an electron in the valence band of the ZnO to the conduction band, this energy difference for photoexcitation is approximately 3.4 eV. Once the electron is excited into the conduction band it leaves behind a positively charged hole. This hole can then migrate to the surface of ZnO where it feels the electric field of the localized electron and with which it subsequently recombines (**Figure 1.3.2c**). This process results in a recaptured electron plus the generated electron and released oxygen, which means two electrons for one photon was obtained giving a gain of 200% (**Figure 1.3.2c**). Combining the electron depletion effect and the absorption of oxygen effect can result in very low dark current and, as a result, a large on/off ratio and photocurrent, which in turn gives a large photoresponsivity, gain and detectivity. For example, a nanoporous ZnO film has achieved a photoresponsivity of 383.6 A/W, as opposed to a photoresponsivity of 14.7 A/W for a regular ZnO precursor film, which will be discussed in Section 3.1.

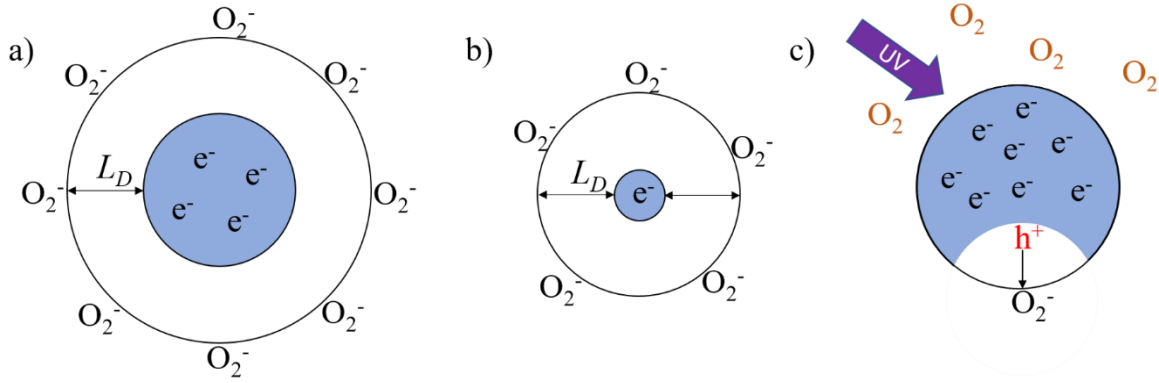


Figure 1.3.2 (a) Bulk metal-oxide with oxygen absorbed onto the surface and (b) a nanostructure approaching the Debye length. (c) Electron multiplication from recapturing of electrons localized by oxygen.

The performance of a device is also heavily affected by the graphene interface with other materials, whether it be a Schottky interface, Ohmic contact, or Van der Waals contacts and so forth. In particular, when quantum dots are placed in contact with a graphene, a Van der Waals interface forms. In this case, there is no need for lattice matching and it is the weak Coulomb interaction between the two materials that gives rise to the adhesion of the two materials. In some cases, such as with PbS QDs or FeS₂ nanoparticles, these particles are fabricated utilizing organic solutions and will result in ligands on the surface of the nanoparticle. These long ligand chains will often need to be replaced with shorter ligand chains. These shorter ligands not only provide better charge transfer between materials but also can increase the performance of Van der Waals graphene based devices by several orders of magnitude. Moreover, in the Van der Waals contact the two materials have their Fermi levels in equilibrium and can be treated independently, so they maintain their intrinsic properties with no energy band bending. The energy band bending is typically present in heterostructures of graphene with other materials, where there is strong molecular bonds resulting in a continuous energy band. For example, ZnO grown directly on graphene can result in energy band bending between the two materials. The energy band bending

between the conduction band and valence band of ZnO with the graphene has been known to form a Schottky contact between the two materials that creates energy band bending at the interface. This interface creates an upward slope in the valence band and a downward slope in the conduction band and, as a result, electron-hole pairs generated at the interface feel this energy band bending. The hole in this case will seek a high energy state and is pulled toward graphene and the electron slides down the conduction band slope away from graphene, assisting in charge separation. This assisted charge separation will allow for more charge to be separated in the bulk of the film. In addition, graphene at this point also can contribute to conduction once the film is saturated with charges, allowing for better conduction of the ZnO and graphene heterostructure film.

1.4 *Printed Thin-Films and Graphene Nanohybrid Photoconductors*

Inkjet printing offers a low cost, mass scalable, non-invasive, drop-on-demand method for integrating sensitizers with complementary-metal-oxide-semiconductors (CMOS), such as semiconductor quantum dots (QDs) [25, 26], graphene nanoflakes/quantum dots [26-28], polymers [29, 30], and many other nanostructures that can be incorporated into inks [31-35]. These materials excel at being extremely sensitive to specific wavelengths of light [36], gases [27, 37], vibrations [38], and temperature changes [30, 39] and can find application in electrochromic displays [40, 41] and touch screens [33]. This makes printing semiconductor devices and graphene nanohybrids worthy of exploration for device optimization. The physical mechanisms that can be used to optimize a photodetector were discussed in Section 1.3. However, these mechanisms do not tackle the issue of the printing process, which forces a number of constraints. To start, the ink must first be printable. How well an ink will perform can be estimated using Reynolds (N_R), Weber (N_W), and Ohnesorge (N_O) numbers

$$N_R = \frac{v\rho a}{\eta}, \quad (6)$$

$$N_W = \frac{\rho a v^2}{\gamma}, \quad (7)$$

$$N_O = \frac{(N_W)^{\frac{1}{2}}}{N_R} = \frac{\eta}{(\gamma\rho a)^{\frac{1}{2}}}, \quad (8)$$

where v , ρ , a , η , and γ are the velocity, density, drop diameter, dynamic viscosity, and surface tension, respectively [42-45]. The Reynolds number tries to characterize the inertial and viscous forces. If the Reynolds number is small then viscous flow is large. If the Reynolds number is large then inertial flow is dominant [42-44]. The Weber number relates the kinetic energy and the surface energy of the droplet. At a large Weber number value the surface tension is negligible, otherwise the surface tension becomes dominant [42-44]. The combination of the Reynolds and Weber numbers is the Ohnesorge number, which, when taking the reciprocal, gives the Z parameter ($Z = N_O^{-1}$). Typically, an ink will be too viscous if $Z < 1$, and will result in spraying if $Z > 10$ [44, 46].

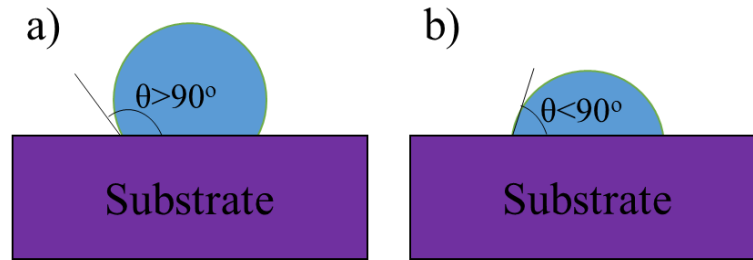


Figure 1.4.1. In (a) and (b) is a depiction of the contact angle of a droplet on a hydrophobic and hydrophilic surface, respectively.

The ink also needs to be able to spread and form a film without coagulating. One approach is to find an ink and surface that are compatible for uniform ink spread. This can be very problematic in an industrial setting where SiO_2/Si wafers are used. These are highly hydrophobic, meaning the contact angle of the ink to wafer is 90° or more (**Figure 1.4.1a**). If the contact angle less than 90° than the surface is considered hydrophilic (**Figure 1.4.1b**). To address the hydrophobicity of SiO_2 ,

pre-printing of a layer of ZnO quantum dots (QDs) on the surface of SiO₂/Si substrates to help prepare the surface for will be discussed in Section 4.1. Altering the wettability of a surface is an area of current interest [47-50]. For example, the enhanced surface roughness was reported to change the apparent contact angle [50]. The texturing of the surface with pillars or holes can also result in a hydrophobic surface [48, 49] or hydrophilic by controlling the spacing and size of the pillars and holes [47, 48]. However, surface texturing methods can be highly unpredictable. For example, the contact angle of WO₃ ink using these methods is subject to hysteresis resulting in only a 60% rate of success for printed ZnO QDs as the texturing layer on a SiO₂/Si wafer. A better method of producing a printed film with less unpredictability is to heat the substrate to a temperature that is appropriate for the ink. The heating of the substrate will allow the deposited ink to be localized on contact so that any spreading or coagulation is mitigated. Raising the temperature does, however, increase the possibility of developing a "coffee ring effect." The coffee ring effect occurs when a small amount of liquid at the ends of a droplet are more easily evaporated compared to the bulk of the ink droplet. The dried ends of the droplet then become nucleation sites for the liquid to be drawn to and continue to dry. This results in an elevated boundary with more deposited material and a flat thin center. Section 4.2 presents the results of an inkjet printed WO₃ precursor (WO₃Pr) on a heated surface. These results are compared to a textured surface solution.

A more easily printable material is formed by combining quantum dots with graphene. Using this combination, no heating is needed as the quantum dots tend to settle rather quickly to the surface of the substrate. In particular, the quantum dots printed on graphene require a clean interface for charge transfer to graphene to be efficient, because the interface is a Van der Waals contact. This means the graphene to quantum dot interface is not strongly bonded, but simply is attached through weak Coulomb interaction. The weak Coulomb bond will result in a noisy signal

or no signal and slow response times if the graphene nanoparticle interface is dirty. This problem can occur from many sources. Nanoparticles fabricated through solution processes, which is usually the case, tend to either have organics such as long chained ligands attached to the outer surface [51-53]. Alternatively, some nanoparticles will not have a long organic chain but, instead, will have an outer, unreacted shell that hinders charge transfer [21, 53]. To resolve these issues, a alternative ligand that is shorter and that does not hinder charge transfer has been used for nanoparticles like a PbS QDs and FeS₂ QDs mixtures. The deposited quantum dots on graphene were used for graphene field effect transistor (GFET), which improve the performance of the inkjet printed PbS/FeS₂ QDs mixture by over 400% from $\sim 1.2 \mu\text{A}$ to $\sim 6.4 \mu\text{A}$ [51]. Most significantly, the response times of the before and after the ligand exchange went from $\sim 452 \text{ s}$ to $\sim 15 \text{ s}$, which is an order of magnitude (30 times) improvement [51]. Similarly, FeS₂ nanocrystals (NCs) showed considerable photocurrent increase by two orders of magnitude from $0.038 \mu\text{A}$ to $1.37 \mu\text{A}$ and a response times decrease from greater than 192.5 s to 0.6 s , which is a three order of magnitude improvement [52]. An outer shell that hinders charge transfer can occur if the quantum surface is coated by an inorganic layer. This will block the charge transfer from quantum dot to graphene, as is the case with hydrothermally grown ZnO QDs [21]. This outer shell had a simpler solution of simply aging the ZnO quantum dots so that the outer shell reacts and degrades into ZnO. The aging process resulted in a negligible photocurrent to increase to a photocurrent of $\sim 2 \text{ mA}$ over time, and rise/fall times of $5.0 \text{ s}/85.1 \text{ s}$, respectively [21]. The improvement can be attributed to the better charge transfer between graphene and the quantum dots.

Other inkjet printed graphene and ZnO nanocomposites inks typically are mixture of pre-synthesized ZnO and graphene nanoflakes. These ink mixtures have photoresponsivities on the order of $\sim 10^{-2} \text{ A/W}$ and rise and fall times of $\sim 0.1 \text{ s}$ for UV photodetection, which can be attributed

to the poor interface [54]. However, printed interlinked ZnO nanoparticles (NPs) on top of graphene instead of a composite mixture can achieve a photoresponsivity of up to 5.0×10^3 A/W at a wavelength of 340 nm with a rise/decay time of 25 s/23 s, respectively [55]. In the infrared there have been sandwich structure graphene/PbS QDs/graphene photodetectors that have shown responsivities up to 1 A/W at a wavelengths of 640 nm [56]. In addition, there have also been WS₂ photoconductors that rely on the plasmonic effect, which greatly enhances the local electromagnetic field without the need of a back gate [13]. As a result, a large gating of graphene is achieved with a photoresponsivity of 6.4 A/W, without the complicated GFET fabrication [13].

So far, these printed materials have interacted with graphene through a Coulomb bond, called a Van der Waals contact, and as a result have been subject to a very sensitive interface condition. In cases where materials are grown directly on graphene there can be a strong atomic Coulomb bond formed with graphene. The strong Coulomb bond gives rise to a very different interface. In the case of graphene and ZnO, the difference in work function of the materials, which is the amount of energy needed to free an electron from the material, results in a Schottky junction. This junction can be used to improve performance, which has been accomplished through mixing graphene flakes with ZnO precursor and then annealing the mixture. These devices have shown a photoresponsivity as high as 2.2 A/W, which is two orders of magnitude greater than the composite mixture previously mentioned.

1.5 *Remaining Issues in Development of Printed Thin-Films and Graphene Nanohybrids*

The aim of this thesis is to take advantages of the physics of graphene and nanostructures that have different properties from the large bulk materials. Developing inkjet printing combined with these new nanomaterials will allow for improved performance of the sensors developed with these

materials. The optimization of these devices uses the nanophysics of the nanomaterials, including but not limited to, charge depletion in combination with nanostructure dimensions to the Debye length, using high charge carrier mobility of graphene, ligand exchange of the nanoparticle surface ligands, and the ZnO and Schottky interface heterostructures.

In Section 2.1.2, a method for optimizing the effect of electron depletion is discussed where the ZnO NW dimensions are reduced down to the Debye length through controlling the nucleation. In addition, ZnO QDs are incorporated into the ZnO precursor resulting in a Debye length nanoporous film [57]. These nanowires and films are then grown on graphene allowing for use of the high charge mobility of graphene, and the improved performance is compared with and without graphene in Chapter 3.

Chapter 4 explores the control of the printed films. These films were kept at a thickness of approximately 200 nm through heated printing of ZnO and WO₃ precursor films or through surface texturing with quantum dots, which is discussed in Sections 2.1.4 and 2.2.3 [42, 58, 59]. The quantum dots used were synthesized through controlling the reaction times and suspended in alcohol and chloroform (Section 2.1.3) [21, 51, 53]. The ZnO and WO₃ had modest results, and therefore, graphene nanoflakes were incorporated into ZnO precursor to take advantage of the graphene properties. Incorporating graphene directly into the ink allows for a clean interface to be formed during the annealing process without the need for extensive cleaning.

Graphene is better used as a conductor so the quantum dots are instead printed on graphene directly, which is discussed in Chapter 5. However, this requires a graphene cleaning and transfer process, and the exchange of ligands on the nanoparticle surface for a better interface with graphene. This is done for PbS QDs and FeS₂ QDs so that there is better charge transfer and performance. The ZnO QDs did not require ligand exchange, instead an aging process is

implemented that allows for the surface to fully react and result in a clean ZnO surface. These quantum dots and graphene nanohybrids are used to create a singular UV photodetector and a multiwavelength photodetector, which shows promising results.

However, this is just a small step into advancing inkjet printed nanohybrid sensors with the ultimate goal of being CMOS compatible. As a result, it is useful to think beyond CMOS for other applications such as flexible substrates. Printing and optimizing sensors on a flexible surface is one of many next steps for inkjet printing of novel nanomaterials. This will allow for wearable sensors and curvable sensors, which have applications in bioelectronics. However, flexible polymer substrates and foil substrates have similar limitation to that of CMOS, such as, temperature restrictions, hydrophobic surfaces, and hydrophilic surfaces. The methods discussed in this thesis hopefully can offer possible solutions to printing on flexible substrates.

Chapter 2

Experimental

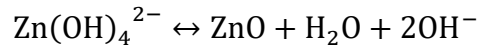
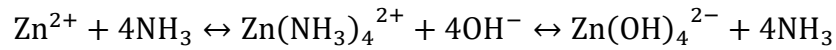
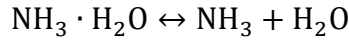
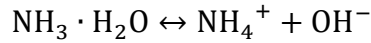
2.1 *Material Synthesis*

2.1.1 *Graphene Synthesis and Cleaning/Transfer Process*

Graphene synthesis was performed through a chemical vapor deposition method on copper foil. This is performed by passing H_2 gas through a quartz tube at 40 sccm in a furnace that is being heated to 1050 °C. Once the temperature of 1050 °C is reached the H_2 gas flow is lowered to 7 sccm and methane CH_4 is introduced at a flow rate of 40 sccm. After 30 min under CH_4 the methane flow is stopped and the furnace is turned off and the chamber is allowed to cool down under a constant flow of H_2 at 7 sccm. To transfer the graphene from the copper foil, a Poly(methyl acrylate) (PMMA) is spin coated onto the surface of the graphene/Cu foil at a rate of 3000 rpm for 1 min. and then heated on an 80 °C degree hotplate for 15 min. after which the copper is dissolved. The PMMA/graphene film is then cleaned by floating in DI water where the water is changed every 15 min. three times and then left in DI water for 24 hours so that all Cu ions diffuse from the surface of graphene. Once the PMMA/graphene film is cleaned it is then transferred graphene side down to the perspective wafer and then annealed at 120 °C for a minute or until water evaporates, after which it is allowed to naturally dry for 24 hrs. Once the drying process is finished, the PMMA is dissolved with acetone and cleaned with isopropyl alcohol and the annealed at 400 °C under H_2/Ar gas at 300/500 sccm flow rate, respectively, for 15 minutes and then cooled naturally to room temperature under the gas flow.

2.1.2 Zinc Oxide Nanowire Hydrothermal Growth

CVD graphene was transferred onto Si/SiO₂ wafers then placed in a growth 100 ml growth solution of an aqueous 2 – 10 mMol zinc nitrate hexahydrate solution, ammonia hydroxide is added to adjust the total pH to approximately 10-11 [60, 61]. The wafers are floated at the top of the solution and placed in an oven at 80 – 90 °C for up to 9 hours to ensure complete coverage and growth of ZnO nanowires (NWs) on the graphene surface [60, 61]. The following chemical reactions are the reaction that lead to the formation of ZnO NWs [60, 61].

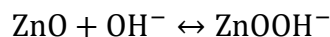
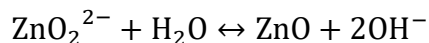
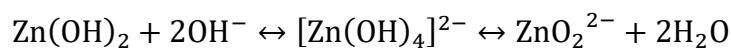
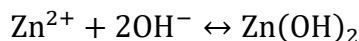


Dissolving the ammonia hydroxide into the DI water produces OH⁻ and NH₄⁺ ions that then can react with dissolved Zinc acetate in the solution producing ZnO in the last step of the reaction equations [60, 61]. Once the growth is complete the nanowires are then let to dry naturally and then annealing at 120 °C for 5 min to remove any residual water [60, 61].

2.1.3 Zinc Oxide, Lead Sulfide, and Iron Sulfide Quantum Dot Synthesis

Zinc oxide quantum dots were synthesized through solution by mixing 1.0 mmol of zinc acetate dihydrate, 10 ml of ethanol and magnetically stirred at 70 °C for an hour [21]. The mixture is then allowed to cool to room temperature while separately, a mixture of potassium hydroxide (1.7 mmol) is added to 10 ml of ethanol and sonicated for 1.0 hour [21]. The two solutions are then cooled down to 0 °C in an ice bath after which, drop by drop the potassium hydroxide mixture was added to the zinc acetate dehydrate mixture and allowed to sit in a 4 °C refrigerator for 24 hours [21]. Hexane (30 ml) was then added and centrifuged at 4000 RPM to extract the ZnO QDs from

the solution and then cleaned three times with one to one mixture of ethanol and hexane and allowed to air dry for 10 hours afterwards [21]. The ZnO QDs are then placed into ethanol for storage. The following reaction equations describe the processes to obtaining ZnO QDs [21]:



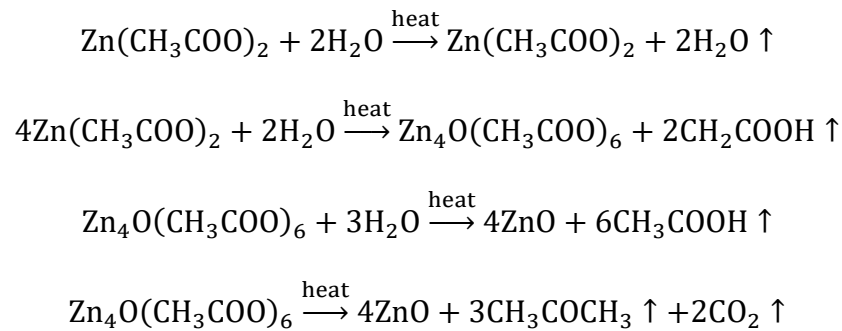
The PbS QDs were fabricated in an argon environment Schlenk line system, where 760 mg of lead(II) acetate trihydrate and 1.4 mL of oleic acid (OA) are mixed together, and then the Schlenk line system was vacuum degassed and refilled with argon three times [51]. Next 20 mL of 1-octadecen (ODE) was added and the degassing/refill process with argon was performed five times, after which the argon environment temperature is increased to 100 °C [51]. Using a separate three-neck flask, 180 mg of hexamethyldisilathiane (HMS) was added into 10 mL of ODE and then the argon degassing/refill process is performed five times while the temperature reached 100 °C [51]. The temperature was then increased to 130 °C for the lead acetate trihydrate solution, and the HMS mixture was added, and within 5 min the reaction was complete and the mixture was cooled to room temperature slowly for one hour [51]. The PbS QDs were precipitated out under centrifugation with acetone and dispersed three times with hexane and precipitated with 4:1 acetone/ethanol mixture, followed by dispersion in chloroform [51].

The FeS₂ QDs were fabricated using 63.4 mg of FeCl₂ and 12 g of octadecylamine (ODA) mixed in a three-neck flask and degassed/refilled with argon five times [51]. The mixture was decomposed for 2 hours at 120 °C while in another three-neck flask 128 mg of sulfur powder was mixed with 5 mL of diphenyl ether and sonicated for 10 min. Afterwards, it was degassed/refilled

with argon and heated to 70 °C for 1 hour until everything was dissolved [51]. The diphenyl solution was injected into the FeCl₂ solution at a temperature 120 °C [51]. Then the final mixture was raised to 220 °C for 90 min. for the reaction to take place, then the reacted solution was allowed to cool to 100 °C naturally. The reaction was terminated by injecting methanol and the FeS₂ QDs were precipitated using centrifugation [51]. The FeS₂ QDs were then cleaned with a 1:3 ratio mixture of ethanol/chloroform and centrifugation in a glovebox in a N₂ environment [51]. Afterward the QDs were dispersed in chloroform [51].

2.1.4 Zinc Oxide and Tungsten Oxide Precursor Inks

The ZnO precursor (ZnOPr) is a mixture of 0.3 M zinc acetate dihydrate, 0.3 M ethanolamine dissolved in 2-methoxyethanol and sonicated until completely dissolved usually 10 min. or longer [62]. This ink can either be used on its own, or mixed with ZnO QDs or graphene nanoplatelets (GnPs) as demonstrated later to make a composite ZnOPr/ZnO QD (ZnOPrQDs) and ZnOPr/GnP (ZnOPrGnP) composite inks. When the ZnO precursor ink is heated up on a ramp rate of 5 °C/min to 350 °C for two hours in air at atmosphere, it will decay into zinc oxide by the following chemical reactions [63]:



The tungsten oxide inks were made utilizing ammonium metatungstate ((NH₃)₆H₂W₁₂O₄₀) and a Dimethylformamide (DMF)\water mixture was used as the tungsten oxide precursor (WO₃Pr) ink, with a Z value most likely greater than 10 given that the WO₃Pr tends to have spraying and

satellite droplet formation. The Z values for the solvent were calculated assuming the ink solution is composed mainly of Dimethylformamide (DMF) and water in a 7:1 ratio and the density, viscosity and surface tension is 0.944 g/cm^3 , $0.794 \text{ mPa}\cdot\text{s}$ and 37.1 mN/m , respectively, for DMF [64, 65]. In combination with a tip diameter of $\alpha \approx 50 \text{ }\mu\text{m}$ the Z values is approximately 53, indicating the ink has high fluidity. Similarly, using 1 g/cm^3 , $0.954 \text{ mPa}\cdot\text{s}$, and 72.7 mN/m for the density, viscosity and surface tension of water a $Z \approx 63$ is obtained. Ultrasonication for 30 min. or longer was employed to generate a uniform ink. The molecular weight of ammonium metatungstate of total solution was selected at 0.01, 0.02 and 0.03 M for testing performance.

2.2 *Device Fabrication*

The instrumentation used to create the following devices consist of an e-beam evaporator for gold deposition, a Branson 1800 ultrasonicator for substrate cleaning and mixing, and a inkjet printer SonoPlot Microplotter Proto (Sonoplot) operated with SonoGuide and SonoDraw Software. The inkjet printer tips are a boron silica glass pipette stretched out using a laser puller (P-2000 Micropipette Puller System, Sutter Instrument Company), and for annealing a Lindberg furnace was utilized. Also, standard items such as a Fisher Scientific vortex mixer, A-160 gram scale, and Vacuum Oven Model 281A.

2.2.1 *Electrodes*

Gold electrodes with channel length of 0.3 mm and a width of 3 mm were deposited on SiO_2/Si wafers with an electron beam evaporator. The silicon layer of the wafers were heavily p-doped and the silicon dioxide layer ranged in thickness from 90 nm, 300 nm, and 500 nm where 90 nm

was solely utilized for field effect transistors and the thicker SiO₂ layers were used for photoconductors.

2.2.2 ZnO Nanowire/Graphene Nanohybrid UV Photodetector Fabrication

The ZnO nanowires (ZnO NWs) grown on single layer graphene were fabricated through two methods a seedless and seeded method. The graphene was used as the nucleation surface for the ZnO NW growth and is cleaned and transferred utilizing the method summarized in Section 2.1.1, followed by an addition step of acid and base treatment, with 0.1M of hydrochloric acid (HCl) and 0.1M sodium hydroxide (NaOH) for one hour each to clean the ion residues on graphene completing a graphene/Au/SiO₂/Si wafer for growing ZnO NWs [60, 61]. For ZnO NW growth in the seedless process, the sample is floated in 100 ml of an aqueous 10 mMol zinc nitrate hexahydrate with ammonia hydroxide added until the pH value was in the range of 10-11 as discussed in Section 2.1.2, with renewal of solution every 2 hours [60, 61]. For the ZnO NW growth in the seeded process, a layer of a zinc oxide seed solution was coated on the transferred graphene after the cleaning. The seed layer was composed of 0.818 g of zinc acetate, 0.25 ml of DI water and 42 ml of methanol and the mixture was ultrasonicated for 30 minutes before coating (3500 RPM for one minute) [60, 61]. Curing at 200 °C for 3 minutes was employed and the coating and curing were repeated for five times to ensure a complete coverage of graphene by the seed layer. Annealing at 350 °C for 30 minutes was adopted to promote crystallinity of ZnO in the seed layer. ZnO NW growth condition on the graphene with the seed layer was the same as that in the seedless case except a shorter growth time of 3 hours and no solution renewal [60, 61].

The two differing growth process seedless and seeded methods are illustrated schematically in **Figure 2.2.1**. the seed layer is indicated by the red layer and the two methods produce differing

morphologies, with the seeded producing vertically aligned ZnO NWs and the seedless method producing flower like ZnO NWs. In **Figure 2.2.1b**, is the photoconductor architecture and in **Figure 2.2.1b** is the relative energy band diagrams of ZnO and graphene with respect to the vacuum energy. The energy diagram shows that under photoexcitation of the electrons (red circle) from valence band to conduction band in ZnO, the electrons have a proclivity to transfer over to graphene leaving behind a hole (black circle) and obtaining a lower energy state. The efficiency of this charge transfer depends on several major factors. One is the photocarrier generation in the ZnO NWs, which is best when the ZnO NW radius is comparable to the Debye length for an optimal surface electron depletion effect as described in Section 1.3 [66, 67]. Second, a high areal coverage and density of the ZnO NWs is important as the generated photocarriers are proportional to the areal coverage/density. Finally, the ZnO NW/graphene interface plays a critical role in electron transfer from ZnO NWs to graphene, as the interface can either hinder or facilitate efficient charge transfer which in turn can diminish or enhance the photoresponse.

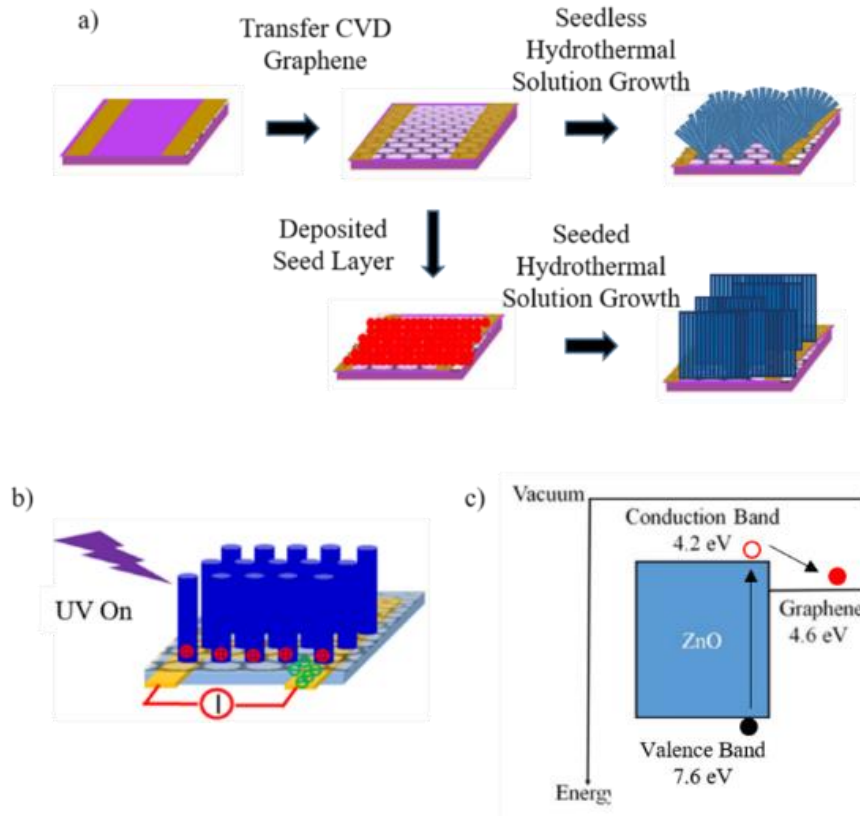


Figure 2.2.1 (a) Schematic of the hydrothermal solution synthesis of ZnO NWs on graphene with a seeded and seedless layer. (b) Schematic device diagram of the ZnO NW/graphene heterojunction nanohybrid UV detector, and (c) the band edge electronic structures of the graphene with respect to ZnO [60, 61].

2.2.3 Inkjet Printed ZnO and WO₃ Precursor/Composite Ink UV Photodetector

A SonoPlot Microplotter with a glass capillary attached to an ultrasonicated piezoelectric device for dispensing was used for sample printing on interdigitated electrodes with channel length of 100 μm where there is an e-beam deposition of Au (40 nm)/Ti (5 nm) on SiO₂ (500 nm)/Si wafer. A single layer of ZnO precursor (ZnOPr) ink and ZnO precursor with ZnO QDs (ZnOPrQDs) were printed on the interdigitated electrodes as shown in **Figure 2.2.2a** and **Figure 2.2.2b**, respectively. The ZnO QDs utilized in this experiment are synthesized using the method described in Section

2.1.3 and they are dried and then placed in the precursor and ultrasonicated for 30 minutes. The SonoPlot Microplotter is set to a dispensing voltage of 1-2 volts until a capillary bridge is formed from glass tip to substrate and then the interdigitated design is printed. Printed samples were then annealed in a furnace at 350 °C for 2 hours in air before characterization of the optoelectronic properties.

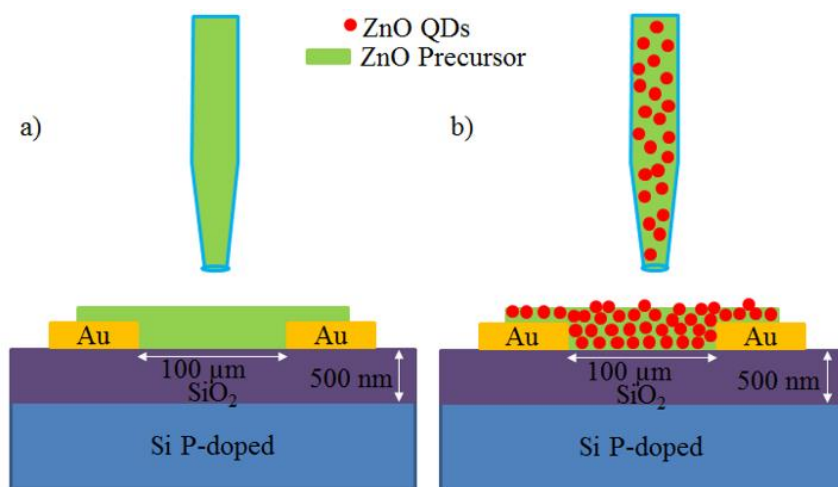


Figure 2.2.2 Schematic of inkjet printing with two types of inks of (a) ZnOPr and (b) ZnOPrQDs [57].

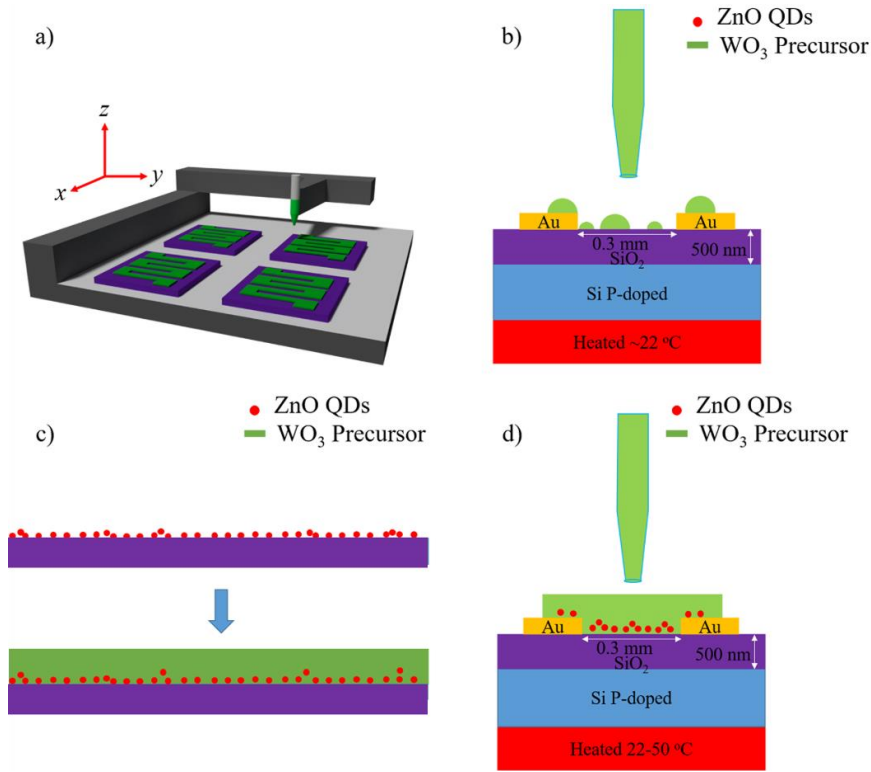


Figure 2.2.3 A schematic of the inkjet printer setup and the printed WO₃Pr ink on the SiO₂ surface which has coagulated are shown in (a) and (b), respectively. In (c) is the SiO₂ surface treated with ZnO QDs for texturing followed with printing of the WO₃Pr ink into a continuous film. Lastly, in (d) the printed WO₃ UV detector design with Au electrodes using ZnO QDs texturing layer at room-temperature (~22 °C) to 50 °C [42].

In **Figure 2.2.3a** is schematic of the printing setup and in **Figure 2.2.3b** is the tungsten oxide precursor (WO₃Pr) ink printed on a SiO₂ surface and a depiction of the results, which shows only extreme coagulation of WO₃Pr ink. To prevent this the surface is textured with ZnO QDs as shown in **Figure 2.2.3c**, in addition, one device is printed at a sample platform temperature of 22 °C (room temperature) and the other at 50 °C (**Figure 2.2.3d**). The ZnO QDs utilized are the same QDs that are fabricated in Section 2.1.3. The increased surface temperature allows for better precursor localization due to accelerated drying of liquids near the edge of the printed WO₃Pr [59]. In

Section 4.2 a study on finding an optimal temperature range for WO_3Pr was found to be at $\sim 50^\circ\text{C}$, it should be noted that the so-called coffee-ring effect was reduced but not eliminated. After printing, the dried precursor was placed into an oven in air at a temperature of 500°C for 2 hours as described in Section 2.1.4.

The WO_3Pr was also printed on a heated surface of SiO_2/Si to find optimal printing conditions that yield a high performing UV photoconductor. A homemade heater was employed as a sample platform to control the substrate temperature which was monitored by a K-type thermocouple during printing. For this experiment, the platform temperature was varied from 22°C to 80°C and a glass capillary which holds the ink undergoes a voltage sinusoidal waveform of amplitude range from 1-3 volts, usually 2.5 V is used with a frequency in range of 350 – 450 kHz, with the nozzle a distance of 20 μm from the surface. The electrodes with a channel length of 0.3 mm were fabricated using standard photolithography followed with e-beam evaporation of Au (40 nm)/Ti (5 nm) on SiO_2 (500 nm)/Si wafers before printing. The wafers were then cleaned with a spray of DI water, acetone and isopropanol and air dried with N_2 gas then treated with UV light for 30 min. prior to printing. In addition to the printing temperature and molar concentration of the ink, the number of printing scans was also varied in the range of 3 – 7 for optimal sensor thickness control. All printed samples were cured on a hotplate for 10 min. at 180°C , followed with annealing at 500°C in air for 2 hours.

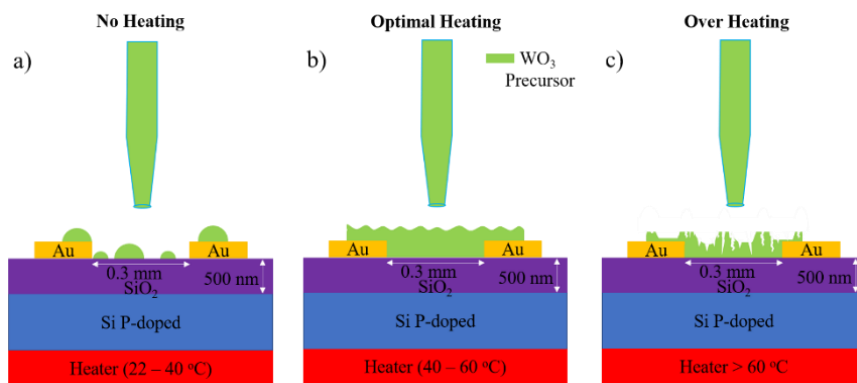


Figure 2.2.4 The conditions for printing WO₃Pr at no heating, optimal heating, and over heating are depicted in (a), (b) and (c), respectively [59].

Figure 2.2.4a illustrates the importance of the heated assisted printing of WO₃ thin films, as can be seen when the SiO₂/Si substrate was maintained at room-temperature (22 °C), the ink drops cannot spread effectively. However, at an elevated substrate temperatures of 40-80 °C, the ink droplets spread momentarily on the substrate surface to produce a continuous film as illustrated in **Figure 2.2.4b**. Qualitatively, at a higher temperature the morphology of the printed behavior becomes unpredictable, usually resulting in spraying and clogging of the ink. In addition, there are very prominent cracks that form on the peaks and frequently in the troughs between the peaks (**Figure 2.2.4c**). This is likely the result of stress and strain caused by a very uneven film due to a strong coffee ring effect.

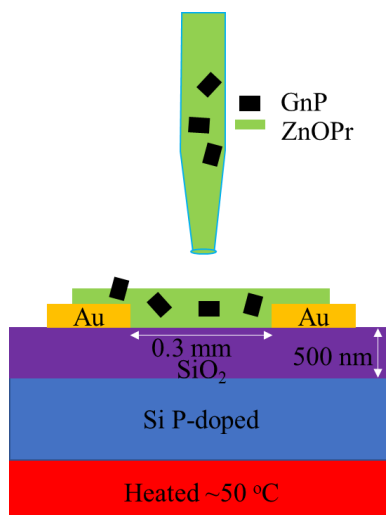


Figure 2.2.5 The inkjet printed ZnO precursor/Graphene nanoplatelet ink (ZnOPrGnP) on a heated SiO₂/Si surface with deposited Au electrodes.

The ZnO precursor ink was also used as a dispersion medium for prefabricated graphene nanoplatelet (GnP) to make a bulk heterojunction ZnO/GnP UV photodetector (**Figure 2.2.5**). The ink was obtained by mixing the GnPs into a 0.3 M ZnO precursor solution described in Section 2.1.4. The graphene nanoplatelets (5–8 nm thick, XGnP-M-5, XG Sciences) of 5 mM, 20 mM, and 30 mM concentrations were added into the ZnO sol-gel precursor solution and ultrasonicated for 1 hour until evenly dispersed throughout the solution. The gold electrodes were deposited on SiO₂/Si substrates to form a 0.3 mm x 3.0 mm effective printing area using the method in Section 2.2.1, and the substrate was heated with a hot plate to a temperature of 50 °C before printing. The inkjet glass nozzle with a nozzle diameter of ~150 μm was placed at a distance of ~20 μm from the surface so that a capillary attraction of the liquid to the substrate forms for easy dispensing. The printed area of the ink is approximately $0.40 \pm 0.1 \text{ mm}^2$ and was cured at 180 °C for 10 min after printing and the samples were annealed after using the same ZnO procedure described in Section 2.1.4. After which the samples were cooled down naturally and their optoelectronic performance were characterized immediately. Since ZnO nanostructures have a large surface area

that can be post-contaminated in air and degraded performance afterwards, some samples of long air exposure were treated with the ultrafast thermal annealing (UTA) that turned out to be efficient to remove the surface contamination as illustrated in the comparable optoelectronic performance to that of freshly fabricated ZnO/GnP bulk heterojunction devices [62].

2.2.4 Inkjet Printed Multiwavelength Photodetector

The multiwavelength photoconductor was fabricated utilizing and the same wet transfer process of the CVD grown graphene on Cu-foil as described in Section 2.1.1. The electrodes utilized are the same electrodes fabricated with e-beam evaporation in Section 2.2.1. The SonoPlot was used with a Depending on the glass tip diameter of $136.7 \pm 20.8 \mu\text{m}$ and capillary length of $20.6 \pm 0.7 \text{ mm}$ which underwent 1-3 V piezoelectric vibration for dispensing ink. The graphene channel has channel dimensions of $0.3 \text{ mm} \times 3.0 \text{ mm}$ between the two Au electrodes. The number of printed scans of QDs inks were in the range of 10-20 to ensure uniform coverage of the graphene channel. After printing the PbS QDs and FeS₂ NCs, 3-mercaptopropionic acid (MPA) ligand exchange was performed in an N₂ environment by dipping the QD (or NC) into the MPA for 30 seconds and then allowed to dry in an N₂ environment for a few minutes then passivated with PMMA. The ligand exchange is performed to remove long organic chains that block charge transfer from the QD (or NC) to graphene which is important for obtaining high photoresponse. The ligand exchange is unnecessary for ZnO QDs since ZnO QDs surface contains no organic chains on the surface.

Figure 2.2.6 depicts schematically the three-pixelated photodetectors with the three different inkjet printed ZnO QDs (black), PbS QDs (blue), and FeS₂ (red) NCs on the different graphene channels. The thickness of the printed QD or NC layer was controlled by adjusting the number of

printing scans performed. For ZnO QDs and PbS QDs of comparable QD dimensions and ink concentrations, 10 printing scans were performed to obtain the layer thickness. Considering the FeS₂ NCs have a larger dimensions they tend to diffuse into the ligand solutions during ligand exchange process, which is likely due to the loose packing of larger nanocrystals as a result 20 printing scans was performed for FeS₂ NC. The thicknesses of the printed ZnO, PbS and FeS₂ layers are approximately $0.30 \pm 0.29 \mu\text{m}$, $0.57 \pm 0.37 \mu\text{m}$ and $0.34 \pm 0.42 \mu\text{m}$, respectively.

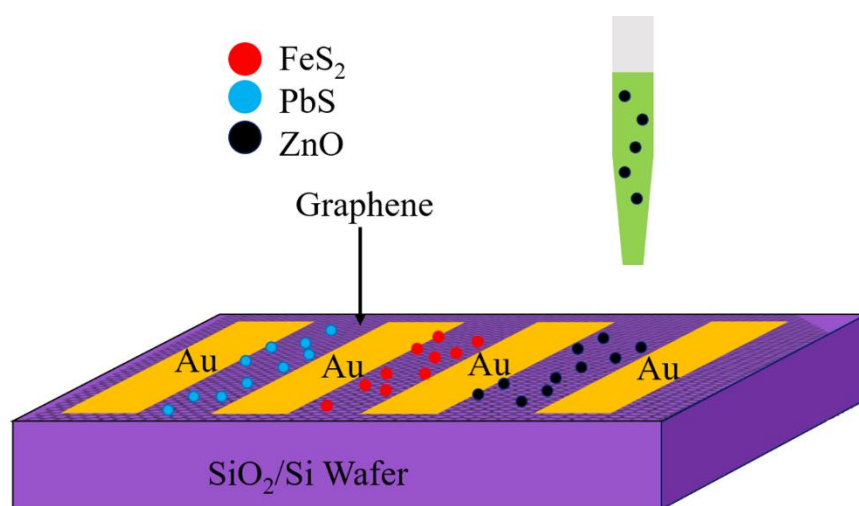


Figure 2.2.6 Schematic diagram of printing of ZnO (black), PbS (blue) QDs and FeS₂ (red) NCs on graphene channels defined between two nearest neighbor Au electrodes on SiO₂ (500 nm)/Si substrates [53].

2.3 Material Characterization

2.3.1 Light Absorption of Nanostructures through Transmission Spectroscopy

Transmission spectroscopy was taken using a UV-Vis spectrometer and through printing, spin-coating, or hydrothermally growing the material on a glass boron silicate substrate of approximately 2 mm. In this setup a light source is varied from 300 – 900 nm and is passed through the material and the amount of light transmitted with respect to the source is measured. The UV-

Vis spectrometer is calibrated in the dark to eliminate background noise and then the glass substrate with the respective material is placed in front of the light source. A second substrate is placed on a second stage that receives the same light as the material and glass substrate and is used as a reference to show the transmission of the substrate by itself without the material.

2.3.2 Molecular Structure Characterized via Raman Spectroscopy

The Raman spectrum and maps were taken using a Alpha 300 Confocal Raman, WiTec, which operates by focusing a laser beam of 480 nm onto a material, the molecular bonds of the material then interact with the light and vibrate producing a shift in the electromagnetic field emission which is then measured by the system. The samples are typically prepared on a 500 nm SiO₂/P-type Si wafer and the wavenumber range is typically measured from 0 – 3000 cm⁻¹, and 20 spectrum lines are taken at an integration time of 0.5 s and then averaged to produce a single average spectrum, however in some cases a single line spectrum is taken at 0.1 s sometimes 0.05 s integration time to produce a faster single measurement, which is usually the case for Raman maps.

2.3.3 Micron Scale Morphology Observed through Scanning Electron Microscopy

Scanning electron microscopy (SEM) was performed utilizing a JEOL JSM-6380, this machine operates by accelerating a beam of electrons onto a sample which then get reflected and are detected by respective detectors to produce an image. Samples are prepared for scanning electron microscopy on a 500 nm SiO₂/P-type Si wafer using an accelerating voltage of 30 kV and a filament current of 85 mA. Samples are then mounted onto a metallic stage with a SiO₂/Si wafer with gold nanoparticles is attached for focusing the SEM, in addition, a faraday cage is on the stage with a small 1 mm hole is used for focusing the beam into the chamber to achieve a maximum current reading insuring that the beam is centered and bombarding the substrate perpendicular to

the surface. In some cases the substrate is also tilted at a 45 to 60 ° angle, and to achieve a full 90 ° profile view a stage with a 45 ° wedge cut is utilized.

2.3.4 Atomic Lattice Spacing Measured Through Transmission Electron Microscopy

To obtain transmission electron microscopy (TEM) and a high resolution transmission electron microscopy (HRTEM) a field emission FEI Tecnai F20XT with an accelerating voltage of 200 kV is used. The sample material is scrapped off to a carbon mesh film and then images are taken at either low or high resolutions. In this instance electrons bombard a sample and pass through the sample and is then magnified onto a screen to get an image, and because of the small de Broglie wavelength of electrons the TEM is able to image much smaller features such as the crystal lattice. This measurement allows for a measurement of the lattice spacing between layers and to identify whether the material is highly crystalline, amorphous, or polymorphous.

2.3.5 Surface Topology Mapped Through Atomic Force Microscopy

The atomic force microscopy (AFM) measurements were done using the same system as the Raman the Alpha 300 Confocal Raman, WiTec. This system operates by using the laser from the Raman to deflect off of a cantilever with a tip that comes into contact with the surface of the sample. The reflected light is then measured on a photodiode to get a measure of the surface topology. This allows for the characterization of surface roughness and small measures of thin films and nanostructures.

2.3.6 Photovoltaic Characterization

The photovoltaic measurements were performed using a CHI660D electrochemical workstation with a Newport Oriel Apex monochromator and Oriel Cornerstone 140 1/8m monochromator filter in the UV–visible spectra. The filter is set to the respective wavelength and then reflected off a mirror through a retina filter then focused through a lens onto the device channel. The device is then has a source drain applied through the CHI660D electrochemical

workstation at a bias usually ranging from -5-5 volts for the current-voltage (IV) characteristics curve, this is done with the sample in the dark and in light. For the dynamic curve the same procedure is performed only this time the voltage bias is constant usually ranging from 1-5 volts and the light source is manually changed using a metallic blocker. For the intensity measurements the amount of light passed through is varied by blocking the amount of light that is reflected on the mirror and then is focused on the channel and the IV curves are measured as done previously described. Finally, for the spectral curve the monochromator filter is changed to specific wavelengths and the IV curves are taken to get the photocurrent. The power of the beam is then measured using a power meter in all cases to get the power of the light on the sample which is then used to find intensity and photoresponsivity. Lastly, the detectivity is measured through putting the sample in parallel with a resistor, a noise spectrum analyzer and a voltage source that is set to 1-5 volts and the noise voltage is measured, the known current is then used to calculate the noise current and then detectivity is calculated.

2.3.7 ZnO Nanowires and Graphene Nanohybrid Crystallinity

A discussion of the material characteristics utilized to fabricate the ZnO NW/graphene nanohybrid device will be discussed in this section. The graphene synthesis/transfer and ZnO NW hydrothermal growth can be found in Section 2.1.1 and 2.1.2, respectively, while in Section 2.2.2 was the discussion on the ZnO NW/graphene nanohybrid photodetector fabrication. To begin is the discussion on the optical transmission spectra of graphene with/without a ZnO seed layer, which is depicted in **Figure 2.3.1a** where both samples have similar behavior for wavelengths greater than 600 nm and then begin to differ at smaller wavelengths. Graphene on its own shows only small absorption at higher wavelengths, while the graphene with a ZnO seed layer begins to show optical absorption in the visible range of 370 – 600 nm indicates defects in the ZnO seed

layer, since the intrinsic bandgap of highly crystalline ZnO should only absorb wavelengths smaller than 360 nm [57, 60, 61]. In **Figure 2.3.1b** is the Raman spectra of ZnO NWs/graphene nanohybrids grown with (black) and without (red) a seed layer, were both spectra exhibit three characteristic peaks in the high frequency region, the disorder-induced defect D band at $\sim 1354\text{ cm}^{-1}$, the carbon-carbon bond G band at $\sim 1589\text{ cm}^{-1}$ derived from the in-plane vibration of the sp^2 carbon atoms, and the second-order harmonic 2D band at $\sim 2708\text{ cm}^{-1}$ which corresponds to graphene carbon ring breathing modes [60, 61]. The ratio of the 2D peak to G peak (2D/G) is approximately 3.2 and the small D peak ($\sim 1354\text{ cm}^{-1}$) indicate the transferred graphene is monolayer. The peak at $\sim 437\text{ cm}^{-1}$ derived from E2 mode of ZnO NWs, demonstrating the formation of crystalline ZnO NWs on graphene in both seedless and seeded processes [68, 69]. After coating the ZnO seed layer, both G and 2D show a red shift, which is possibly attributed to large hole-doping in graphene [70, 71].

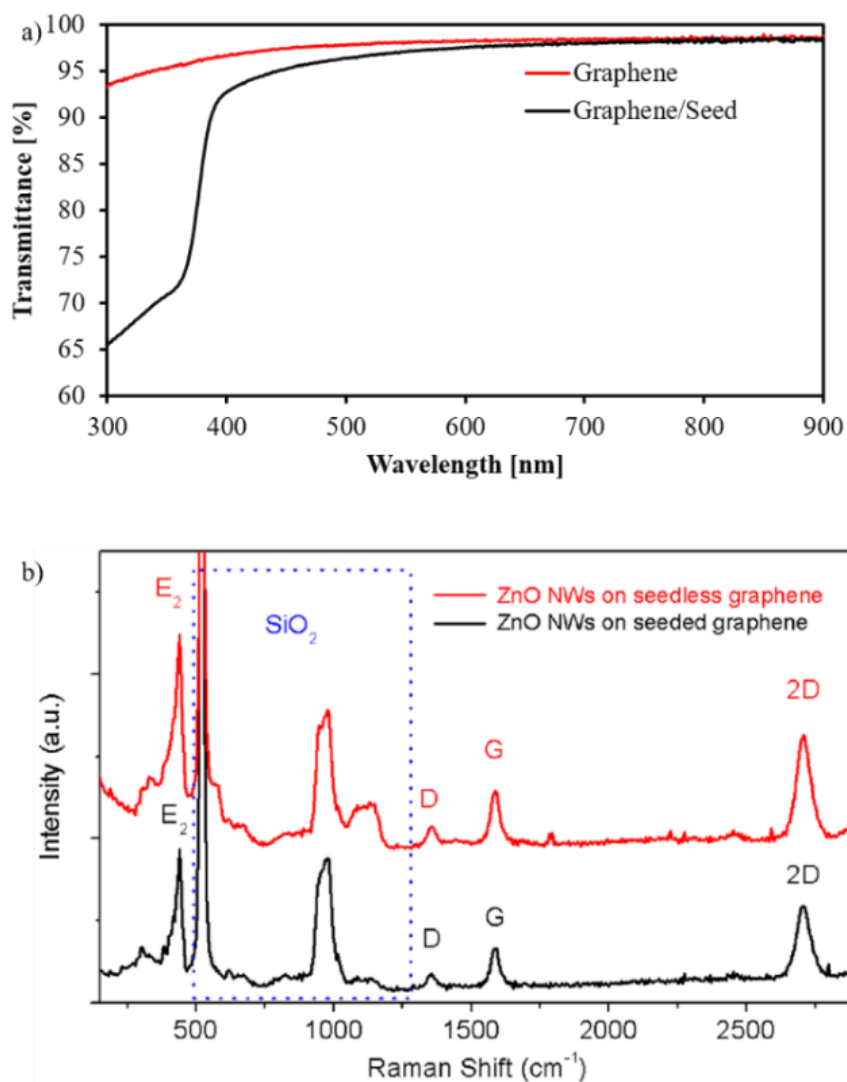


Figure 2.3.1 The optical transmittance of graphene and Raman spectra with (black) and without (red) a ZnO seed layer are shown in (a) and (b), respectively [60].

Scanning electron micrographs (SEM) at different magnifications are taken on ZnO NW/graphene nanohybrids obtained in the seedless (**Figure 2.3.2a, c, e**) and seeded (**Figure 2.3.2b, d, f**) processes. The differences in nucleation of the graphene layer from the ZnO seed produced noticeable differences in morphology, while dense ZnO NWs can be seen from both samples, they are much smaller in diameter and hence denser in the case with a seed layer. In the seedless case the nucleation is less and only defects in graphene are contributing to ZnO NW

nucleation. The ZnO seed layer plays a critical role in accelerating the nucleation and initiation of the ZnO NW growth on graphene, typically slow at a growth rate of approximately $0.63 \mu\text{m/hr}$ is observed in the seedless graphene while a much faster growth rate of $\sim 1.74 \mu\text{m/hr}$ is observed in the seedless case. It should be noted the seed layer has no effect on the morphology and growth orientation of the ZnO NWs, which are predominantly in the (0001) orientation as shown in **Figure 2.3.3**, on the other hand, the areal density of the NWs corresponds strongly with the NW diameter [61, 72]. Although the ZnO seed layer itself can form an optimal interface with graphene, this interface may become degraded and contaminated from the solution growth of ZnO NWs as suggested by the TEM and HRTEM studies in **Figure 2.3.3c-f**.

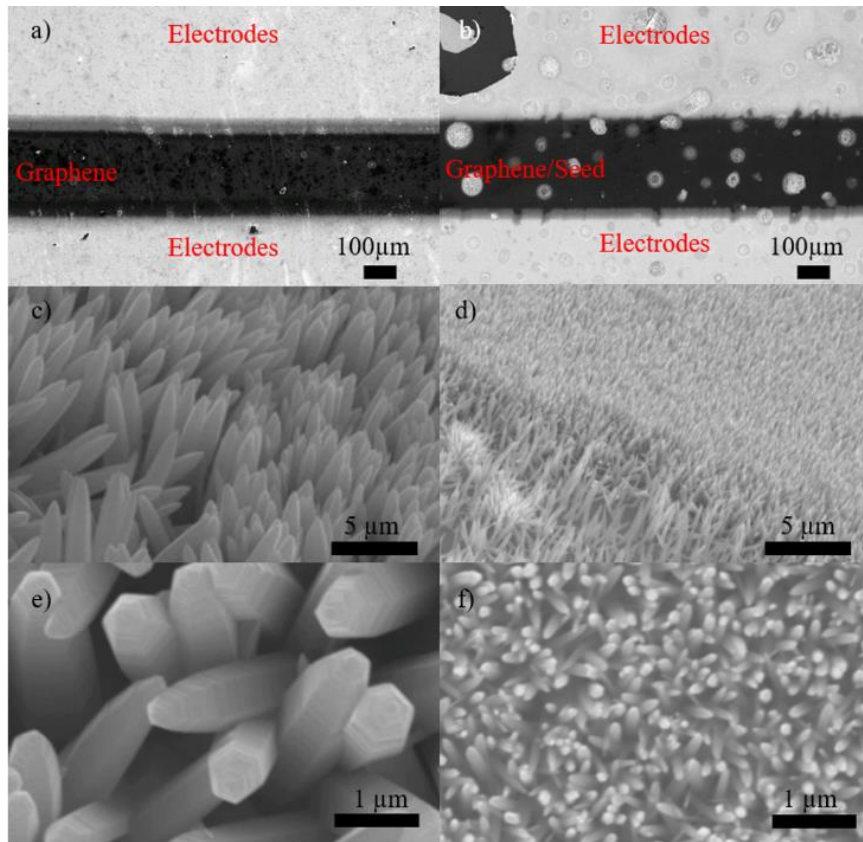


Figure 2.3.2 The SEM images of the graphene layer without (a) and with (b) a seed layer are shown. In addition, the SEM images of ZnO NW nanowire growth on graphene on the respective layers are shown in (c, d) and (d, f). Where (c) is the ZnO NWs at a 60° tilt without a seedlayer

and (e) is the top view of the respective ZnO NWs, similarly, the same tilt and magnification are shown for the ZnO NWs with a seed layer in (d) and (f) [60].

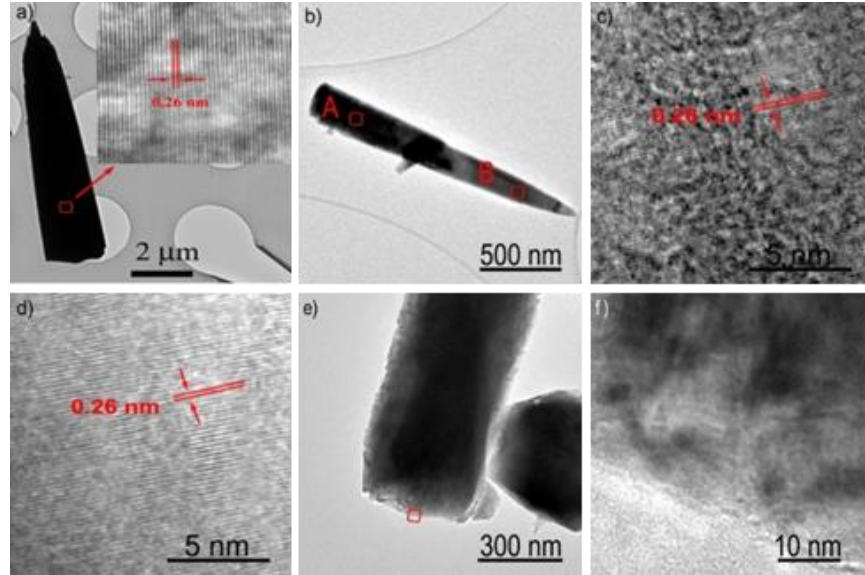


Figure 2.3.3 (a) Representative TEM image of a seedless grown ZnO NW. Inset is enlarged framed area at the bottom of ZnO NW. b) Representative TEM images of a seeded-grown ZnO NW. c-d) HRTEM image of the framed areas of the same ZnO NW in b) on its (c) bottom (Box A) and (d) tip stem (Box B). (e) TEM image of the root part of a seeded-grown ZnO NW and (f) HRTEM image of the framed area in (e) [60].

Utilizing the SEM images, an areal density of the ZnO NWs on graphene grown using both seedless and seeded processes was obtained, and the areal density was found to be approximately $1.0 \text{ NW}/\mu\text{m}^2$ and $\sim 14 \text{ NW}/\mu\text{m}^2$, respectively. The low NW areal density resulted in a flower structure, while the dense NW growth displayed nearly perpendicular alignment to the growth surface. Under the conditions specified in Section 2.1.2, the growth rate is approximately in the range of $0.63 \mu\text{m/hr}$ to $1.74 \mu\text{m/hr}$ for the seedless and seeded, respectively, and the ZnO NWs with had a length in range of $1\text{-}7 \mu\text{m}$. The length of the ZnO NWs were measured directly on ZnO

NWs/graphene by tilting the sample at an angle of 60-75 degree under SEM for a side view of the sample. For further confirmation of the ZnO NW dimensions, some were removed and transferred onto TEM grids, on which the lateral and vertical dimension of the nanowires were measured. The ZnO NWs obtained from both seedless and seeded processes have hexagonal cross sections, which is anticipated for c-axis oriented growth of ZnO NWs in the [0001] direction [61]. Considering the larger diameter at the NW stem in contrast to the smaller one at the tip on most of them, additional lateral (perpendicular to the NW axis) growth was also present in conjunction with the longitudinal growth.

Figure 2.3.3 compares the transmission electron microscopy (TEM) and high resolution TEM (HRTEM) images of the ZnO NWs fabricated using the seedless and seeded processes, respectively. The former exhibits high-quality crystalline structure with the NW axial orientation along the [0001] of ZnO. These ZnO NWs have pencil-like tips of diameters on the order of 100-500 nm and non-uniform stem diameters ranging from 100-3000 nm as shown in **Figure 2.3.3a** [61]. The ZnO NWs grown with a seed layer have similar crystalline structure (**Figure 2.3.3b**), however, the nanowire tip and stem diameter are much smaller in the ranges of 10-50 nm and 70-500 nm, respectively [61]. In addition, non-uniformity in the nanowire crystallinity can be seen in **Figure 2.3.3b-d** where the HRTEM images of the bottom and tip of the same ZnO NW are shown in **Figure 2.3.3c** and **Figure 2.3.3d**. Relatively poor crystallinity especially at the bottom of the ZnO NW has been observed, even though a [0001] direction of growth is observed with a standard lattice constant of 0.26 nm is observed, this poor crystallinity is clearly displayed in **Figure 2.3.3e** and **Figure 2.3.3f** at the root of the seeded grown ZnO NW. This observation suggests that the crystallinity of the ZnO seed layer may not be uniform as opposed to the more uniform crystallinity on the seedless-grown ZnO NWs (**Figure 2.3.3a**) [61].

2.3.8 Printed Highly Crystalline ZnO and ZnO/GnP and Polymorphous Structures

In this section will be discussed to types of inkjet printed hybrid films. The ink utilized will be the ZnO precursor (ZnOPr) discussed in Section 2.1.4 in combination with the ZnO QDs and the graphene nanoplatelets (GnPs). The devices discussed will be a ZnOPr device which produces simply a ZnO film while ZnOPr with ZnO QDs (ZnOPrQDs) and the ZnO with GnPs (ZnO/GnPs) produce a hybrid film, which their fabricated can be found in Section 2.2.3.

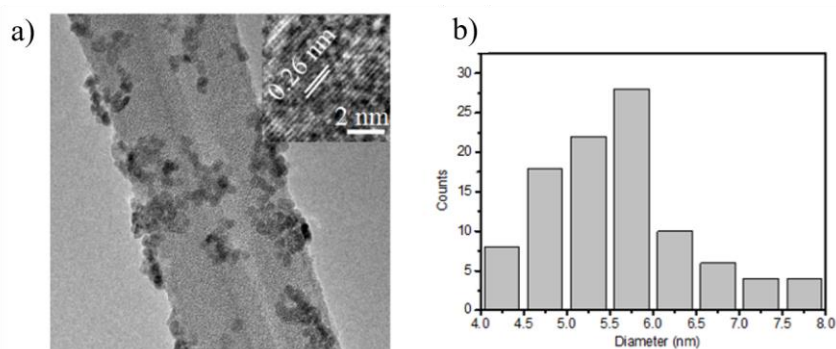


Figure 2.3.4 The TEM images of the ZnO QDs used is depicted in (a) with a histogram of their size distribution in (b) [57].

The schematic of two ZnO nanostructure photoconductor detectors printed using the ZnOPr and ZnOPrQDs are shown in **Figure 2.3.4a** and **Figure 2.3.4b**, respectively. The ZnO QDs utilized have a dimension of 5-6 nm predominately with an asymmetrical distribution extending from 4 nm to 8 nm (**Figure 2.3.4c-d**). The diameter range of the ZnO QDs an optimal feature size to fully feel the effects surface electron-depletion effect, as the ZnO QDs diameter are well below the Debye length of approximately ~11 nm, which amounts to a diameter of ~22 nm. High crystallinity can be seen with a lattice spacing of 0.26 nm expected for ZnO along the (0001) (inset **Figure 2.3.4c**) direction as previously discussed for the ZnO NWs.

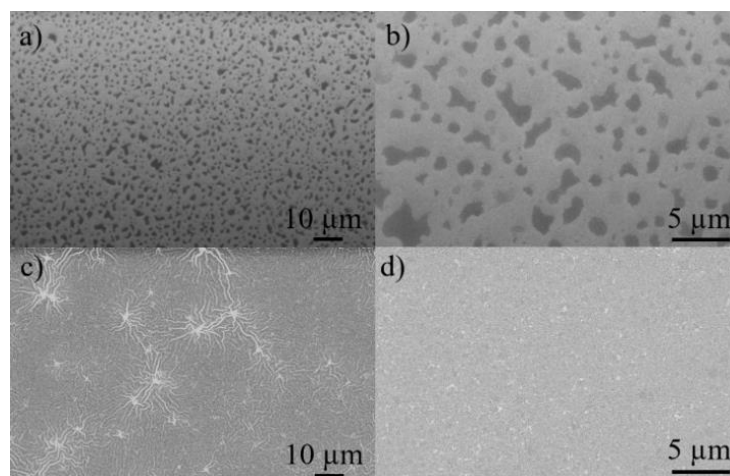


Figure 2.3.5 SEM images of (a)-(b) a single layer ZnO films printed from the ZnOPr ink at different magnifications, respectively; and (c)-(d) a single layer of ZnO films printed from the ZnOPrQDs ink at the scales to (a) and (b), respectively [57].

The morphology of two printed films the ZnOPr and ZnOPrQDs are given in **Figure 2.3.5a** and **Figure 2.3.5c**, respectively, with their increased magnification for the ZnOPr (**Figure 2.3.5b**) and ZnOPrQDs (**Figure 2.3.5d**). The ZnOPr sample shows a very rough and porous film which is likely caused by the hydrophobicity of the SiO_2 surface of the film causing coagulation and pores to form. In contrast, the ZnOPrQDs films have a complete film with what look like nucleation centers around which the precursor coagulated with the ZnO QDs (**Figure 2.3.5c**). The nucleation sites are on the order of a few microns in size, and at a close look at the film there is small dots that are probably nanoparticles with a nanoporous smooth film structure that have formed around the ZnO QDs and some ridges(**Figure 2.3.5d**).

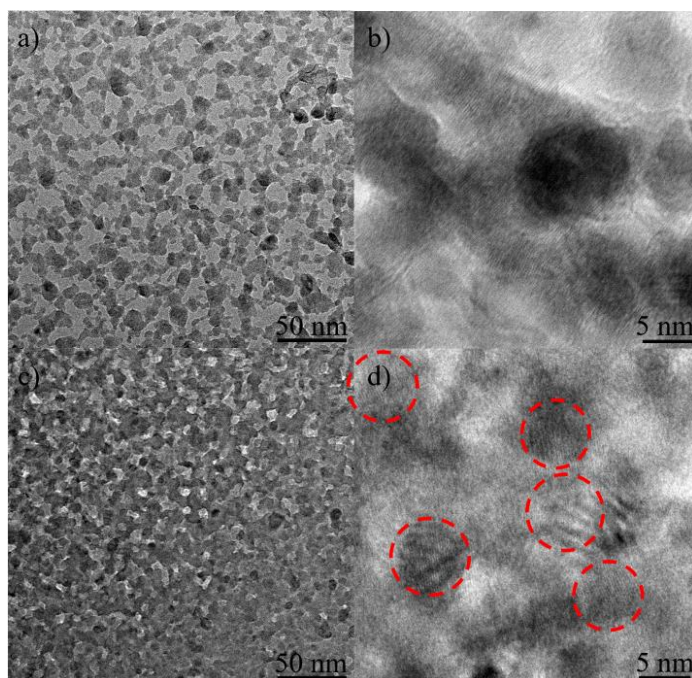


Figure 2.3.6 (a, c) TEM and (b, d) HRTEM images of a single layer of printed ZnO using (a, b) ZnOPr and (c, d) ZnOPrQDs inks [57].

The TEM and images shown in **Figure 2.3.6** are of the ZnOPr (**Figure 2.3.6a-b**) and ZnOPrQDs (**Figure 2.3.6c-d**) and clearly shows that the precursor without quantum dots (**Figure 2.3.6a**) has a more large porous morphology with less ZnO material opposed to the ZnOPrQDs film (**Figure 2.3.6b**), which has smaller pores and more material. Furthermore, the TEM images of the ZnOPr film shows large crystallites and fringe patterns that all move in similar direction (**Figure 2.3.6b**), while the ZnOPrQDs film clearly shows fringes moving in different directions which is circled red (**Figure 2.3.6d**). For further discussion on these films and their device performance can be found in Section 4.3.

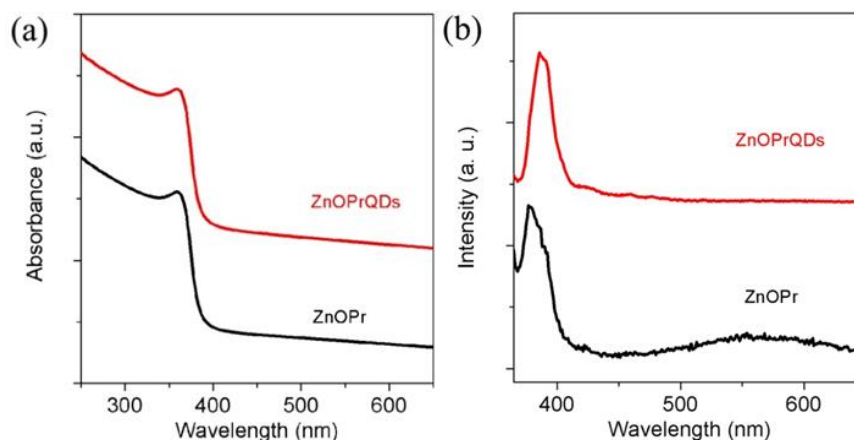


Figure 2.3.7 (a) Absorption and (b) PL spectra of the printed ZnOPr and ZnOPrQDs samples [57].

In addition the absorption spectra and the photoluminescence spectra of the ZnOPr and ZnOPrQDs can be found in **Figure 2.3.7a-b**, respectively, there can easily be seen a strong UV absorption at approximately 365 nm which corresponds to the usual ZnO bandgap of ~ 3.4 eV. In the photoluminescence (PL) spectra there is a clear UV emission at ~ 385 nm, as expected with the characteristic band-edge emission of crystalline ZnO. Compared to the ZnOPrQDs sample, which has a low and broad visible emission that is associated with the defects is detectable in the ZnOPr sample. This demonstrates that ZnO QDs also enable an improved crystallinity and surface-to-volume ratio as can be seen in the SEM and TEM results

ZnO/GnP Nanohybrid Films

The ZnO/GnP films can be seen optically in **Figure 2.3.8** the concentrations of GnP in the ZnO films was varied from 0, 5, 20, and 30 mM as shown in **Figure 2.3.8a-d**, respectively, along with the SEM below their respective images are depicted in **Figure 2.3.8e-h**. As can be seen in the ZnO/GnP films as the GnP concentration is increased there is a clear increase in darkened features due to the clumping of the GnPs. The feature sizes remain relatively the same for the 5 mM and

20 mM of $3 - 4 \mu\text{m}$, while there are a few larger ones of $5 - 7 \mu\text{m}$ in the latter, and the clumping significantly increases to $6 - 12 \mu\text{m}$ in lateral dimension for the 30 mM GnP concentration.

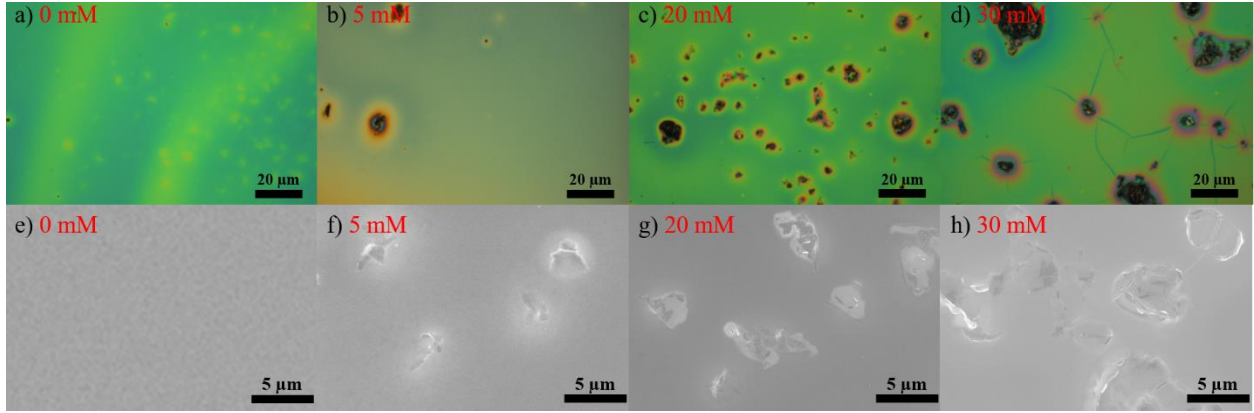


Figure 2.3.8 The optical images for ZnO/GnP concentration can be seen in (a) 0 mM, (b) 5 mM, (c) 20 mM, and (d) 30 mM concentration and there respective SEM images can be seen in (e), (f), (g) and (h) [58].

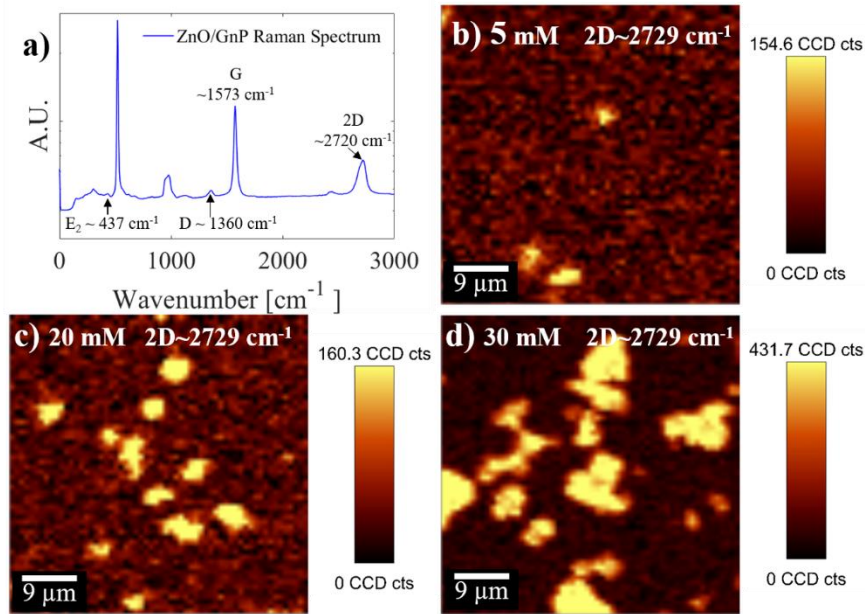


Figure 2.3.9 (a) Raman spectrum of the 20 mM ZnO/GnP film and (b), (c), and (d) Raman maps of graphene 2D peak for GnP/ZnO nanocomposite samples of 5 mM, 20 mM, and 30 mM GnP concentrations, respectively [58].

The Raman spectrum of the ZnO/GnP nanocomposite film for 20 mM GnP concentration can be seen in **Figure 2.3.9a** where the graphene peaks for the G and 2D peak can be clearly seen at approximately 1584 cm^{-1} and 2729 cm^{-1} , and the 2D/G peak ratio is approximately 0.5 indicating multilayer graphene [73-75]. Only the 20 mM GnP sample was used for simplicity and it should be noted that the differences in the Raman spectra of the ZnO/GnP nanocomposite films with the GnP concentration varied was negligible as the relative peaks all showed similar traits (**Figure 2.3.10**). Also in **Figure 2.3.9a**, it can be seen that there is a peak at 436 cm^{-1} , which is the E_2 peak associated with the c-axis of the sol-gel grown ZnO wurtzite structure being perpendicular to the substrate [69]. The other peaks similar to those seen in **Figure 2.3.1** are associated with the Si/SiO₂ wafer and the most intensive one is the peak at 520 cm^{-1} . From the Raman map in **Figure 2.3.9b-d**, there is obvious progress in GnP flake size consistent with the SEM where the dimensions range from approximately $2 - 4\text{ }\mu\text{m}$, $5 - 8\text{ }\mu\text{m}$ and $8 - 12\text{ }\mu\text{m}$ can be observed for the 5 mM, 20 mM and 30 mM GnP concentration, respectively. In addition, the areal density of GnP flakes can be observed to be 10^3 flakes/mm^2 at 5 mM of GnP up to 10^4 flakes/mm^2 at 20 mM GnP. However, the density at 30 mM does not increase, the dimension of the GnP flakes are larger compared to the 20 mM GnP concentration and have feature sizes of approximately $10.2 \pm 1.9\text{ }\mu\text{m}$, while at 20 mM the features are $5.4 \pm 1.0\text{ }\mu\text{m}$. This is twice the difference and indicates the clumping observed in the optical and SEM images. Lastly, the transmission spectrum is measured for all concentrations and shows a small decrease in the visible spectrum with an increase in GnP concentration (**Figure 2.3.11**), likely caused by small absorption/reflection, however, this effect seems unapparent in the UV range probably because of the optoelectronic process becoming dominant for ZnO in the UV range.

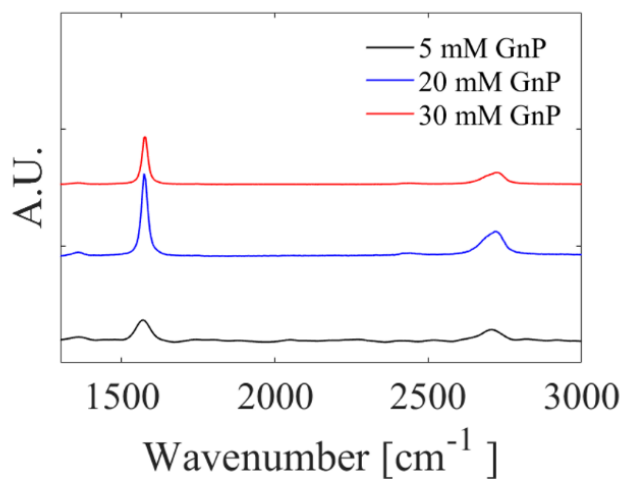


Figure 2.3.10 The Raman spectrum of ZnO at different concentrations of GnP of 5 mM, 20 mM, and 30 mM [58].

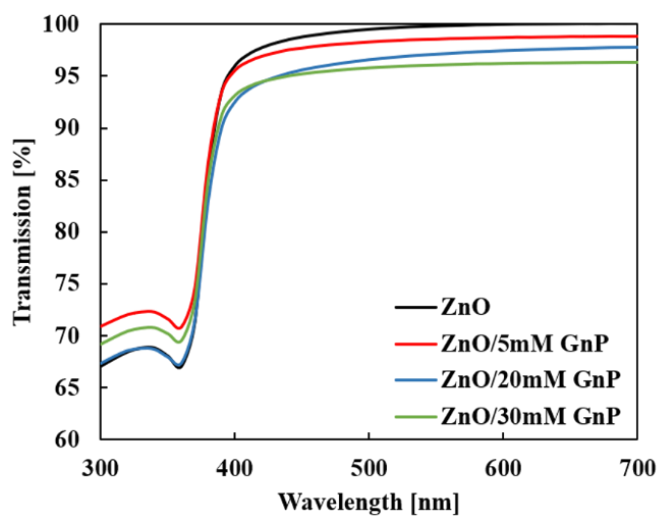


Figure 2.3.11 The transmission as a function of wavelength is shown for ZnO and ZnO/GnP at the different GnP concentrations of 5 mM, 20 mM and 30 mM [58].

2.3.9 Crystallinity of Printed WO₃ Films and Morphology

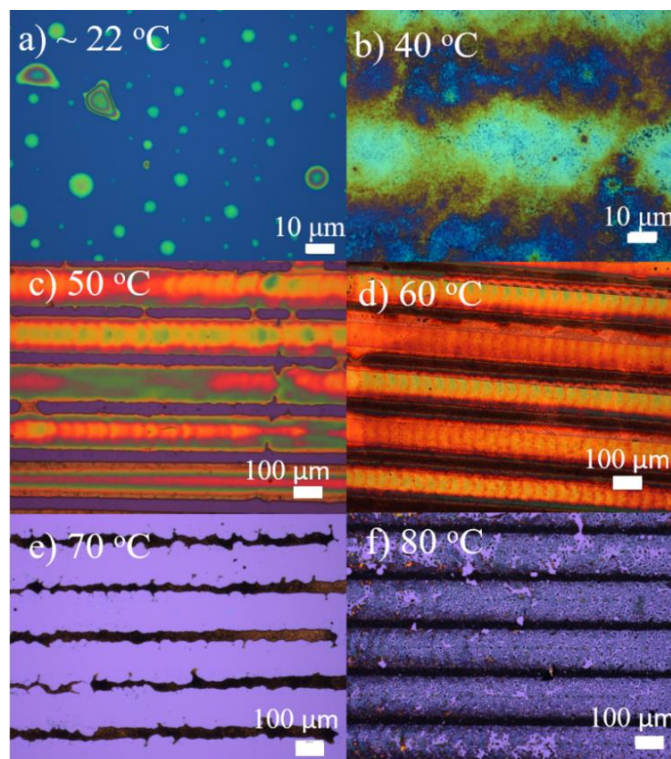


Figure 2.3.12 Printing three scans of the WO₃Pr ink at (a) room-temperature (b) 40 °C (c) 50 °C (d) 60 °C (e) 70 °C and (f) 80 °C. The ink concentration was at a con 0.02 M [59].

Figure 2.3.12 compares the inkjet printed morphology of six printed samples using the same interdigitated printing pattern at a ammonium metatungstate concentration of 0.02 M at substrate temperatures of 22, 40, 50, 60, 70 and 80 °C, for **Figure 2.3.12a-f**, respectively, at a three printed scans. At room-temperature (22 °C) the ink could not spread well on the SiO₂/Si wafer, resulting in isolated droplets (**Figure 2.3.12a**). As the temperature is increased there is a steady increase in film formation, improved ink spreading is clearly seen up to 50 °C (**Figure 2.3.12 b-d**). However, a more prominent coffee ring effect was observed at higher temperatures, which is expected for increased temperatures while printing [29, 76]. In the extreme cases ink evaporation increased preventing ink spread and continuous films from forming (**Figure 2.3.12e**) and at 80 °C the ink began to boil and spray and over time complete drying and clogging of the capillary tip (**Figure**

2.3.12f). However it was found that the optimal substrate temperature window is 40-60 °C, as a result a lot of the printing will be focused on printing a temperature of 50 °C unless it is otherwise indicated.

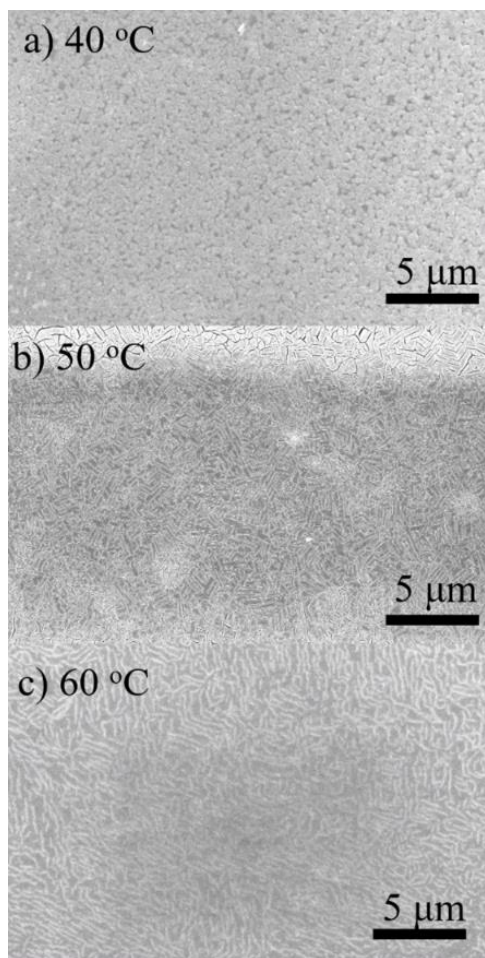


Figure 2.3.13 SEM images of the printed films on substrates heated to (a) 40 °C, (b) 50 °C, and (c) 60 °C, respectively [59].

The SEM images of the three samples printed at 40 °C, 50 °C, and 60 °C printing temperature are depicted in **Figure 2.3.13a-c**, respectively, after undergoing annealing as described in Section 2.2.3 to form crystalline WO₃. At the printing temperature of 40 °C, the printed WO₃ film is rather porous, rough and cracked (**Figure 2.3.13a**), however, at higher printing temperatures of 50-60

°C, the films becomes more uniform with just rough and rigid surface texture and some microscopic cracking at the surface (**Figure 2.3.13b-c**). The rough and rigid film comes about from the small non-uniformity of the surface of the printed film. In addition, the non-uniformity in the film and a presence of the coffee ring affect occurring at higher temperatures there is induced stress and strain at the surface of the film which can result in a cracked film [29, 76].

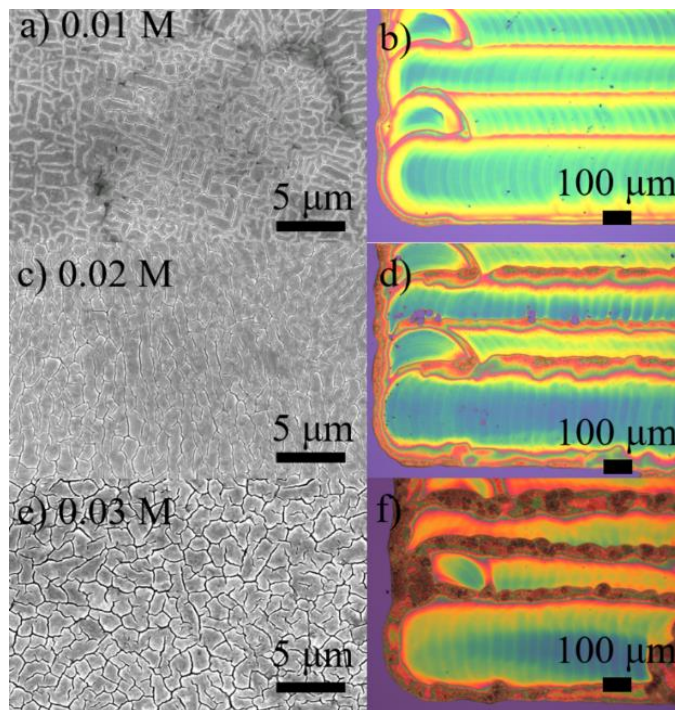


Figure 2.3.14 SEM images of WO_3 films and optical images of their corresponding printed WO_3Pr films of (a) and (b) at 0.01M; (c) and (d) at 0.02M, and (e) and (f) at 0.03M. All samples have three printing scans and the 50 °C substrate temperature [59].

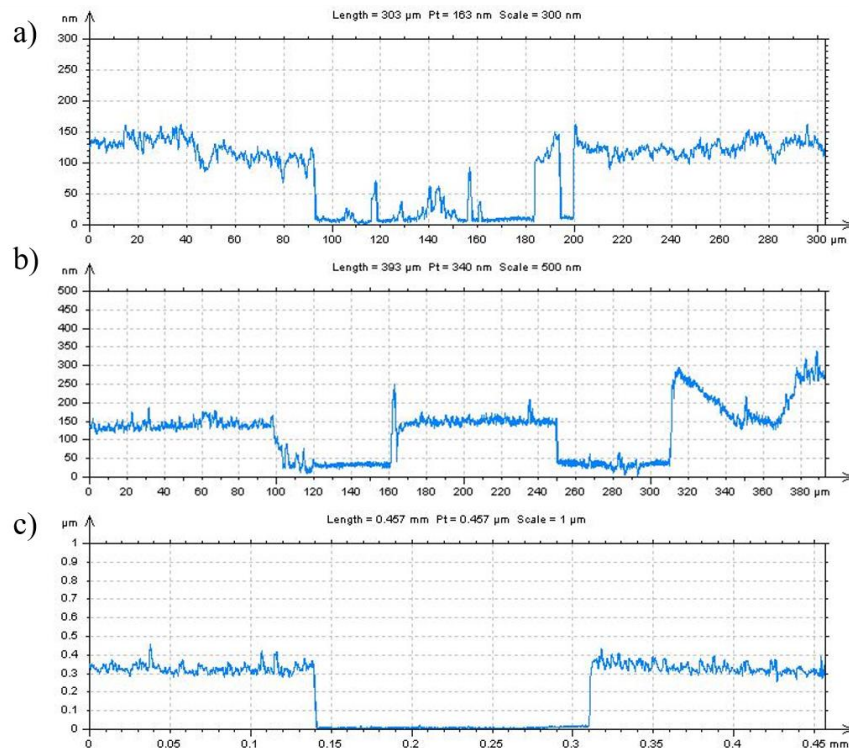


Figure 2.3.15 Three printed scans of different concentrations of WO₃ precursor ink at (a) 0.01 M (b) 0.02 M, (c) 0.03 M with thicknesses, 100-150 nm, 150-200 nm, and 400 nm, respectively, at printing temperature of 50 °C [59].

Changing the ammonium metatungstate molar concentration from 0.01, 0.02, and 0.03 M is then performed to understand the concentration effect on the morphology of the printed WO₃Pr and the WO₃ films after the annealing. The films varied from rough and rigid films (**Figure 2.3.14a-d**) to being cracked (**Figure 2.3.14 e-f**). The thickness profiles of the different concentrations, the 0.01 M and 0.02 M show little difference in thickness after three printing scans, varying in thickness between 100-200 nm, respectively (**Figure 2.3.15 a-b**), however the three scans at 0.03 M shows an increase in thickness to approximately 400 nm (**Figure 2.3.15c**). To further investigate the thickness effect on the film morphology 0.02 M was chosen and printed at 3, 5, and 7 printing scans. The resulting films have film thickness of 150, 350, 500 nm for 3, 5, and 7 printing scans, respectively.

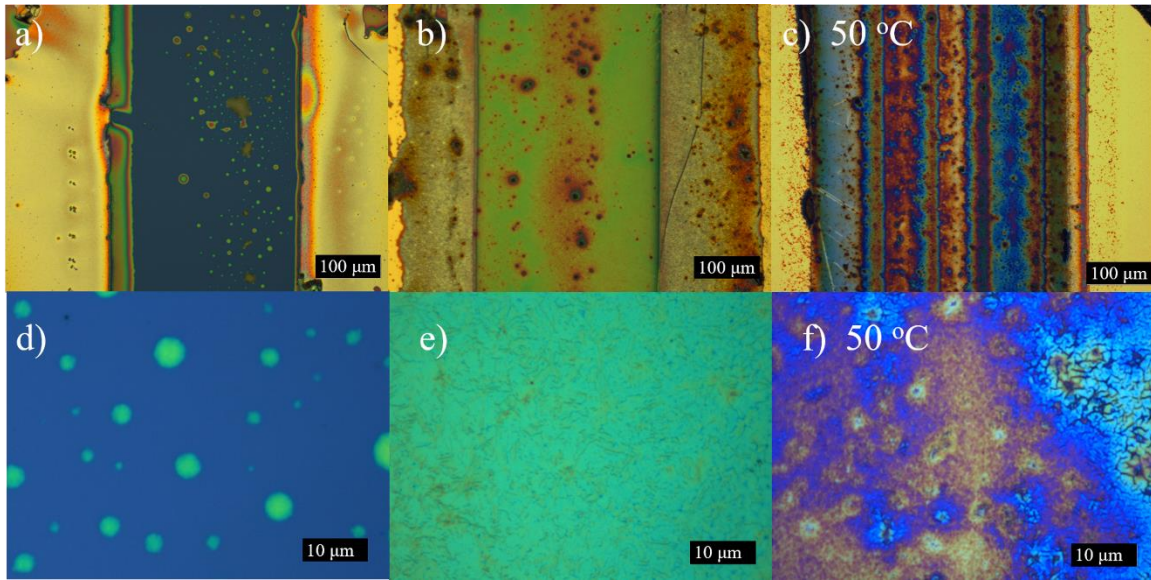


Figure 2.3.16 Optical images of the WO_3 samples printed between Au electrodes of $\sim 300 \mu\text{m}$ spacing on: (a) regular SiO_2/Si wafer at room temperature; (b) and (c) on ZnO QDs textured SiO_2/Si substrates at room temperature and 50°C , respectively; (d)-(f) are the zoom-in optical images of the same samples in (a)-(c), respectively. All samples were printed using the same printing parameters and subjected to annealing at 500°C for 2 hours in air to form crystalline WO_3 [42].

On the other hand, the WO_3 precursor was also printed on a ZnO QDs textured surface which is shown in the following optical image (**Figure 2.3.16**). The optical image of a representative WO_3 sample printed on regular SiO_2 substrates is shown in **Figure 2.3.16a**, which consists of droplets instead of a continuous film, and the magnified view of the same sample is shown in **Figure 2.3.16d**, in which the size of the droplets is shown to be in the range of few to tens of micrometers. Introducing a ZnO QD texturing layer produces a continuous WO_3 film if the WO_3Pr printing was performed at room-temperature (**Figure 2.3.16b**). Nevertheless, the coffee-ring effect (shown as lines along the printing direction) is clearly visible in an otherwise similar sample except the WO_3Pr printing was performed at 50°C (**Figure 2.3.16c**) [59]. In contrast to no coffee-ring

effect on the room-temperature printed WO_3 sample on SiO_2/Si with a ZnO QD texturing layer (**Figure 2.3.16b**). This observation reveals the correlation between the accelerated ink evaporation on the surface of the substrates and the formation of the coffee-rings, which results from precursor or liquid drying earlier on the outer edges of the droplet than on the center of the droplet [29, 76]. This results in an uneven sample morphology, and in many cases cracking formation due to uneven mechanical stress during post heating treatments. The much improved surface morphology, especially the absence of the coffee-ring effect in **Figure 2.3.16b** and its zoom-in view in **Figure 2.3.16e**, illustrates a ZnO QD texturing layer is effective in preventing ink aggregation towards the ink drop edge. This benefit, however, may diminish at elevated printing temperature of 50°C as shown in **Figure 2.3.16c** and its zoom-in view in **Figure 2.3.16f**.

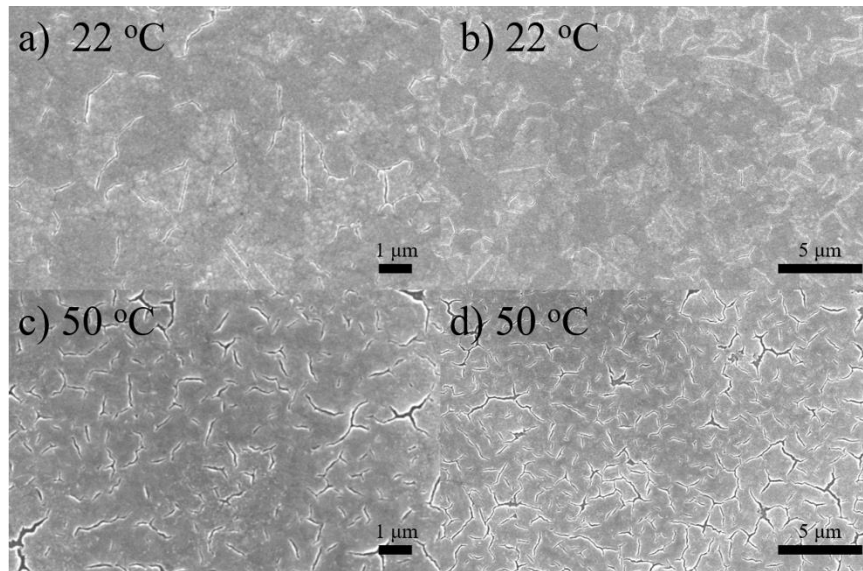


Figure 2.3.17 (a) and (b) are the SEM images after the 500°C annealing of printed WO_3Pr films on ZnO QDs texturing layer at room-temperature; whereas (c) and (d) include the SEM images of WO_3 samples through a similar process except the WO_3Pr printing was carried out at 50°C . The scale bars are $1\ \mu\text{m}$ in (a) and (c) and $5\ \mu\text{m}$ (b) and (d) [42].

Figure 2.3.17 shows the SEM images of the WO_3 films printed from the WO_3Pr ink on the ZnO QDs texturing layer on SiO_2/Si substrates at room-temperature (**Figure 2.3.17 a-b**) and at 50 °C (**Figure 2.3.17c-d**). The former shows a more uniform film morphology than the latter. In fact, the heated printing shows many cracks likely caused by high local stress induced in the uneven films due to uneven reaction of the precursor to form crystalline phases during annealing at 500 °C.

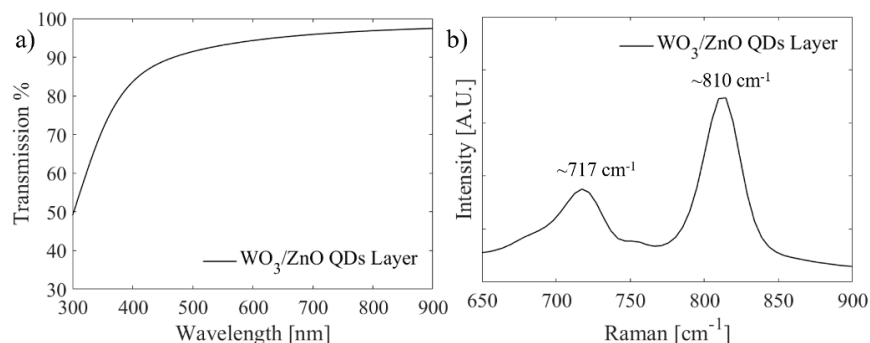


Figure 2.3.18 The optical transmission and the Raman spectrum for the WO_3/ZnO QDs layer film are depicted in (a) and (b), respectively [42].

The optical transmission was obtained for the WO_3/ZnO QDs layer film (**Figure 2.3.18a**) with a band edge beginning at around 480 nm which is consistent with the bandgap of approximately 3.2 eV. To further confirm the quality of WO_3 , a Raman spectrum was obtained and two prominent peaks at approximately 717 cm^{-1} and 810 cm^{-1} which is consistent with previous reports of the Raman spectra for monoclinic WO_3 (**Figure 2.3.18b**) [77].

2.3.10 Graphene and Quantum Dot Nanohybrids Crystal Structures

The absorption spectra of the three kinds of photosensitizers are shown in **Figure 2.3.19a** along with their TEM images for ZnO QDs, PbS QDs, and FeS_2 NCs in **Figure 2.3.19b-d**, respectively. The ZnO QDs (black) show an absorption edge at approximately 360 nm as expected from around

the energy bandgap of 3.37 eV (**Figure 2.3.19a**). For the PbS QDs (blue), the absorption edge is at around 940 nm indicating a bandgap of ~ 1.3 eV which is in agreement with PbS QDs of size 4 nm (**Figure 2.3.19a**) [78]. Lastly, the FeS₂ NCs (red) has a broadband absorption with a broad peak located around 900 nm due to shape-induced localized surface plasmonic resonance as shown in our previous work (**Figure 2.3.19a**) [52]. From the TEM images, it is clearly seen that the ZnO and PbS QDs have spherical or irregular shapes while the FeS₂ NCs have a cubic shape. In addition, the average dimensions are approximately 5.6 ± 4.0 nm, 4.3 ± 4.4 nm, and 99.4 ± 19.8 nm for the ZnO QDs, PbS QDs, and FeS₂ NCs, respectively. The insets of **Figure 2.3.19b-d**, are the HRTEM of the corresponding QDs or NCs, illustrating high crystallinity for the three types of samples. Based on the HRTEM images, the lattice spacings of 0.26 nm, 0.29 nm, and 0.27 nm are observed as expected for ZnO, PbS, and FeS₂, respectively.

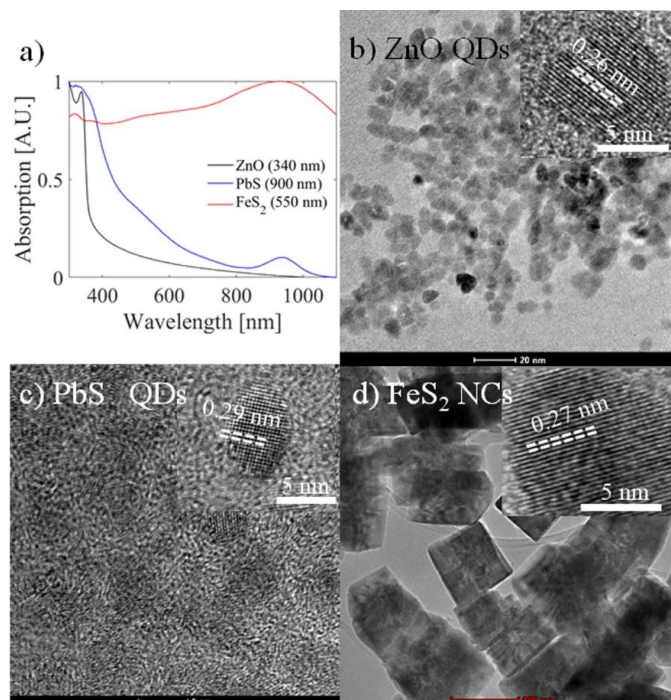


Figure 2.3.19 (a) Optical absorption spectra of ZnO QDs (black), PbS QDs (blue), and FeS₂ NCs (red). TEM images of the (b) ZnO QDs, (c) PbS QDs, and (d) FeS₂ NCs, respectively, with their HRTEM images as the insets [53].

Chapter 3

Inkjet Printed and Hydrothermally Grown ZnO/Graphene Nanohybrids

In this chapter, we will discuss results obtained from inkjet printed ZnO films with and without graphene for UV photodetection, and hydrothermally grown ZnO nanowires on graphene for both UV photodetection and stress and strain sensing, respectively.

3.1 *Printed Zinc Oxide Nanostructures with and without Graphene for UV Photodetectors*

The current-voltage characteristics of the printed ZnO precursor ink (ZnOPr) and the ZnO precursor ink mixed with ZnO QDs (ZnOPrQDs) samples were measured in dark and under a monochromatic light source with a wavelength of 340 nm at UV power of $P=10.45 \mu\text{W}$, and UV intensity $I=0.52 \text{ mW/cm}^2$. The results are compared in **Figure 3.1.1** of the ZnOPr and ZnOPrQDs detectors, which have similar dark currents while the latter has significantly higher illuminated current (**Figure 3.1.1a**). This may be attributed to the nanoporous morphology of the ZnOPrQDs sample with higher surface-to-volume ratio and therefore higher electron-depletion effect, as compared to the microporous morphology in the ZnOPrQD sample. In addition, an on/off ratio of 2470 and 949 was found for the ZnOPrQDs and the ZnOPr, respectively, with a photoresponsivity of at 5.0 V of 383.6 A/W and 14.7 A/W. The improved performance by more than an order of magnitude in the ZnOPrQDs sample compared to the ZnOPr sample illustrates the importance of controlling the morphology and microstructure of the printed ZnO nanostructure UV detectors. The nanoporous structure obtained using ZnO QD-assisted printing from the ZnOPrQDs ink indicates the nanocomposite inks by inclusion of ZnO QDs may provide a versatile approach towards such a control. **Figure 3.1.1b** exhibits the responsivity as a function of voltage measured

on both ZnOPrQDs and ZnOPr samples showing a linear growth in photoresponsivity at increasing voltage.

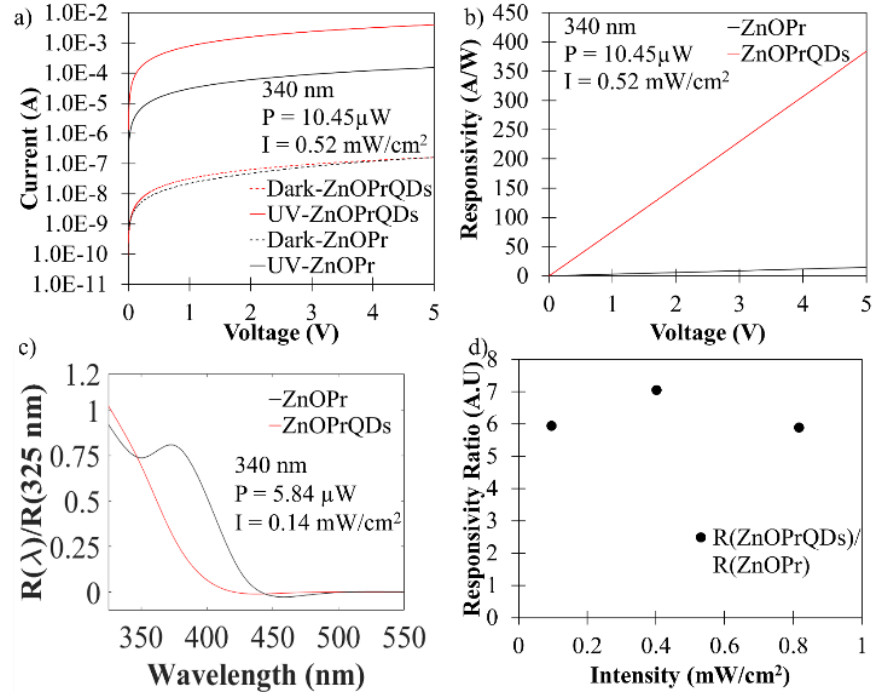


Figure 3.1.1 (a) The dark current and illuminated (UV light intensity of 0.52 mW/cm²) current as function of the bias voltage of ZnO films printed using ZnOPr (red) and ZnOPrQDs (black) inks; (b) Spectral UV responsivity under a UV power of 5.84 μW as a function of voltage; (c) The photoresponsivity divided by the maximum responsivity and (d) the ratio of the photoresponsivity of ZnOPrQDs with respect to ZnOPr [57].

The ratio of photoresponsivity at 325 nm with respect to the responsivity at other wavelengths shows a band edge around 375 nm that is clearly visible across where the photoresponsivity increases (**Figure 3.1.1c**). In addition, the normalized photoresponsivity of ZnOPr depicts a photoresponsivity that is larger than ZnOPrQDs film at 375 nm, which indicates that the band edge for ZnOPr is broaden allowing lower photon energies to excite electrons into the conduction band.

The band edge broadening is likely caused by poorer crystallinity in ZnOPr film, whereas ZnOPrQDs shows a band edge closer to highly crystalline ZnO likely contributing to better performance. The observed trend in spectral responsivity is consistent with high crystallinity of the printed ZnO nanostructure samples revealed from the TEM measurement in Section 2.3.8 in **Figure 2.3.6**. The responsivity ratio of ZnOPrQDs to ZnOPr as a function of UV intensity at the 1.0 V bias is shown in **Figure 3.1.1d**, the responsivity ratio shows ZnOPrQDs is approximately 6 times the responsivity of ZnOPr at lower intensities. The responsivity ratio shows little change from higher and lower intensities of UV light, indicating the charges generated is proportional to the available photons, which means ZnOPrQDs film generates more charge per photon at all intensity than the ZnOPr film.

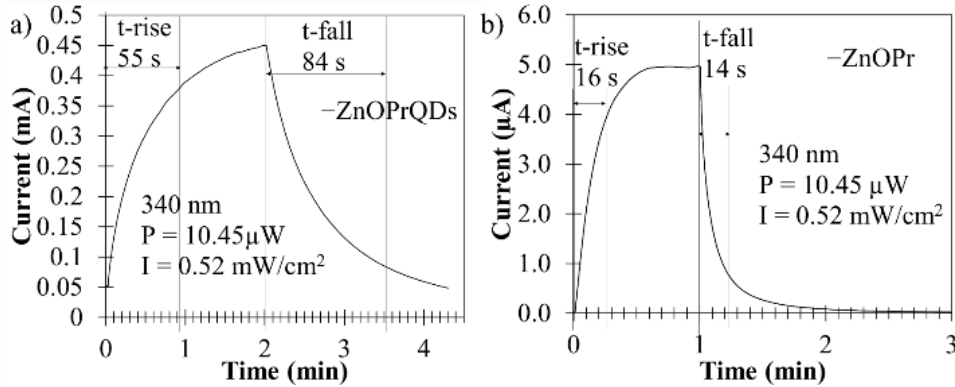


Figure 3.1.2 (a) The ZnOPr has a rise and fall time 16 s and 14 s, and (b) the ZnOPrQDs shows a rise and fall time of 55 s and 84 s, respectively, both films were tested at a 5 V bias [57].

In **Figure 3.1.2**, the dynamic response is compared of the ZnOPr and ZnOPrQDs inks showing former has a rise/fall times of 16 s/14 s, while the latter, 55 s/84 s. The photoresponse is much slower than that of highly crystalline bulk ZnO because of the large time frame needed for oxygen desorption (upon UV illumination) and absorption (UV off) on the ZnO nanostructure surface.

This means the significantly enhanced photoresponsivity due to the surface electron depletion effect in the nanostructured ZnO UV detectors is at a cost of the reduced response speed. This also explains the moderately increased response times in the ZnOPrQDs sample due to the increased surface-to-volume ratio in these nanoporous ZnO films printed with the assistance of the ZnO QDs. Similar results were found with a spin-coated precursor that used an ultrafast thermal annealing method that allowed for nanoparticles to bead and conjoin into an interlinked nanoparticle film, which achieved a photoresponsivity of 430 A/W at a UV light wavelength and intensity of 340 nm and 0.003 mW/cm² [62]. In contrast, the ZnO nanoparticle films can be further enhanced by incorporating graphene. In **Figure 3.1.3** is the dynamic performance of a ZnO/graphene photoconductor, as can easily be seen the ZnO film is improved an order of magnitude compared to the nanoporous and conjoined nanoparticle films. The photoresponsivity as a function of wavelength shows that the ZnO/graphene nanohybrid films still has the same spectral properties as ZnO, while graphene merely acts as the conducting material that ZnO gives charge and electrostatic gating too through electron charge transfer from the ZnO layer to graphene (**Figure 3.1.3a**). The dynamic response of the film (**Figure 3.1.3b**) shows a repeatable dynamic curve under on/off cycles of UV illumination at 340 nm and gives a rise/fall time of approximately 25 s/23 s, respectively. In addition, the incident light power dependence of the device in terms of dynamic temporal response and the photocurrent and photoresponsivity are depicted in **Figure 3.1.3c-d**, respectively. As can be seen in **Figure 3.1.3d**, the photocurrent linearly increases with light intensity while the photoresponsivity inversely decreases with respect to the light intensity indicated a reduction of quantum efficiency from charge saturation of the device channel at higher intensities of light.

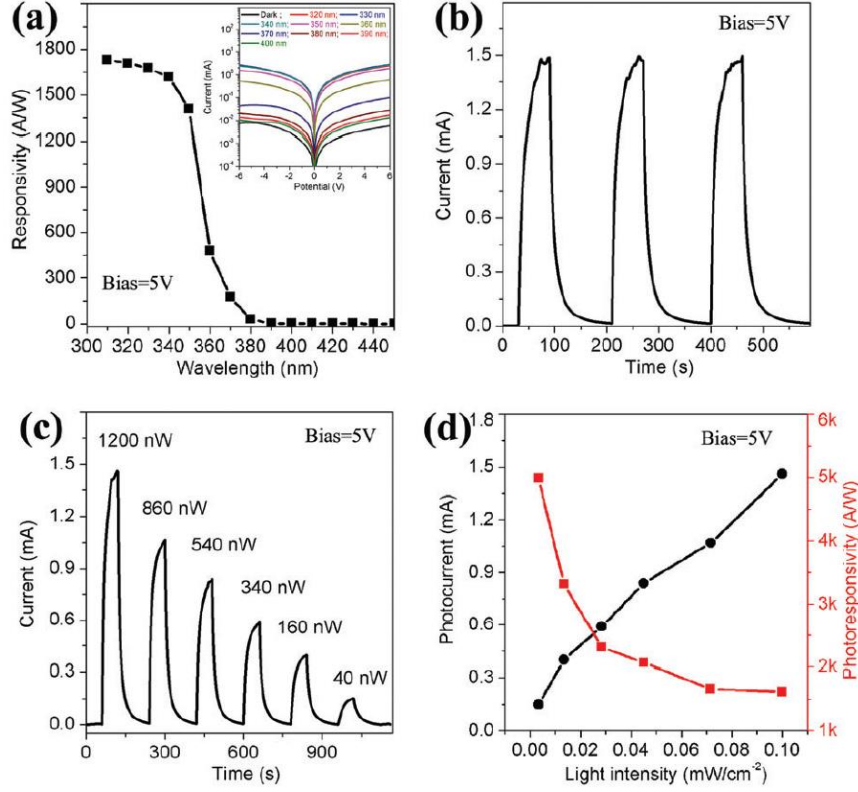


Figure 3.1.3 In (a) is the spectral curve for the ZnO/graphene nanohybrid film and (b) the dynamic temporal response, while in (c) is the dynamic response as a function of light intensity and (d) the photocurrent and photoresponsivity as a function of light intensity [55].

3.2 Zinc Oxide Nanowires/Graphene Nanohybrid UV Photodetectors

The photovoltaic performance of the ZnO NW array hydrothermally grown on graphene utilizing the seeded and seedless method is depicted in **Figure 3.2.1**. In **Figure 3.2.1a** compares the current-voltage (I-V) characteristic curves in dark and under UV illumination at the power $P \sim 8.98 \pm 1.56 \mu\text{W}$ on the ZnO NW/graphene nanohybrids devices made from the seedless (black) and seeded (red) processes, respectively. The dark current, I_{dark} (dashed), of the ZnO NW/graphene sample obtained using seedless process is significantly lower than its counterpart grown using the seeded process by more than an order of magnitude. This is because the defective ZnO seed layer

may introduce direct charge doping into graphene increases the conductivity of the graphene. At 5 V bias voltage, the seedless has a photocurrent of 37 μA while the seeded grown nanowires is 176 times higher. Considering the UV illumination power is the same on the two samples of the same device configuration and dimension, the higher photocurrent values in the latter case implies higher photoresponsivity. Indeed, at 5V the photoresponsivity is around 728 A/W for the ZnO NW/graphene nanohybrid grown with a seed while the seedless method is 4.12 A/W, in addition, a photoconductive gain of 2655 can be estimated for the ZnO NW/graphene nanohybrids devices made using the seeded method, which is ~ 177 times of that for the similar devices made using seedless method. In addition, the spectral of the ZnO NWs grown with a seed are shown in **Figure 3.2.1b**. Indeed from the spectral there is some response throughout indicating many defects likely from the seed layer which becomes more apparent with the dynamic response. The dynamic curves for the seedless and seeded growth methods are shown in **Figure 3.2.1c** and **Figure 3.2.1d**, respectively. From the seedless sample you can clearly see an increase in current under UV illumination giving a rise time of approximately 269 s, which was found by calculating the time it takes to go from 0% of the photocurrent to 80% of the photocurrent, the decay time would be calculated from the max of the current to 80% of the current back down, however it was omitted as it would take hours. This slow decay is likely caused from the slow time it takes for oxygen to return to the entire surface of the ZnO NW array. The slow decay is even more severe in **Figure 3.2.1d**, which in this case it likely not only the oxygen effect but the more defective seed layer acting as charge traps, however, this device showed a fast rise time in this case it being negatively responsive to complete saturation. In this case, the seeded showed a rise time of 139 s which is nearly twice as fast, which can be contributed to the highly dense ZnO NW array easily saturating the sample with charges and quickly doping graphene. However, the seed layer which plays a

critical role hinders charges from returning to the nanowire array and therefore there is hardly any return change in current when the UV light is turned off.

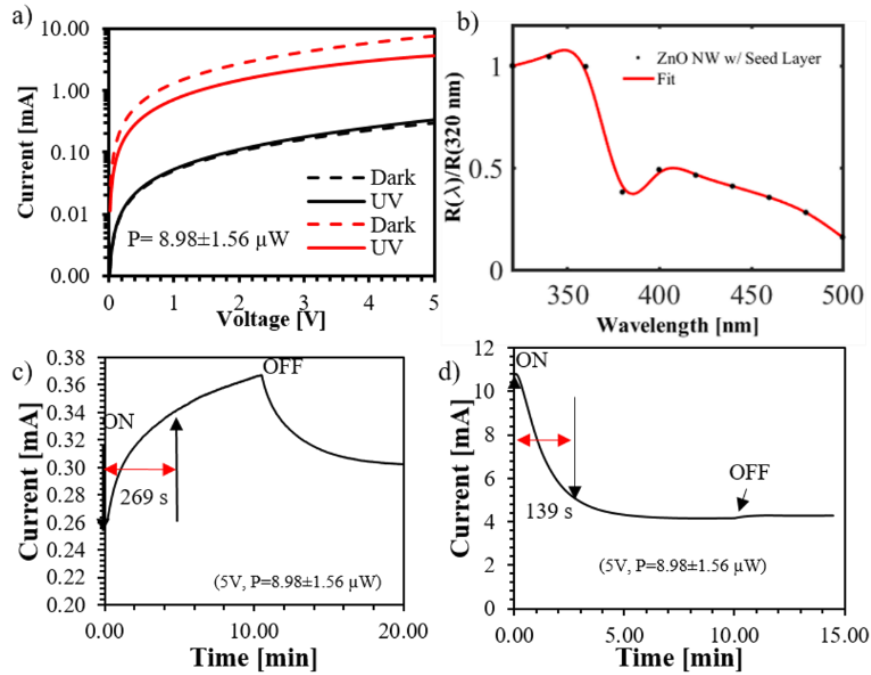


Figure 3.2.1 The I-V characteristics curves in dark and under illumination of UV of 340 nm wavelength and $8.98 \pm 1.56 \mu\text{W}$ power for ZnO NW/graphene nanohybrids obtained from (a) seedless (black) and seeded (red) hydrothermal growth, respectively. The spectral of seeded sample is shown in (b) and the dynamic response of the two samples are shown in (c) seedless and (d) seeded [60].

The negative photoresponse seen in the ZnO NW arrays grown on graphene via a seed layer is because of doping and the fact that the conductivity measured is of graphene. These opposite directions regard to the increase or decrease of the graphene conductivity from the dark value by the UV illumination. ZnO is intrinsically n-type and will provide a positive charge (hole) doping on graphene, which leads to a shift of the Fermi energy (E_F) downwards from the Dirac point (**Figure 3.2.2a**). When a defective ZnO seed layer is placed on graphene (**Figure 3.2.2b**), much

more significant hole-doping may occur. When ZnO is illuminated with UV light the electrons are transferred to graphene and holes become trapped at the ZnO/graphene interface. The holes provide n-doping to graphene and push the Fermi level back towards the Dirac point as shown in the source-drain current (I_{ds}) vs gate voltage (V_g) characteristics at the bottom of **Figure 3.2.2**. In the seedless grown ZnO NWs/graphene sample, the minor deviation of the Fermi energy below the Dirac point in dark can be shifted upwards to the electron branch of the I_{ds} - V_g , which results in a positive change in conductivity (higher conductivity) upon UV illumination. In contrast, for the seeded grown ZnO NWs/graphene sample there is large p-doping, and the same UV illumination may not be adequate to shift the Fermi energy from the hole branch to the electron branch of the I_{ds} - V_g curve. This leads to negative change in conductivity of graphene as depicted in **Figure 3.2.2a** and **Figure 3.2.2b**, respectively.

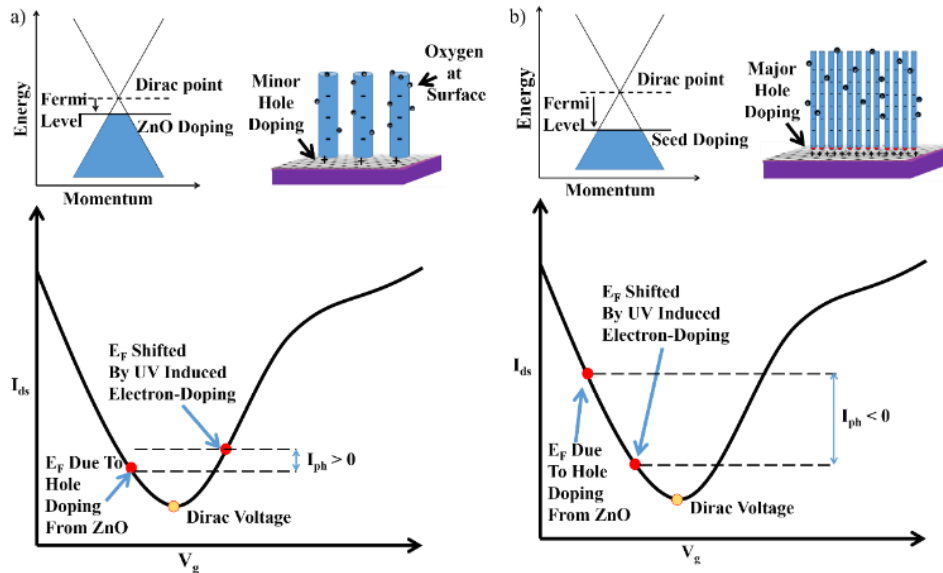


Figure 3.2.2 Schematic description of the photo-induced charge doping in graphene as a consequence of photo-induced charge transfer from the ZnO NWs to graphene in the ZnO NWs/graphene nanohybrids grown in (a) the seedless process and (b) the seeded one [60].

3.3 *ZnO Nanowire/Graphene Strain and Stress Sensor*

ZnO nanowire/graphene nanohybrids can also function as a stress and strain sensor since ZnO can also function as a piezoelectric meaning that through the deformation of the ZnO crystal lattice an electric field is produced from the asymmetric charge distribution induced from positive and negative ions of the lattice. The ZnO NW/graphene nanohybrids in the device are grown using the same method as in the Section 3.1, however these devices are passivated with PMMA to increase the robustness and durability of the ZnO NWs and graphene. In **Figure 3.3.1a** depicts the side by side image of the vacuum pressure device for applying N₂ gas pressure on device (left) and the spring apparatus for applying vertical compressive force via a spring with spring constant of 1.23 N/mm (right) on a ZnO nanowire/graphene sample. The vacuum setup is useful for measure small pressures down to mTorr while the spring setup is particularly beneficial for measuring the dynamic response. When these apparatuses apply pressure the ZnO produces an electric field which then causes a shift in the fermi energy of graphene by drawing charges to the interface between graphene and ZnO and as a result the Dirac voltage of graphene then shifts as can be seen in the schematic diagram of the source-drain current versus back-gate voltage (**Figure 3.3.1b**) [79-81]. A positive and negative charge doping of graphene will result in a decrease or increase in Fermi energy, respectively, as a result a positive shift in Dirac voltage will result from negative charge in graphene while a negative Dirac voltage will be caused by the presence of positive charge as discussed previously for **Figure 3.2.2**.

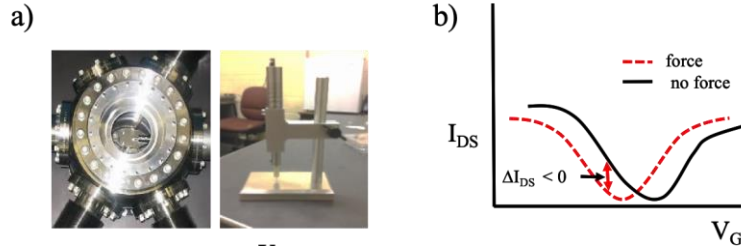


Figure 3.3.1 Schematic of pressure chamber and mechanical spring apparatus for pressure and compressive force on device are shown in (a). In (b) is a diagram of how the Dirac voltage is shifted under stress/strain of nanowires.

The semi-log plot of the change in conductance over initial conductance ($\Delta \sigma / \sigma_0$) versus pressure are compared for ZnO nanowire/graphene (red) and ZnO film/graphene (black) devices are shown in **Figure 3.3.2a**. Both devices have a similar sharp linear increase then a flatter linear increase as a function of pressure indicating there are two regimes of sensitivity for the devices. The sensitivity was calculated by taking the slope of semi-log plot where, $\Delta \sigma = \sigma - \sigma_0$ and σ_0 is the initial conductance without applied pressure. Both devices are showing very sensitive even to changes in micro-Torr of air pressure having a sensitivity of $1.07 \times 10^{-2} \text{ kPa}^{-1}$ from pressure range of 1.1 mTorr to 420 Torr for ZnO NWs/graphene devices and a value of $2.0 \times 10^{-3} \text{ kPa}^{-1}$ for ZnO film/graphene devices which was approximately five times less. This is attributed to ZnO NWs having large elasticity deformation parallel and perpendicular to the graphene/substrate surface, while ZnO films deal with internal stress and strain of the entire bulk film perpendicular and parallel to the graphene/substrate surface. Furthermore, compared with similar work done in literature the ZnO NW/graphene device has three times enhancement in sensitivity and ~ 8 times faster response time [79-81]. The higher performance of our device was attributed to the seedless hydrothermal growth of ZnO NWs directly on graphene allowing for efficient charge exchange and transfer, which is critical for the performance of the ZnO NWs/graphene nanohybrid devices

[60]. The I-V curves are taken at 0 N, 0.14 N, 0.28 N, and 0.58 N using the spring apparatus from which the slope of each line gives the conductance, this is used to calculate $\Delta \sigma/\sigma_0$ and is plotted with respect to the forces applied and is inset of **Figure 3.3.2b** along with the I-V curves. The inset has a change in signal to noise ratio of to $2.72 \times 10^{-3} \text{ kPa}^{-1}$. The dynamic response to pressure the sensor was measured at a spring for of 0.37 N, 0.43 N and 0.5 N forces under a constant voltage bias of 1 V as shown in **Figure 3.3.2c**. At higher applied force there is a larger change in current as can be seen in dynamic change, which is attributed to the greater displacement of ions in the lattice creating a larger gating of graphene and thus a larger shift in fermi energy and change in conductivity of graphene. The rise/fall time is also measured, and is defined as the time taken by a sensor to go from 10% to 90% of the total signal change and the time to fall from 90% to 10% of the total current change is the fall time, the measured rise and fall time of this sensor is approximately 0.1 s for both rise and fall time, which is better than the similar piezoelectric sensor using CVD graphene and hydrothermally grown ZnO NWs with a response time of $\sim 0.8/0.85 \text{ s}$ [80]. Better response time for our device was obtained from the clean ZnO NWs/graphene interface, which results from the direct growth of ZnO on graphene.

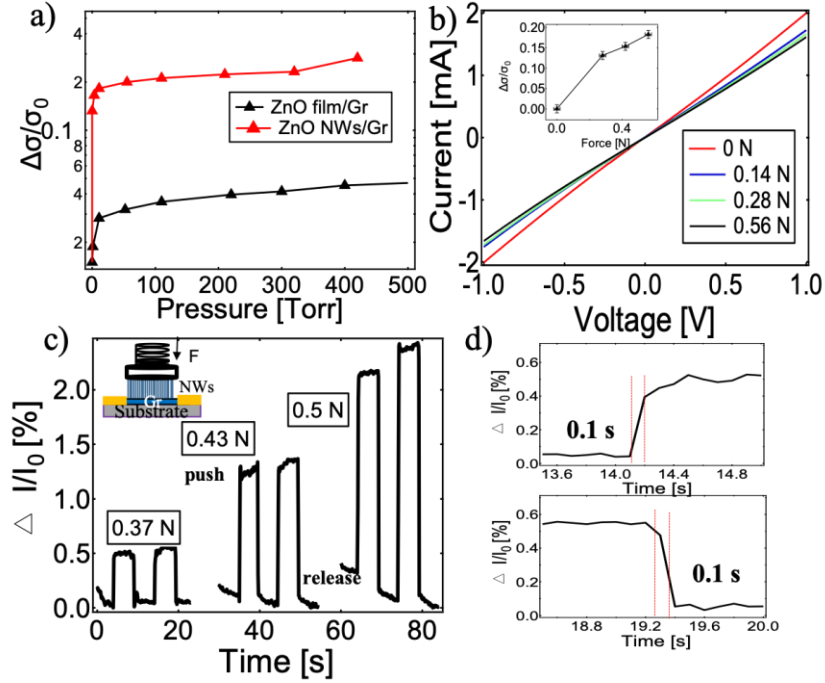


Figure 3.3.2 In (a) is the change in conductance with respect to the initial conductance ($\Delta\sigma/\sigma_0$) as a function of air pressure for ZnO NWs/Gr and ZnO film/graphene devices. In (b) is the I-V characteristic curves for different magnitude of mechanical strain with an inset showing the sensitivity of the device for the given range of forces. In (c) is the dynamic response as a function of force with the inset showing schematic of spring apparatus and finally in (d) is a zoom in image for the rise and fall time.

This device can also be fabricated using a polymer substrate instead of SiO_2/Si wafer, namely polyethylene terephthalate (PET), here the PET is incorporated so the device has more elasticity and flexibility compared to the SiO_2/Si wafers. In **Figure 3.3.3a**, illustrates the experimental design used to characterize the sample, as shown, the force was applied on top of the PMMA/ZnO NWs/graphene channel with the spring-based mechanical system. A schematic of how an electric potential induced under strain of the nanowires, which in turn changes the conductivity of graphene is shown in **Figure 3.3.3b** and is the same mechanism as described for the hard substrate device.

In **Figure 3.3.3c**, compares the dynamic response of the device by applying a force of 0.3 N (blue) and 0.5 N (black) and under compressive force a DC signal is generated under a 1 V bias with the amplitude of about 4 μA at a force of 0.3 N and 6 μA at 0.5 N. It is observed that higher signal amplitude change is observed by applying a 0.5 N of force which is consistent results obtained with the hard substrate from these results it can be determined that the sensitivity of sensor is $6 \times 10^{-6} \text{ kPa}^{-1}$. In **Figure 3.3.3d** the dynamic at 0.56 N and the inset shows the zoom in of the rise and fall edges of the dynamic, which is used to calculate the rise and fall time of the sensor, where the rise/fall time is the time taken to achieve 90% of the total signal change from initial to final and vice versa. The obtained rise and fall time is rather symmetric with a value of 0.2 s for both rise and fall time. The fast response time can be attributed to a clean interface between the ZnO NWs and graphene such that the graphene can feel the effects of the total electric potential generated. In addition, all the dynamic curves observed at a 1 V bias give a negative signal response indicating the fermi level is shifted closer to the Dirac point.

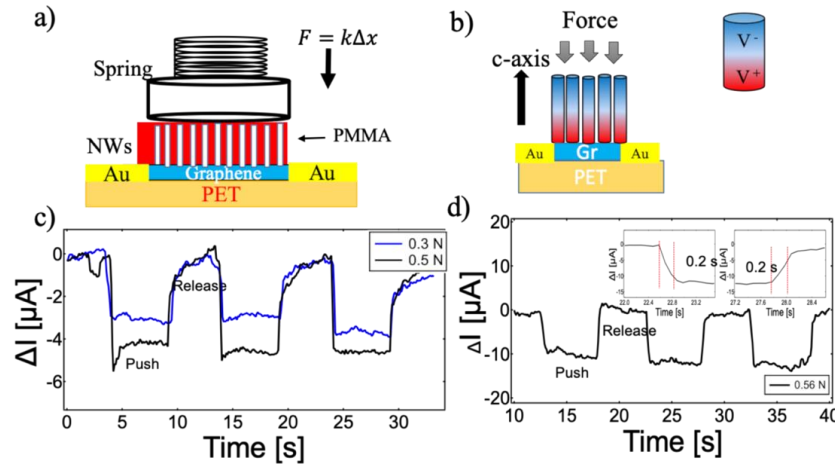


Figure 3.3.3 (a) Schematic of spring setup for applying mechanical pressure on device, (b) schematic of how piezo-potential induced under deformation, and (c) the dynamic response under different vertical compressive forces. (d) Dynamic response and inset showing zoom in image for the measurement of rise/fall time depiction.

Figure 3.3.4a depicts the schematic illustration of the homemade bending apparatus for the bending test, where approximately $1\text{ cm} \times 2\text{ cm}$ sample device is mounted on the cylinder, where one end of the sample is attached to the cylinder surface and other end is set free for the bending up and down. A schematic diagram of the source-drain current (I_{DS}) verse back-gate voltage (V_G) to show the shift in current when the bending is applied to our sample is shown in **Figure 3.3.4b**, where the dotted red and blue curve indicates the I_{DS} for down and up bending, respectively, and the equilibrium position is denoted by solid black curve. The symmetry of the characteristic I_{DS} vs. V_G curve for graphene red dotted curve results in negative change in current, while the blue curve results in a positive change in current. In **Figure 3.3.4c** down/up bending is shown in the black/blue curve, which is taken at a bending radius of 27 mm, with the signal amplitude for both cases of bending being approximately about $60\text{ }\mu\text{A}$. In **Figure 3.3.4d** is the comparison of two dynamic response taken at 55 mm (black) and 27 mm (blue) with a signal amplitude of $10\text{ }\mu\text{A}$ and $60\text{ }\mu\text{A}$, respectively, and the inset of **Figure 3.3.4d** are the zoomed in images of the one of the bend/release cycles depicting the rise/fall times as $0.2\text{ s}/0.15\text{ s}$. In **Figure 3.3.4e**, is the plot of the $\Delta I/I_0$ at different downward bending strain and gives a gauge factor of approximately 67 [82]. This is almost 10 times better than similar PET/CNT/ZnO device and comparable to the graphene-based devices which utilizes the current changes as a result of the bending [82-84]. The gauge factor (G.F.) is calculated by following formula, $G.F. = (\Delta I/I_0)/\epsilon$, where ΔI is the change in current, ϵ is the strain calculated with, $\epsilon = h/2R$, where h is the thickness of the substrate ($200\text{ }\mu\text{m}$ for PET), and R is the radius of curvature at different bending curvatures. The inset in the **Figure 3.3.4e**, is the $(\Delta I/I_0)$ vs bending radius, which gives a sensitivity of $5.2 \times 10^{-2}\text{ cm}^{-1}$ that is determined by the slope. The 20 % current change is observed for the 0-0.37 % strain range. To check the stability and reproducibility of our device, we have taken the dynamic response at a frequency $\sim 0.5\text{ Hz}$ for

large number of cycles depicted in **Figure 3.3.4f**. It is seen that for a large number of bending cycles the device shows relatively good reproducibility and stability with some minor fluctuations.

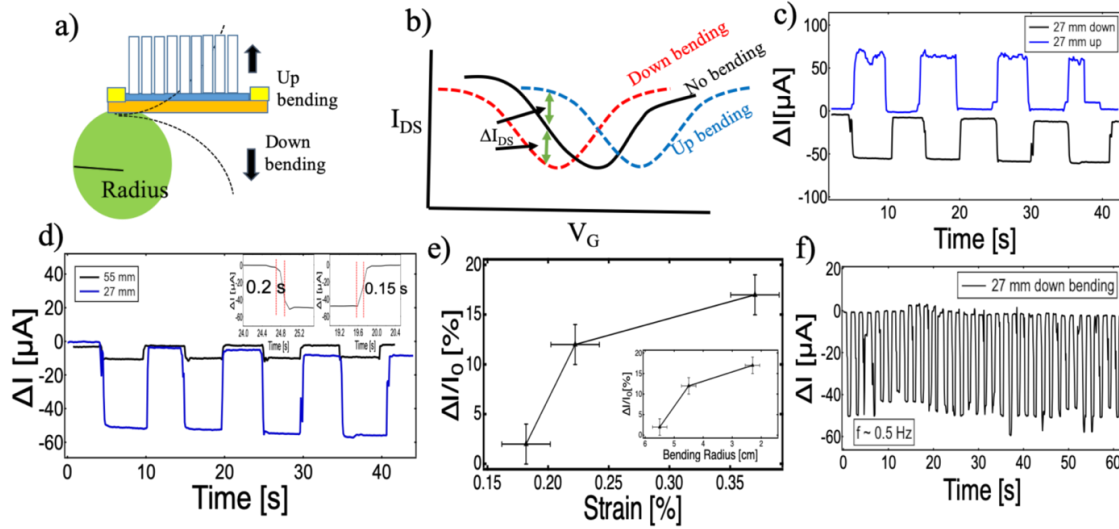


Figure 3.3.4 In (a) is the schematic of homemade bending setup and in (b) is the Dirac point shift as a consequence of bending. In (c) and (d) is the dynamic response comparison of change in current for 27 mm for up-down bending and for bending radii of 55 mm and 27 mm, respectively, with the inset showing a zoom in images for depiction of rise/fall time. In (e) is the change in current as a function of strain induced with the inset showing plot of change in current as a function of bending radius, while in (f) is the dynamic response for the high frequency down bending for large number of cycles.

The hydrothermal growth of NWs without using seed layer on graphene has a crucial effect on the performance of the device so that there is effective interface for charge exchange. In this case, the whole piezoelectric polarization from the NWs is utilized directly to change the conductivity of graphene allowing for detection of small strain of 0.18% which produce significant change in current in graphene of $\sim 10 \mu A$. The G.F. calculated for our device is almost 10 times better than the similar device with ZnO NWs/CNT/rGO with the better response time compared with similar device [82].

Figure 3.3.5 describes the schematic diagram for the working mechanism of the strain sensor at different bending situations for no bending (**Figure 3.3.5a**), down bending (**Figure 3.3.5b**) and up bending (**Figure 3.3.5c**). Under no bending there is no shift in Dirac voltage which is assumed to be positive due to graphene being typically p-doped [85]. Under downward bending it is assumed that a positive potential is produced which then shifts the fermi level up toward the Dirac point inducing a negative change in current (**Figure 3.3.5b**). In the other case, bending upward we instead see a positive change in current, which is likely caused by a negative potential which would shift the fermi level down and away from the Dirac point resulting in higher conductivity.

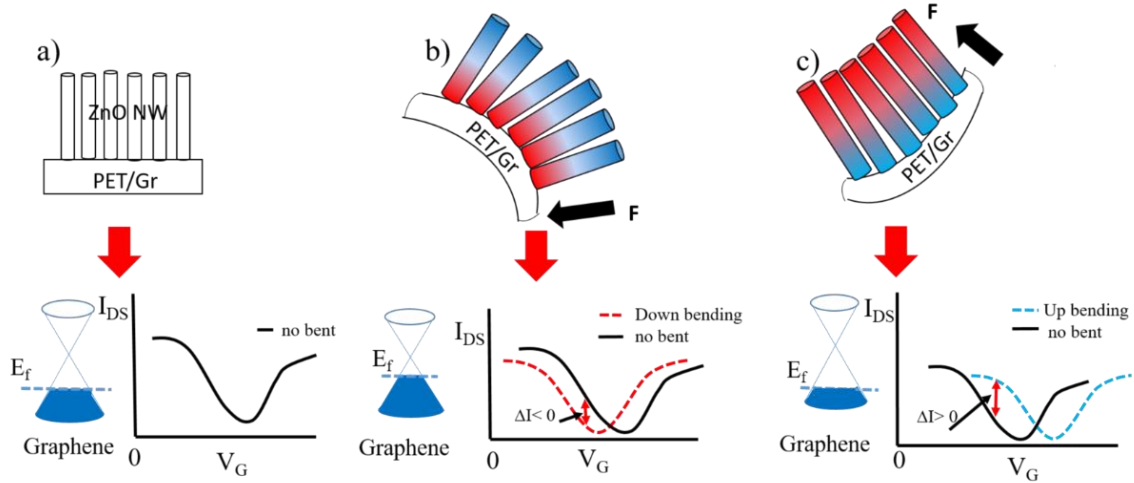


Figure 3.3.5 (a) Schematic of NWs on PET/Gr substrate at no bend situation (Top) and energy diagram of graphene along with IV characteristic curve (down). Similarly, (b) Down bending schematics (c) Up bending schematics.

Chapter 4

Inkjet Printing WO_3 and ZnO Nanocomposite Films

This chapter will discuss the performance of the surface texturing and heat treatment techniques utilized to solve coagulation of tungsten oxide and ZnO precursor inks and composite inks. It will do so by characterizing the photodetectors fabricated with this method utilizing a UV photodetector as the main device.

4.1 *Inkjet Printing WO_3 via Surface Texturing SiO_2 with ZnO QDs*

The device discussed here are two samples, one being WO_3 precursor (WO_3Pr) ink printed at room temperature on a textured surface and the other WO_3Pr printed on a textured surface at 50 °C, further details on the device fabrication and characteristics can be found in Sections 2.2.3 and 2.3.9.

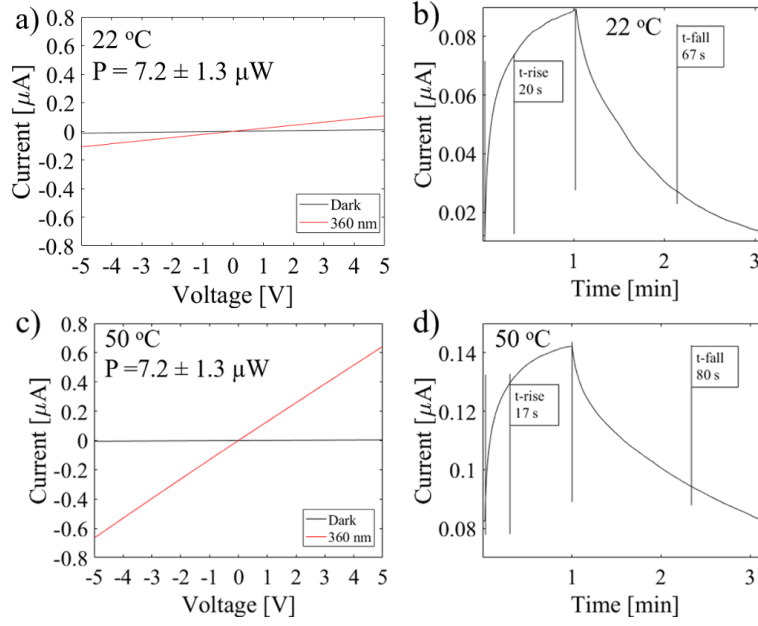


Figure 4.1.1 In (a) and (b) depict the IV curves and dynamic photoresponse of the room-temperature printed sample on ZnO QDs layer, respectively, whereas (c) and (d) include the IV curves and dynamic photoresponse of the sample printed on ZnO QDs layer at 50 °C. The incident light wavelength was 360 nm and its intensity $\sim 7.2 \pm 1.3 \mu\text{W}$ [42].

The current-voltage characteristic curve and dynamic photoresponse are shown in **Figure 4.1.1** for the devices of printed WO_3Pr on a ZnO QD textured SiO_2/Si surface at $\sim 22^\circ\text{C}$ (**Figure 4.1.1a-b**) and 50°C (**Figure 4.1.1c-d**), respectively. The photoresponsivity of the sample printed at room-temperature substrate is around $16.6 \pm 9.22 \text{ mA/W}$ and is approximately four times less than that of the heat assisted printing on ZnO QD layer with a photoresponsivity of $75 \pm 29 \text{ mA/W}$ at 5 V bias voltage. Using these responsivity values and the measured noise equivalent power (NEP), the specific detectivity $D^* = (A)^{1/2}/\text{NEP}$, where A is the area of the channel, can be obtained on WO_3 devices fabricated with the room-temperature printing and heated printing, respectively, as $1.99 \times 10^2 \text{ cm} \cdot \text{Hz}^{1/2}/\text{W}$ ($\text{NEP} = 7.90 \times 10^{-6} \text{ A/Hz}^{1/2}$) and $1.46 \times 10^2 \text{ cm} \cdot \text{Hz}^{1/2}/\text{W}$ ($\text{NEP} = 4.85 \times 10^{-5} \text{ A/Hz}^{1/2}$). The difference in responsivity of the room-temperature device by a factor of four could be due to

a thinner film than the film printed at 50 °C (**Figure 4.1.2**). The room-temperature printed sample shows an even thickness of 138 ± 40 nm and the heated surface shows a thickness of 273 ± 90 nm, notice the roughness is greater by over a factor of 2 (**Figure 4.1.2**).

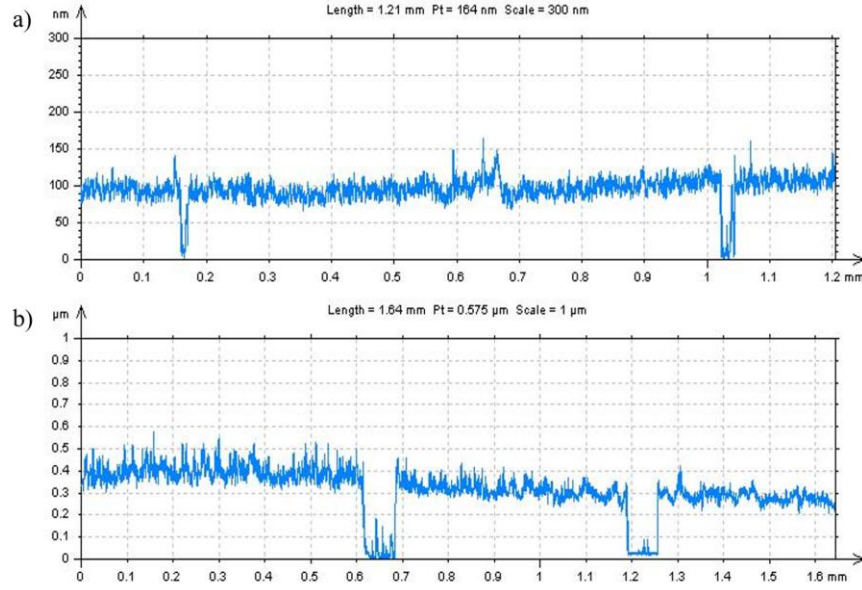


Figure 4.1.2 Depicted in (a) is a printed WO_3 precursor on a ZnO QDs textured SiO_2 surface at room-temperature and (b) at 50 °C. The profile was performed by making scratches and performing a profile to obtain the approximate depth of the films [42].

The heated printing can result in stronger localization of precursor on the channel rather than obtaining a thin evenly spread film. The room-temperature printing of WO_3 with ZnO QD texturing yields comparable quality of devices to our previous work without QD texturing at 50 °C with responsivity of approximately 24 mA/W at comparable power of 4.8 ± 0.9 μW without the quantum dot layer at a thickness of 150 nm [59]. The similar WO_3 device performance between the optimally heated printing without ZnO QDs and non-heated printing with ZnO QD textured layer shows the quality of the WO_3 is unaffected by the ZnO QDs layer. As shown in **Figure 4.1.3**, the ZnO QDs layer alters the surface roughness by an order of magnitude from that of the SiO_2/Si ,

and the surface chemistry, facilitating a uniform spread of the printed ink for WO_3 . However, the dynamic response stability of the samples are dramatically different (**Figure 4.1.4**). The poor dynamic performance can be attributed to more charge trapping and scattering from the cracking at the surface of the film due to the nonuniform films in heated printing.

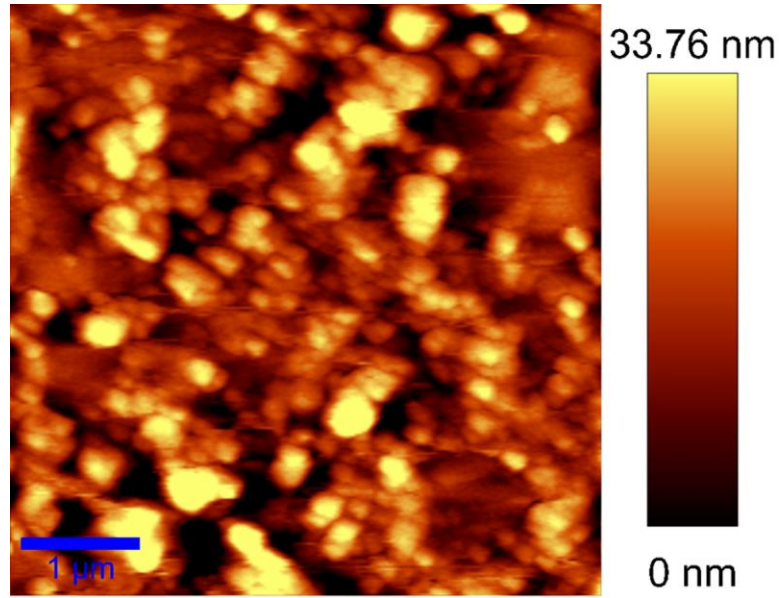


Figure 4.1.3 Atomic force micrograph of ZnO QDs seed layer printed on the SiO_2/Si substrate with surface roughness of approximately 9.39 nm [42].

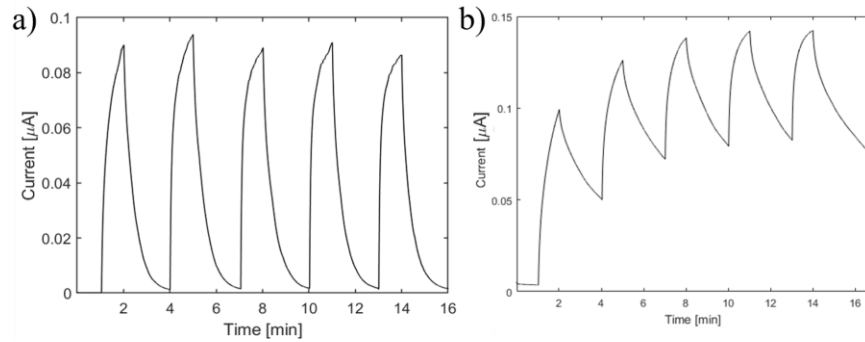


Figure 4.1.4 Dynamic performance of WO_3 device on ZnO QDs texture SiO_2 wafer printed at (a) room temperature and (b) at 50 °C, respectively [42].

In the case of the rougher nonuniform film the charge traps dominate, which can increase the photoresponsivity at the cost of dynamic performance [86, 87]. Both devices have comparable rise and fall times once the heated printed sample reaches a stable dynamic curve (**Figure 4.1.4**), for the room-temperature device there is a rise time and fall time of 20 ± 2.5 s and 67 ± 5.6 s, respectively, and for 50 °C device 17 ± 3.2 s and 80 ± 7.8 s, respectively. The rise and fall times is in the range of tens of seconds due to the absorption and desorption of oxygen similar to what is discussed for ZnO films. The fall time is longer than the rise time due to the charge traps and time needed for oxygen to reabsorb onto the surface to obtain the initial current [88, 89]. At a larger incident power, the rise time would be faster as there are more photons that can excite more charges to the conduction band (**Figure 4.1.5**).

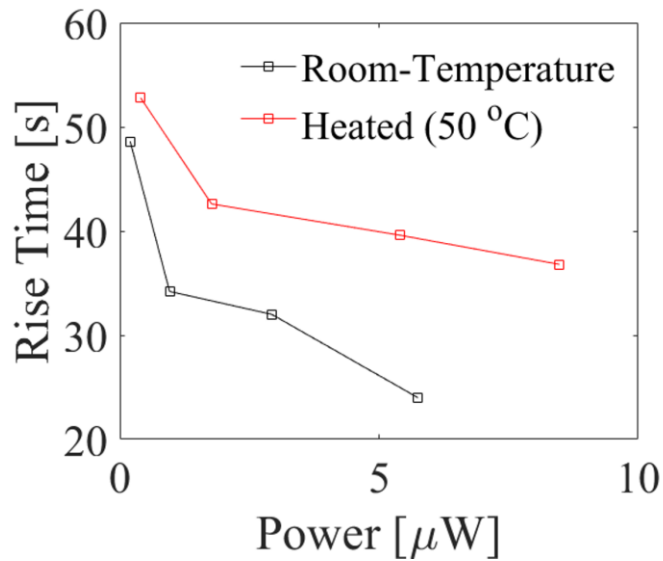


Figure 4.1.5 The rise-time of the room-temperature surface printed device (black), and the heated printing at 50 °C (red) as a function of power [42].

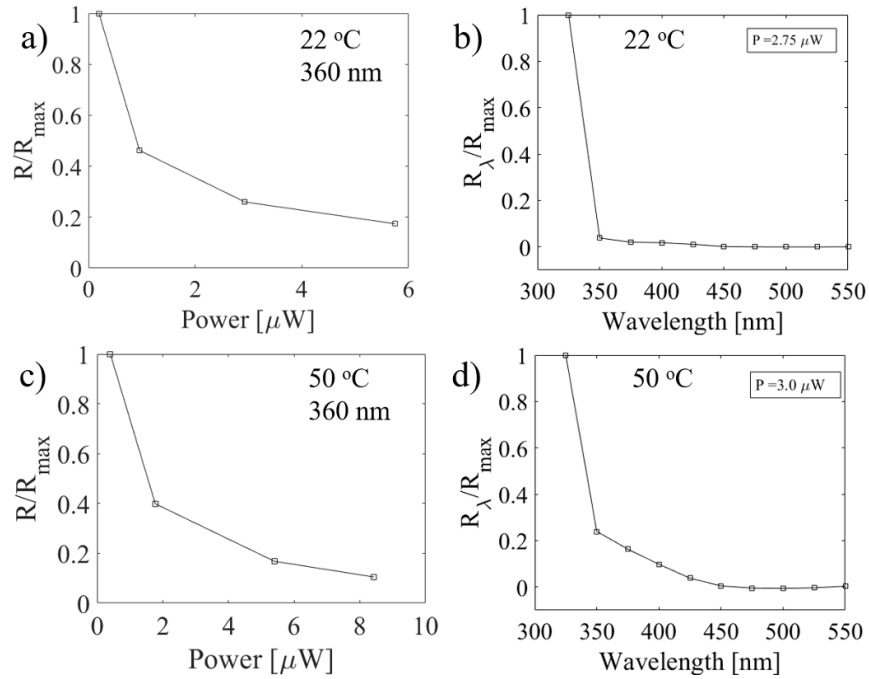


Figure 4.1.6 The responsivity as a function of power for room-temperature printed WO_3 precursor sample on ZnO QDs layer is shown in (a) along with the spectral (b). Similarly, the intensity as a function of power and spectral for WO_3 precursor ink printed on ZnO QDs layer at 50 °C is depicted in (c) and (d), respectively [42].

Lastly, the responsivity as a function of intensity and the spectral of the devices is depicted in **Figure 4.1.6**. The responsivity as a function of intensity of the room-temperature (**Figure 4.1.6a**) and the heated printing (**Figure 4.1.6c**) show comparable results, both show an inversely related response to increased power which begins to saturate at 6-9 μW at a wavelength of 360 nm. Interestingly, the spectral responsivity for the room-temperature printed sample (**Figure 4.1.6b**) shows a sharper band edge at around 360 nm as opposed to the broadened band edge of the 50 °C printed sample, which begins to curve around 450 nm (**Figure 4.1.6d**). The broadening is likely caused by defects in the crystal structure due to cracks and strain introduced by printing at an elevated temperature. While the performance of the printed WO_3 devices is promising, there is room for further improvement with better control of the WO_3 microstructure and device design. In

particular, a specific responsivity up to $0.066 \text{ A/W}\cdot\text{V}$ was recently reported in WO_3 devices made in atomic layer deposition [90, 91], suggesting the performance can be further improved by at least an order of magnitude.

4.2 Heat Assisted Printing of WO_3 Precursor and ZnO Precursors

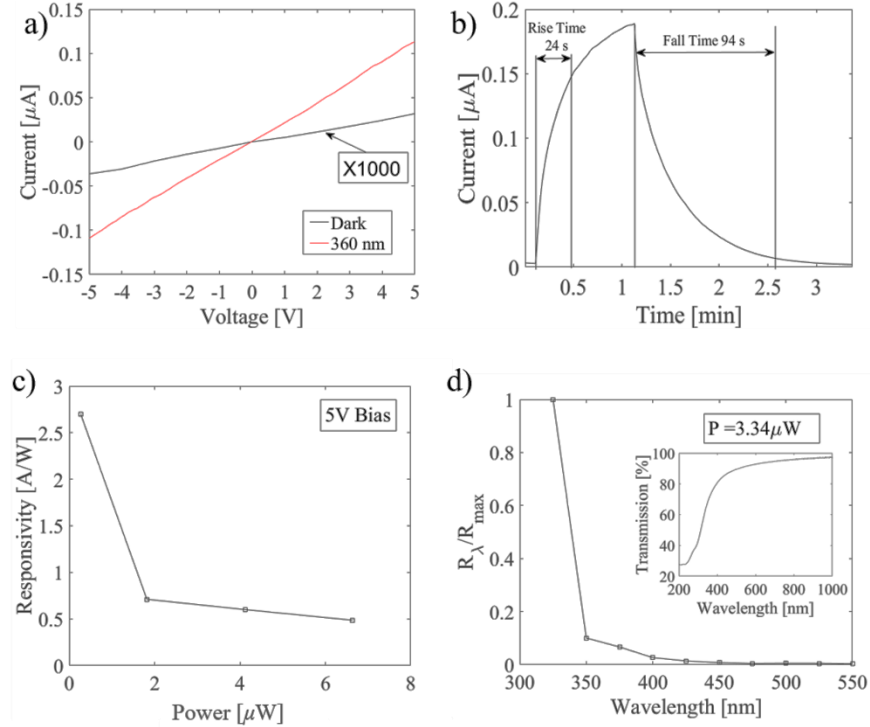


Figure 4.2.1 The current-voltage and dynamic characteristic curves for the 50°C are shown in (a) and (b), respectively, along with the responsivity as a function of power and wavelength in (c) and (d), respectively. Note that in (a) the dark current is scaled by 1000 for clarity [59].

This section just characterizes the photovoltaic properties of the WO_3 printed film on a regular SiO_2/Si surface at different heating and concentration and its fabrication and characterization can be found in Section 2.2.3 and Section 2.3.9, respectively. The photovoltaics were taken at a wavelength of 360 nm, since the bandgap for WO_3 is $\sim 3.2 \text{ eV}$, which is around 380 nm, a slightly smaller wavelength is chosen to account for binding and kinetic energy of the excitons. In **Figure**

4.2.1a is the current-voltage characteristic curve (IV curve) and depicts the linearity of the IV curves, which means the film follows Ohms law and has a constant resistance, indicating a stable film under light with a power of 4.93 μW . The on/off ratio of the IV curve depicted **Figure 4.2.1a** is about 3538, which is remarkable for practical applications requiring a high signal-to-noise ratio. **Figure 4.2.1b** depicts the dynamic photoresponse under UV light of 360 nm at a power of 4.93 μW . A rise time of 24 s and fall time of 94 s can be observed, with the typical range of rise time being 25-30 s and for the fall time is 90-120 s on the printed WO_3 devices. The power of the light was varied and the photoresponsivity was calculated for the respective light power at a wavelength of 360 nm, the results are shown in **Figure 4.2.1c**. The photoresponsivity decreases inversely as the power increases since the number of charges generated in the crystal is reaching saturation and the photocurrent reaches a constant value, resulting in a high quantum efficiency at lower light intensities as observed in other photodetectors [57, 62]. The highest photoresponsivity obtained in the printed WO_3 UV detector is 2.70 A/W at 5 V bias ($\sim 0.54 \text{ A/W}\cdot\text{V}$) at a power of 0.27 μW , which is the best so far achieved on WO_3 UV detectors. This photoresponsivity is better than recent reported results of WO_3 films of 0.17 $\mu\text{A/W}$ ($\sim 0.28 \mu\text{A/W}\cdot\text{V}$) [91], and $\sim 0.29 \text{ A/W}$ ($\sim 0.056 \text{ A/W}\cdot\text{V}$) [90]. **Figure 4.2.1d** shows the spectral responsivity and a band edge that begins around 375 nm, which is right around the expected band edge of 380 nm for WO_3 meaning the crystal obtained is indeed tungsten oxide. Inset in **Figure 4.2.1d** is the optical transmittance spectra of a uniform WO_3 -NP film on fused silica. A low absorption to visible light was observed with a sharp cut-off below $\approx 450 \text{ nm}$, corresponding to the intrinsic band gap of WO_3 at $\approx 2.8 \text{ eV}$ which is in agreement with the spectral response in **Figure 4.2.1d** [92].

4.3 Inkjet Printed Graphene Nanoplatelets/ZnO Precursor for UV Photodetection

Using graphene as the main conductor works great for high photoresponsivity photodetectors, but they suffer from large amounts of surface contamination and need chemical cleaning. This experiment avoids use of any cleaning and instead mixes the graphene nanoplatelets directly into the ZnO precursor for a ZnO/GnP bulk heterojunction film. The photocurrent as a function of the bias voltage is shown in **Figure 4.3.1a**, with the UV light source being 340 nm in wavelength at a power $P=4.6 \pm 0.3 \mu\text{W}$. In the photocurrent-voltage characteristic curves the photocurrent increases monotonically with the GnP concentration up to 20 mM, confirming the benefits of the ZnO/GnP Schottky junctions for efficient exciton dissociation and charge transfer. At higher GnP concentration of 30 mM, this benefit is reduced due to the GnP clumping. This trend can be seen clearly in the photoresponsivity as a function of GnP concentration in **Figure 4.3.1b**. The photoresponsivity was measured with a 5 V bias at the wavelength of 340 nm and power $P= 4.6 \pm 0.3 \mu\text{W}$. Specifically, the photoresponsivity increases from 0.20 A/W for the printed ZnO only device, to 0.22 A/W for 5 mM ZnO/GnP sample, and to 0.82 A/W for 20 mM ZnO/GnP. At the higher GnP concentration of 30 mM, it decreases to 0.71 A/W. The detectivity (D^*) as a function of voltage is also show in the **Figure 4.3.2** and shows a similar trend to the photocurrent as a function of voltage with the highest detectivity being the 20 mM GnP with $D^*=2.03 \times 10^{11} \text{ cm} \cdot \text{Hz}^{1/2} \cdot \text{W}^{-1}$ at a voltage bias of -5V. Here D^* is defined as, $D^* = R \sqrt{\frac{A}{i_n^2}}$, where A is the area, which for our device is 0.45 mm^2 , and R is the photoresponsivity and the root-mean-squared of the noise current is $(\overline{i_n^2})^{\frac{1}{2}}$. The mechanism responsible for the decrease in photoresponsivity can be seen in **Figure 4.3.1c** on the dynamic photoresponse measured on these four samples. Interestingly, the dark current for the three samples with lower GnP concentrations have comparable I_{Dark} while the sample with 30 mM GnP concentration has a considerably increased

I_{Dark} . This means the reduced I_{ph} in the ZnO/GnP nanocomposite sample with 30 mM GnP concentration is primarily caused by the higher I_{Dark} . The rise times (fall times) are determined from the time required to go from 10% to 90% (90% to 10%) of the photocurrent are depicted in **Figure 4.3.1d**. For the ZnO/GnP nanocomposite samples with for 0, 5, 20, 30 mM GnP concentrations, the rise/fall times are 9.6 s/17.2 s, 13.5 s/10.8 s, 20.6 s/15.7 s, and 16.2 s/23.6 s. Basically, the rise and fall times remain comparable at zero or low GnP concentrations. The moderately increased rise and fall times at higher GnP concentrations of 20 and 30 mM may be associated with large ZnO/GnP interfaces for charge trapping and a highly conductive percolation path through GnPs. This is caused by the GnP becoming a dominant conducting materials at higher GnP concentration much like other graphene based photoconductors the high conductivity of graphene can cause charges to cycle through the material much easier and allows for a longer photoconductive decay.

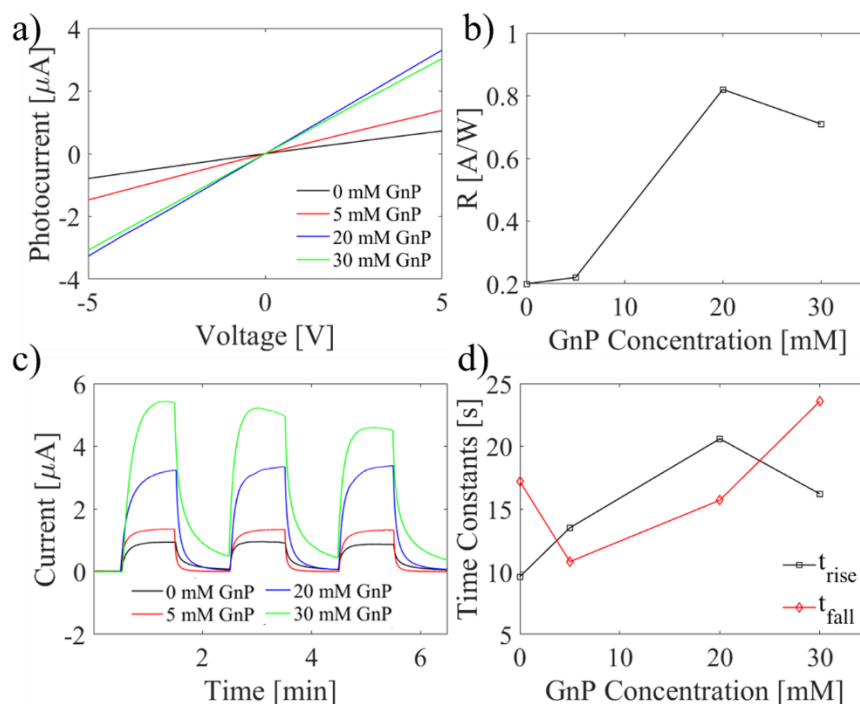


Figure 4.3.1 (a) Photocurrent as a function of the bias voltage and (b) responsivity measured on ZnO/GnP nanocomposited films with 0, 5 mM, 20 mM and 30 mM GnP concentrations,

respectively. (c) Dynamic UV photoresponse (340 nm) at a 5V bias of the same four samples in (a), and (d) the extracted rise and fall times from (c) for the four samples [58].

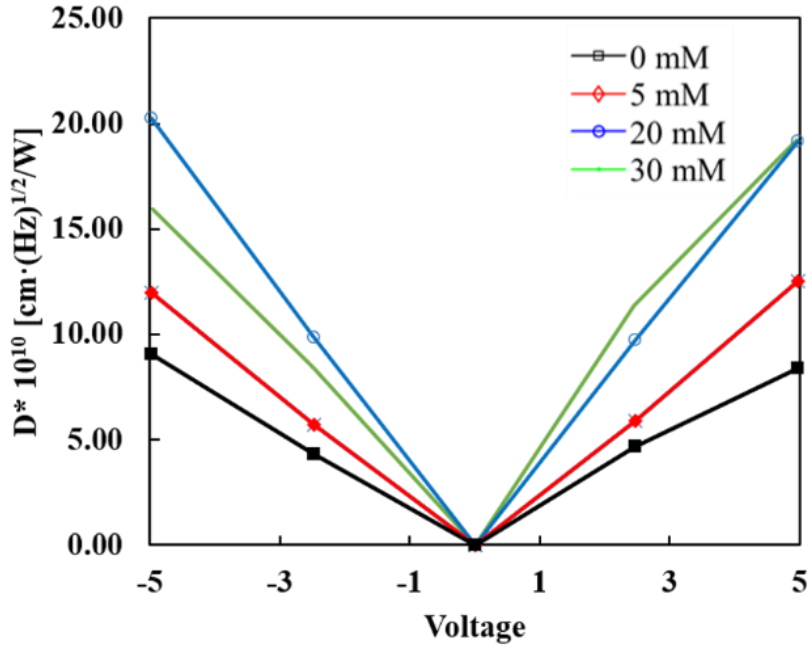


Figure 4.3.2 Detectivity as a function of voltage of the ZnO/GnP film at different concentrations of GnP 0 mM, 5 mM, 20 mM, and 30 mM [58].

The photoresponsivity as a function of the UV light power is depicted in **Figure 4.3.3a**. The best performance can be observed on the ZnO/GnP nanocomposite samples with GnP concentration of 20 mM. While the sample with GnP concentration of 30 mM suffers an increased I_{Dark} , it considerably outperforms the samples with low GnP concentration of 5 mM and without any GnP. The ZnO/GnP nanocomposite samples of 20 mM GnP concentration shows the highest photoresponsivity of 2.2 A/W at 0.2 μ W at a wavelength of 340 nm, which is 2.8 times and 4.5 times higher than that of the samples with 0 mM (0.78 A/W) and 5 mM (0.41 A/W) GnP concentrations at comparable UV light powers of 0.20 μ W and 0.27 μ W, respectively. It should be noted that the photoresponsivity decreases with increasing light power similar to all previous devices which is expected since it is just a reduction in quantum efficiency at higher intensity [21,

59]. In **Figure 4.3.3b**, the spectral photoresponsivity and is normalized to the maximum responsivity value for feasibility of comparison for the samples with 0 mM and 20 mM GnP concentrations are compared, and shows a increase around 380 nm which is anticipated from the crystalline ZnO with a bandgap of 3.26 eV. In **Figure 4.3.3c**, a series of dynamic photoreseponse curves taken on a ZnO/GnP nanocomposite films of 20 mM GnPs over the course of approximately 17.7 weeks are depicted. A clear trend of elongation of rise and fall times can be observed between the solid black and red curves. This issue can be attributed to the ZnO surface contamination by air molecule attachment. To alleviate this issue, the ZnO/GnP device was treated with UTA 800 °C for 2 seconds [62]. Remarkably, the optoelectronic performance was resumed after the UTA as illustrated in the dynamic response comparable (blue curve) to the initial red curve. In **Figure 4.3.3c**, the dynamic response curves on a ZnO/GnP nanocomposite sample with PMMA printed on top as passivation to ambient is also included. The reduced impact of the ambient exposure can be observed. To further investigate, the dark current and photocurrent are plotted as a function of time in **Figure 4.3.3d** where it is observed that the photocurrent and dark current increase significantly from initial fabrication to the 17.7 weeks with no passivation. After UTA indicated by the dashed vertical line in **Figure 4.3.3d** it is observed that the dark current and photocurrent return to comparable values, however a few weeks after the photocurrent increases significantly again while maintaining a low dark current, which might be due to the PMMA slowly aging and drying over time. As time increases the dark current more or less stays constant while the photocurrent shows an exponential decay and then begins to level off. Interestingly, the photocurrent levels off to a larger photocurrent than it had previously obtained before UTA and passivation, while also maintaining a relatively stable dark current, which indicates methods of

passivation such as with PMMA can offer a viable method for stable packaging of devices that show instability in ambient air.

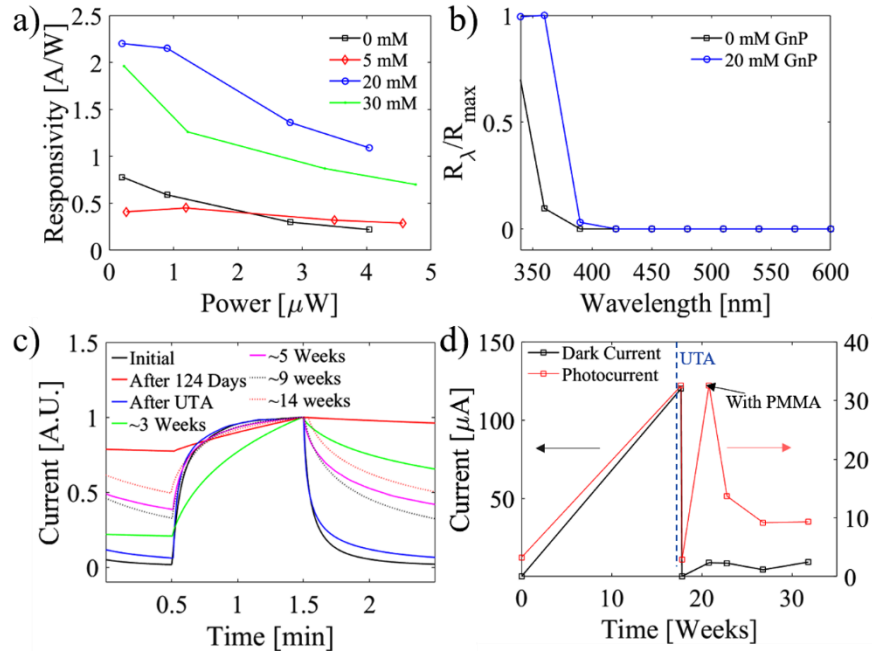


Figure 4.3.3 In (a) the photoresponsivity as a function of power of the ZnO/GnP nanocomposite photodetectors with 0 mM 5 mM, 20 mM and 30 mM GnP concentrations. Similarly, we have the (b) spectral photoresponse comparing the best result to pure ZnO, (c) dynamic photoresponse, and (d) dark current and photocurrent as a function of time before and after the UTA treatment. PMMA passivation was applied to the sample after UTA [58].

Chapter 5

Inkjet Printing Quantum Dots on Graphene for Single and Multiwavelength Photodetectors

5.1 *Single Quantum Quantum Dot and Graphene Photodetectors*

In this section we will begin discussing purely quantum dot/graphene nanohybrid devices that really heavily on the long life time of charges in quantum dots and the extremely high charge mobility associated with graphene. In **Figure 5.1.1a** is the schematic diagram of a graphene field effect transistor (GFET) with inkjet printed ZnO QDs on a channel of approximately 7 microns, there is a back-gate voltage V_{bg} and a source-drain voltage V_{sd} with a 90 nm SiO_2 layer and a heavily p-type doping of the Si layer. When the ZnO QDs are illuminated with the UV light they experience excitation and the electrons transfer over to graphene while leaving behind holes resulting in a electron doping of graphene from the electrostatic gating caused by the holes remaining in the QD layer (**Figure 5.1.1b**). The ZnO QDs were synthesized using a hydrothermal method as described in Section 2.1.3 and after fabrication there is a shell of unreacted zinc acetate shell that is often unreacted (**Figure 5.1.1c**), this shell provides an energy barrier that electrons have to overcome and as a result charge transferred is hindered. After approximately a month the zinc acetate shell degrades and what is left is the ZnO QDs (**Figure 5.2.1d**).

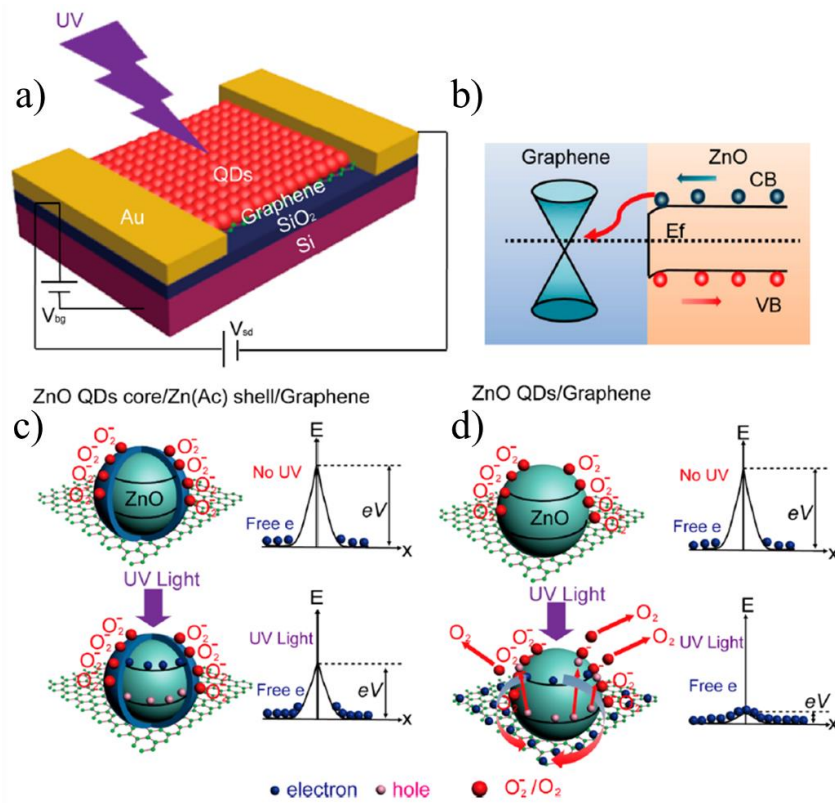


Figure 5.1.1 In (a) is the device schematic for ZnO QDs printed on graphene for a graphene field-effect transistor, and (b) shows the charge transfer schematic for the device. In (c) and (d) is the ZnO QDs right after fabrication and after aging, respectively [21].

In **Figure 5.1.2a** is the dynamic curves the ZnO QDs GFETs of the different stages of the ZnO QDs after fabrication (blue), partially aged (red), and fully aged (black). These show that indeed there is a charge barrier preventing charge transfer from moving over to graphene and the zoom in of the blue and red curves are shown in **Figure 5.1.2b**. As can be seen in the blue dynamic curve, there is nearly no response however after the shell has had some time to degrade a signal starts to appear which is shown in red. Using the fully aged ZnO QDs the rise and fall times are measured giving a value of 5.0 s and 85.1 s, respectively (**Figure 5.1.2c**). The photoresponsivity as a function of wavelength is shown in **Figure 5.1.2d** given by the black curve and the dashed red line is the absorption of the ZnO QDs on glass. The spectral and transmission both show agreeable results

indicating that the ZnO QDs have a band edge around 360 nm which corresponds to a bandgap of 3.44 eV for highly crystalline ZnO.

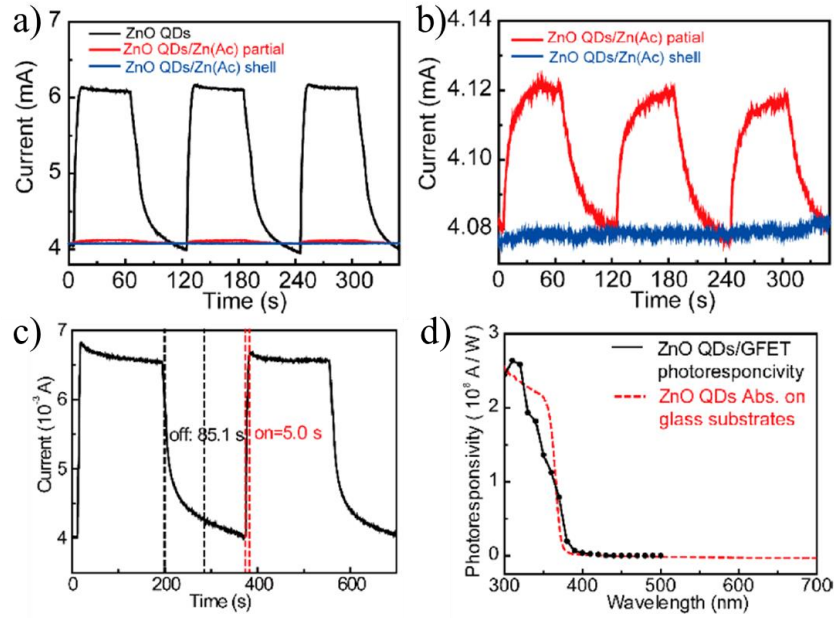


Figure 5.1.2 (a) Dynamic performance of the ZnO QDs after aging (black), partial aging (red), and after fabrication (blue), and (b) is the red and blue curves zoomed in on. In (c) is the dynamic performance with the rise and fall times, and (d) the spectral curve and the transmission of the ZnO QDs [21].

Lastly, is the photoresponsivity and gain as a function of the light intensity at different constant voltage bias of 1, 5, and 10 V is shown in **Figure 5.1.3a** where the solid lines correspond to the photoresponsivity on the left axis and the dashed lines correspond to the gain on the right axis. It can be seen that with increasing light intensity the quantum efficiency is reduces inversely, while if the light intensity is kept constant and the voltage bias V_{sd} is increased it increases almost logarithmically likely because of the increased transit time and thus the rise in gain (**Figure 5.1.3b**). In **Figure 5.1.3c** is the D^* as a function of UV light intensity (solid lines) and as a function of voltage bias (dashed lines) and shows that it has a similar inverse relationship because of the

detectivity being proportional to the photoresponsivity and similarly is it logarithmically related to the voltage bias.

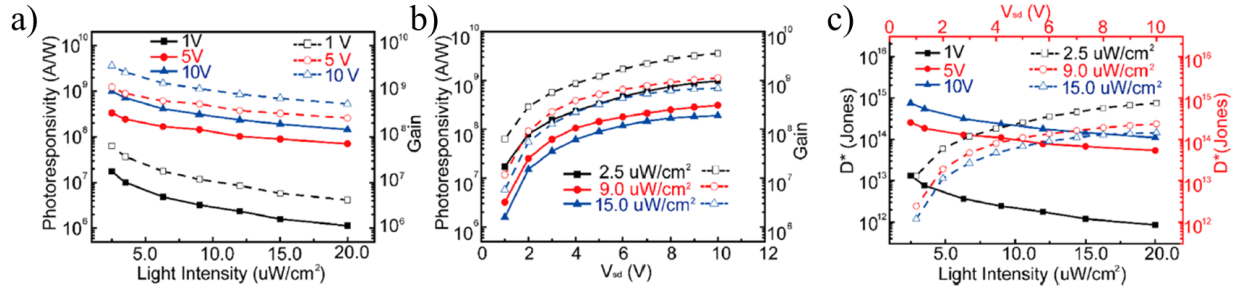


Figure 5.1.3 (a) photoresponsivity (solid lines) and gain (dashed lines) as a function UV light intensity at a 340 nm wavelength at different V_{sd} of 1, 5, and 10 V. (b) photoresponsivity and gain as a function of different light intensities with changing V_{sd} and (c) the D^* as a function of UV light intensity and V_{sd} [21].

It should be noted that the high electron mobility, small channel size, and large lifetime of charge in the ZnO QDs and slow return of oxygen to the ZnO QD surface the ZnO QDs not only gain 2 electron from oxygen absorption desorption effect this also results in a very long lifetime of the electrons in the graphene channel, as a result the photoresponsivity can reach as high as 1.8×10^8 A/W and detectivity exceeding 10^{14} jones.

5.2 Inkjet Printed Quantum Dots for Multiwavelength Pixelated Photodetection

The optoelectronic properties of the three-pixelated photoconductors were tested at wavelengths of 340 nm, 550 nm, and 900 nm, for PbS QDs, FeS₂ NCs, and ZnO QDs, respectively. The dynamic photoresponses on the different channels are depicted in **Figure 5.2.1**. The dynamic photoresponse of the ZnO-QD/graphene channel is measured at a 1.0 V bias and 340 nm wavelength (**Figure 5.2.1a**). The rise and fall times are defined as the time for the photocurrent to

rise from 0% to 80% and decay from 100% - 20% of the maximum photocurrent, respectively. The rise and fall times of the ZnO-QD/graphene channel is 2 s and 29 s, respectively. This result is comparable and slightly better than previously reported single-channel ZnO-QDs/graphene devices with 5 s and 85.1 s for the rise and fall times, respectively, which is likely the result of longer aging of the ZnO-QDs while kept in storage [21]. However, the response of ZnO-QDs/graphene channel is considerably slower than the PbS-QD/graphene and FeS₂-NC/graphene channels most probably caused by the MPA ligand exchange that passivates the surface of the PbS-QD and FeS₂-NC and the interfaces of the QD-QD junctions, as well as the PbS-QD/graphene and FeS₂-NC/graphene heterojunctions to eliminate/reduce the charge traps [21, 51, 52]. Specifically, the rise and fall time constants of the PbS-QD/graphene channel is 0.3 s and 3.2 s at a 1.0 V bias at 900 nm illumination (**Figure 5.2.1b**). In fact, similar rise and fall times of 0.01 - 0.26 s and 1 - 1.7 s, respectively, have been reported previously on PbS/graphene photodetectors [93, 94]. In addition, ZnO-QD/graphene (**Figure 5.2.1a**) and PbS-QD/graphene (**Figure 5.2.1b**) show a asymmetric rise and fall in dynamic response indicating other process such as charge traps, which indicate that there is a room for improvement via eliminating charge traps. Interestingly, the FeS₂-NC/graphene channel approximately has a symmetric rise and fall time of 0.20 s and 0.24 s at 1.0 V bias at a wavelength of 550 nm (**Figure 5.2.1c**). Furthermore, the printed FeS₂-NC/graphene channel shows better results than previous work which demonstrated a rise/fall time of 0.6 s/7.6 s, respectively [52]. The considerably shorter response times in PbS-QD/graphene and FeS₂-NC/graphene channels as compared to the ZnO-QD/graphene counterpart may be attributed to the MPA ligand exchange applied to the former cases, which reduces the charge traps by the surface defects of the sensitizers (QD and NC), the QD-QD (or NC-NC) and QD (or NC)/graphene

junctions, whereas ZnO has oxygen absorption and desorption, which contributes to the rise and fall time by electron localization and delocalization [21, 52].

The channels also show a linear trend of photoresponsivity (R) with a varying voltage bias as shown in **Figure 5.2.1d**, with a photoresponsivity of 7.41 A/W (1.85 A/W·V) for the FeS₂-NC/graphene channel measured with a wavelength of 550 nm and a power of 18.1 μ W and with an external quantum efficiency (EQE) value of 1,670%. Similarly, the PbS-QD/graphene channel has a photoresponsivity of 6.81 A/W (1.70 A/W·V) and an EQE of 940% at a wavelength of 900 nm at a power of 27.5 μ W, and finally the ZnO-QDs/graphene channel has a photoresponsivity of 97.5 A/W (24.4 A/W·V) at a wavelength of 340 nm and a power of 6.66 μ W and with an EQE value of 35,580%. The performance of the PbS-QDs/graphene device is comparable to the previous report of \sim 8.4 A/W with similar graphene channel dimension [95]. However, the ZnO-QDs/graphene channel has significantly improved performance than previously reported (\sim 0.5 A/W) [96]. Furthermore, the high performance of the inkjet printed FeS₂ NC on graphene represents the first report with a graphene channel length of a few hundred micrometers. Considering a shorter graphene channel would lead to higher photoconductive gain and hence higher photoresponsivity as shown in the previous works on the FeS₂-NC/graphene, PbS-QDs/graphene and ZnO-QDs/graphene [21, 51, 52, 93, 94], which means further improvement can be obtained on the printed pixelated QD/graphene photoconductors through optimization of the graphene channel.

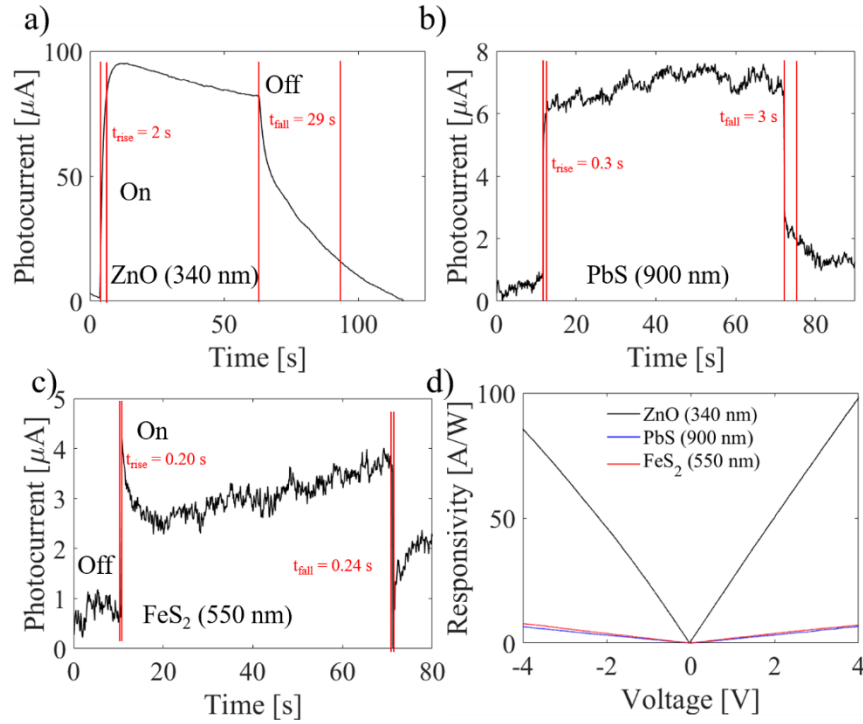


Figure 5.2.1 Dynamic photoresponse to light “On” and “off” on (a) ZnO-QD/graphene; (b) PbS-QD/graphene, and (c) the FeS₂-NC/graphene photoconductor channels. (d) photocurrents as a function of the bias voltage in the three channels [53].

The photoresponsivity as a function of the light power are depicted at wavelengths of 340 nm, 550 nm, and 900 nm (**Figure 5.2.2a-c**) at a 1.0 V bias and the normalized spectral curve is depicted in **Figure 5.2.2d**. Only ZnO/graphene and PbS/graphene is measured for 340 nm, FeS₂ was also measured but displayed a poor dynamic response to UV light and so was not included. Similarly, ZnO mainly shows noise in wavelengths larger than ~ 380 nm and was not included in the measurements for 550 nm and 900 nm. ZnO shows a photoresponsivity inversely related to the power and is comparable to the measured photoresponsivity from the photocurrent-voltage characteristics curve, which gives ~ 24.4 A/W for 1.0 V bias. Similarly, PbS QDs also shows an inversely related trend at all wavelengths however, the photoresponsivity is about as half as much in this measurement as compared to what was measured from the current-voltage characteristic

curve. This is likely caused by some degradation attributed to oxidation of the PbS particles, and similar behavior is seen in FeS₂. Looking at the spectral curves, they show that the ZnO QDs has a bandedge at ~360 nm, while PbS QDs and FeS₂ NCs are broadband nanomaterials that absorb light at all wavelengths. In addition, the spectral curve shows a similar broad peak for FeS₂ around 800 nm with a steady decrease as seen in previous work [52]. For PbS there is a similar small peak slightly shifted to the right of FeS₂ and then an increase in UV absorption, while ZnO has no absorption then begins absorption around 380 nm as usual.

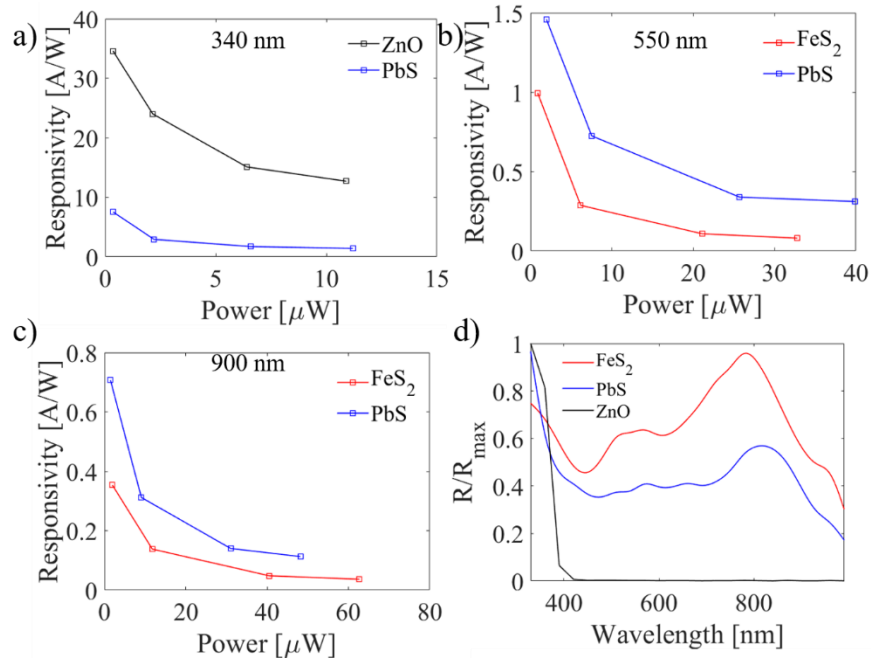


Figure 5.2.2 The photoresponsivity as a function of power is depicted in (a), (b) and (c) along with the normalized spectral curve shown in (d) [53].

In addition, the tandem device structure shown in **Figure 5.2.3** is a multi-layer QD vdW nanohybrid structure, which differs from conventional tandem photovoltaics based on p-n junctions. Moreover, the band-edge alignment shown in **Figure 5.2.3a** facilitates exciton dissociation and charge transfer through vdW heterojunction of ZnO-QDs/PbS-QDs/graphene from the larger bandgap ZnO-QD top layer to the lower bandgap PbS-QD bottom layer then to

graphene. A major obstacle in the Van der Waals (vdW) heterostructure optoelectronics is in controlling the vdW interface to eliminate any unwanted interface contaminants. In the ZnO-QDs/PbS-QDs/graphene tandem devices we investigate in this work, the controlling of the QD-QD junctions is one such example and should be addressed in future research for optimal performance of this kind of tandem devices. Both physical and chemical methods may be promising to address the QD-QD junction issue. For example, an ultrafast thermal annealing (UTA) was found to generate nanoscale junctions between oxide nanoparticles and improves the electron transport properties [62, 97]. On the other hand, certain ligands such as mercaptopropionic acid (MPA) have been found to improve the QD-graphene vdW junctions, resulting improved photoresponse and shortened response time by orders of magnitude [21, 52]. For our ZnO-QDs/PbS-QDs/graphene tandem photodetector shown schematically in **Figure 5.2.3b**. We see through the energy diagram in **Figure 5.2.3a** that the wide-bandgap energy of ZnO will allow lower energy photons to pass through and allow the PbS layer to collect the incident photons, and ZnO and PbS QDs can both absorb high energy photons. However due to the stacking of QD layers shown in **Figure 5.2.3b**, charges cannot move to graphene layer from the ZnO QD layer without passing through the PbS QD layer (**Figure 5.2.3a-b**), this can result in an increase dynamic response time. In **Figure 5.2.3c** under 900 nm and 340 nm we see dramatically different response with a positive photocurrent in the former and a negative photocurrent in the latter. In addition, the dynamic response at 900 nm is slower than in the single QD (or NC)/graphene devices with the rise and fall times, respectively, being increased up to 12.1 s (3.0 s) and 40.3 s (4.8 s) (**Figure 5.2.3d**). This slower photoresponse may be attributed to the increased number of QD (or NC) layers since photocarriers formed on the top of the QD (or NC) layers must travel across multiple QD-QD junctions before reaching the graphene channel, as well as surface defects on QDs (or

NCs) would result in charge traps at the QD-QD junctions and slow down the response. In **Figure 5.2.3e** is the response to 340 nm light and there is no appreciable rise or fall times to the curve and exhibiting a negative photocurrent response. Lastly, a spectral responsivity from 330 nm to 900 nm wavelengths is shown in **Figure 5.2.3f**. Interestingly, the variation of the responsivity is moderate due to complementary bandgaps of ZnO and PbS QDs despite an overall lower responsivity and slower photoresponse as discussed above. This means the tandem devices can be promising for broadband photodetection if the QD-QD junctions can be improved to optimize the charge transfer and minimize charge trapping. The differences in response could be attributed to a shift in Dirac voltage of graphene. Depicted in **Figure 5.2.3f** is the spectral response and the inset is a schematic of the Dirac voltage shift. As shown, a positive photoresponse can be seen at longer wavelengths from visible to infrared while a negative photoresponse is shown in the UV spectrum. This means the charges trapped in the PbS-QD layer under longer wavelength illumination are electrons since holes will be transferred to graphene, providing a negative gate [51], which lowers the graphene Fermi energy away from the Dirac point (red curve in the inset in **Figure 5.2.3f**). In the UV spectrum, both PbS-QD and ZnO-QD layers are active and a transition from positive to negative photoresponse occurs at about 355 nm. This may result from mobile electrons in the ZnO QDs recombining with the holes in the PbS-QD layer (red dashed lines in **Figure 5.2.3a-b**) preventing holes from transferring to graphene [21]. In addition, the electrons in the PbS-QD layer may transfer to the now empty energy states in the ZnO conduction band and holes can move to the valence band of PbS-QD layer, resulting in more holes being trapped in the ZnO/PbS film and hence a positive gating of the graphene layer (blue curve inset in **Figure 5.2.3f**). The photoresponsivity at the different wavelengths of the tandem structure at 900 nm and 340 nm illumination was 0.67 A/W and 20.8 A/W at 55 μ W and 10.9 μ W, respectively, with EQE values

of 90% and 7,590%. The poorer performance of the tandem structure can be contributed to the poor interface between QDs caused by oxidation and ligands at the interface. This poor interface results in lower photoresponsivity and slow dynamic performance. In addition, the alignment of the ZnO and PbS energy bands results in strange behavior caused by the proposed dynamic charge exchange between the different active and inactive layers of the ZnO QDs and PbS QDs.

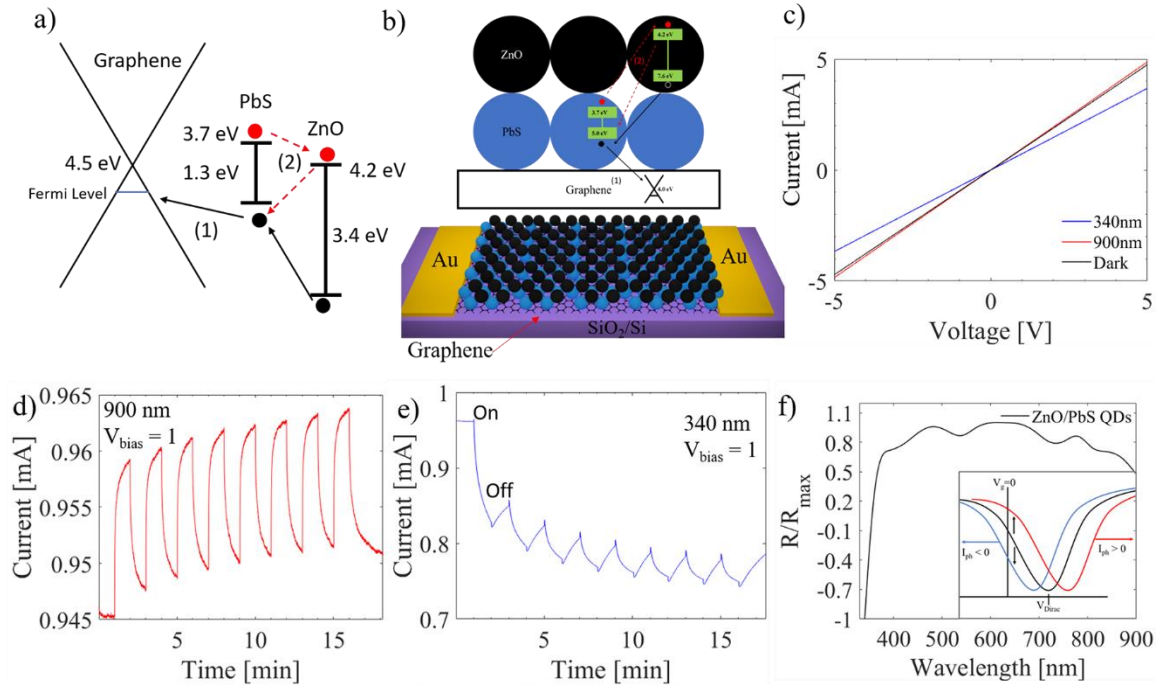


Figure 5.2.3 (a) Energy band edge diagram of a ZnO/PbS/Graphene tandem structure, and a graphic shown in (b). In (c) are the current-voltage characteristic curves, (d) dynamic response to 900 nm, (e) 340 nm and (f) spectral photoresponse of the tandem device from 330 – 900 nm. Inset of (f): positive photoresponse (from black to blue) at a longer wavelength illumination when only PbS-QD layer is active and negative photoresponse at shorter wavelength (blue) illumination when both ZnO-QD and PbS-QD layers are active [53].

Chapter 6

Conclusions and Future Work and Prospects

This thesis has demonstrated that high performing photodetectors can be accomplished with inkjet printing. Certain issues encountered are addressed, involving but not limited to, maintaining nanoscale feature sizes, hydrophobicity of surfaces, and interface engineering between differing quantum dots and graphene. For example, nanoscale sizes are accomplished through controlling the nucleation density of ZnO NWs and incorporating ZnO QDs into ZnO precursor ink. The nanoscale features allowed for a larger electron depletion effect through oxygen absorption. The hydrophobicity of SiO₂/Si wafers are dealt with in two ways. The first method involved inkjet printing ZnO QDs onto the SiO₂/Si surface for surface texturing, which resulted in being able to print at room temperature. Second, the surface of SiO₂/Si wafer was also heated to 50 °C so that the ink can be localized and dried before coagulating into droplets. The interface of printed quantum dots also encountered their own problems. The PbS and FeS₂ quantum dots have large ligands attached to the surface from the chemical synthesis. These large ligands block charge transfer, so they were removed with a ligand exchange process and replaced for shorter ligands that assisted in charge transfer. In addition, ZnO QDs have an unreacted insulating shell after being synthesized and required aging to fully form ZnO QDs. These improvements resulted in several orders of magnitude improvement in response time and photoresponsivity.

The devices also had an improved performance through the underlying physics of the nanomaterials, such as, surface charge depletion, high charge mobility of graphene, and the long charge life time of confined charges in the quantum dots. The nanoporosity of the ZnOPrQDs film

down to the Debye length allowed for full electron depletion through oxygen absorption, as a result, the photoresponsivity was increased two orders of magnitude. The high charge mobility of graphene combined with the long life time of the quantum dots printed onto the graphene channel resulted in extremely high gain for both GFET devices and photoconductor devices. Lastly, using a graphene nanoplatelet and ZnO precursor composite to print a heterostructure film resulted in efficient charge separation as a consequence of the graphene/ZnO Schottky interface. In addition, the graphene ZnO precursor composite devices can be fabricated without any cleaning and further modifications. The composite film also allows for a photoconductor network of graphene nanoplatelets to assist in photoconduction under UV excitation.

In conclusion, although the ultimate goal to fully integrate inkjet printed novel materials with CMOS was not fully achieved, significant steps were taken toward this development. There still remains two main issues that need to be addressed. First, CMOS has a thermal budget that is very strict, and if the thermal budget is exhausted the pn junctions in CMOS will malfunction. Second, wet transfers and chemical cleaning of graphene and quantum dots can contaminate the CMOS chip. A possible solution compatible with industry standards is laser ablations and laser machining/writing. Ultrafast high powered lasers are very versatile tools in their uses, since they can be used to clean surfaces, melt material, vaporize material, and induce reactions in materials. An ultrafast laser would be able to anneal and induce a reaction in printed precursors, which would allow for localized heating without damaging a CMOS chip. In addition, the ultrafast laser could also be used to clean the surface of materials like graphene or quantum dots with the proper focusing and precision. This is only one option toward incorporating new novel nanomaterials with CMOS. Moreover, there is still room for optimizing the material synthesis and fabrication. In particular, the graphene and quantum dots also can be used in flexible applications, which is

outside the scope of CMOS, making these materials interesting for more research and development.

References

- [1] A. M. Hussain and M. M. Hussain, *CMOS-Technology-Enabled Flexible and Stretchable Electronics for Internet of Everything Applications*. Advanced Materials, 2016. **28**: p. 4219-4249.
- [2] H. Iwai, *Future of nano CMOS technology*. Solid-State Electronics, 2015. **112**: p. 56-67.
- [3] S. E. Thompson and S. Parthasarathy, *Moore's law: the future of Si microelectronics*. Materials Today, 2006. **9**(6): p. 20-25.
- [4] J. W. Gardner, P. K. Guha, F. Udrea, and J. A. Covington, *CMOS Interfacing for Integrated Gas Sensors: A Review*. IEEE Sensors Journal, 2010. **10**(12): p. 1833-1848.
- [5] F. Xia, H. Wang, D. Xiao, M. Dubey, and A. Ramasubramaniam, *Two-dimensional material nanophotonics*. Nature Photonics, 2014. **8**(12): p. 899-907.
- [6] C. Xie, Y. Wang, Z.-X. Zhang, D. Wang, and L.-B. Luo, *Graphene/Semiconductor Hybrid Heterostructures for Optoelectronic Device Applications*. Nano Today, 2018. **19**: p. 41-83.
- [7] D. Y. Guo, C. X. Shan, S. N. Qu, and D. Z. Shen, *Highly sensitive ultraviolet photodetectors fabricated from ZnO quantum dots/carbon nanodots hybrid films*. Sci Rep, 2014. **4**: p. 7469.
- [8] Q. Zhang, J. Jie, S. Diao, Z. Shao, Q. Zhang, L. Wang, W. Deng, W. Hu, H. Xia, X. Yuan, and S.-T. Lee, *Solution-Processed Graphene Quantum Dot Deep-UV Photodetectors*. ACS Nano, 2015. **9**: p. 1561-1570.
- [9] X. Xu, J. Chen, S. Cai, Z. Long, Y. Zhang, L. Su, S. He, C. Tang, P. Liu, H. Peng, and X. Fang, *A Real-Time Wearable UV-Radiation Monitor based on a High-Performance p-CuZnS/n-TiO₂ Photodetector*. Adv Mater, 2018. **30**(43): p. e1803165.

- [10] K.-Y. Shin, J. S. Lee, and J. Jang, *Highly sensitive, wearable and wireless pressure sensor using free-standing ZnO nanoneedle/PVDF hybrid thin film for heart rate monitoring*. Nano Energy, 2016. **22**: p. 95-104.
- [11] Y. Zhang, J. Zhai, and Z. L. Wang, *Piezo-Phototronic Matrix via a Nanowire Array*. Small, 2017. **13**(46).
- [12] A. K. Geim and K. S. Novoselov, *The rise of graphene*. Nature Materials, 2007. **6**: p. 183-191.
- [13] M. Alamri, M. Gong, B. Cook, R. Goul, and J. Z. Wu, *Plasmonic WS₂ Nanodiscs/Graphene van der Waals Heterostructure Photodetectors*. ACS Appl Mater Interfaces, 2019. **11**(36): p. 33390-33398.
- [14] M. Buscema, D. J. Groenendijk, S. I. Blanter, G. A. Steele, H. S. van der Zant, and A. Castellanos-Gomez, *Fast and broadband photoresponse of few-layer black phosphorus field-effect transistors*. Nano Lett, 2014. **14**(6): p. 3347-52.
- [15] X.-L. Li, W.-P. Han, J.-B. Wu, X.-F. Qiao, J. Zhang, and P.-H. Tan, *Layer-Number Dependent Optical Properties of 2D Materials and Their Application for Thickness Determination*. Advanced Functional Materials, 2017. **27**(19): p. 1604468.
- [16] Q. Liu, B. Cook, M. Gong, Y. Gong, D. Ewing, M. Casper, A. Stramel, and J. Wu, *Printable Transfer-Free and Wafer-Size MoS₂/Graphene van der Waals Heterostructures for High-Performance Photodetection*. ACS Appl Mater Interfaces, 2017. **9**(14): p. 12728-12733.
- [17] D. Reddy, L. F. Register, G. D. Carpenter, and S. K. Banerjee, *Graphene field-effect transistors*. Journal of Physics D: Applied Physics, 2012. **45**(1): p. 019501.
- [18] D. Yu, Y. Zhang, and F. Liu, *First-principles study of electronic properties of biaxially strained silicon: Effects on charge carrier mobility*. Physical Review B, 2008. **78**(24).

- [19] S. T. Meyers, J. T. Anderson, C. M. Hung, J. Thompson, J. F. Wager, and D. A. Keszler, *Aqueous Inorganic Inks for Low-Temperature Fabrication of ZnO TFTs*. Journal of American Chemical Society, 2008. **130**: p. 17603-17609.
- [20] B. J. Norris, J. T. Anderson, J. F. Wager, and D. A. Keszler, *Spin-coated zinc oxide transparent transistors*. Journal of Physics D: Applied Physics, 2003. **36**: p. L105-L107.
- [21] M. Gong, Q. Liu, B. Cook, B. Kattel, T. Wang, W. L. Chan, D. Ewing, M. Casper, A. Stramel, and J. Z. Wu, *All-Printable ZnO Quantum Dots/Graphene van der Waals Heterostructures for Ultrasensitive Detection of Ultraviolet Light*. ACS Nano, 2017. **11**(4): p. 4114-4123.
- [22] L. Filipovic and S. Selberherr, *Performance and stress analysis of metal oxide films for CMOS-integrated gas sensors*. Sensors (Basel), 2015. **15**(4): p. 7206-27.
- [23] N. Hongsoth, E. Wongrat, T. Kerdcharoen, and S. Choopun, *Sensor response formula for sensor based on ZnO nanostructures*. Sensors and Actuators B: Chemical, 2010. **144**(1): p. 67-72.
- [24] A. Janotti and C. G. Van de Walle, *Fundamentals of zinc oxide as a semiconductor*. Reports on Progress in Physics, 2009. **72**(12): p. 126501.
- [25] Y. Dong, Y. Zou, J. Song, J. Li, B. Han, Q. Shan, L. Xu, J. Xue, and H. Zeng, *An all-inkjet-printed flexible UV photodetector*. Nanoscale, 2017. **9**(25): p. 8580-8585.
- [26] S. Goossens, G. Navickaite, C. Monasterio, S. Gupta, J. J. Piqueras, R. Pérez, G. Burwell, I. Nikitskiy, T. Lasanta, T. Galán, E. Puma, A. Centeno, A. Pesquera, A. Zurutuza, G. Konstantatos, and F. Koppens, *Broadband image sensor array based on graphene–CMOS integration*. Nature Photonics, 2017. **11**(6): p. 366-371.

- [27] S. Santra, G. Hu, R. C. Howe, A. De Luca, S. Z. Ali, F. Udrea, J. W. Gardner, S. K. Ray, P. K. Guha, and T. Hasan, *CMOS integration of inkjet-printed graphene for humidity sensing*. Sci Rep, 2015. **5**: p. 17374.
- [28] G. Hassan, J. Bae, A. Hassan, S. Ali, C. H. Lee, and Y. Choi, *Ink-jet printed stretchable strain sensor based on graphene/ZnO composite on micro-random ridged PDMS substrate*. Composites Part A: Applied Science and Manufacturing, 2018. **107**: p. 519-528.
- [29] D. Soltman and V. Subramanian, *Inkjet-Printed Line Morphologies and Temperature Control of the Coffee Ring Effect*. Langmuir, 2008. **24**: p. 2224-2231.
- [30] I. Etxebarria, J. Elizalde, and R. Pacios, *Smart monolithic integration of inkjet printed thermal flow sensors with fast prototyping polymer microfluidics*. Smart Materials and Structures, 2016. **25**(8): p. 085022.
- [31] M. Gao, L. Li, and Y. Song, *Inkjet printing wearable electronic devices*. Journal of Materials Chemistry C, 2017. **5**(12): p. 2971-2993.
- [32] S. Khan, L. Lorenzelli, and R. S. Dahiya, *Technologies for Printing Sensors and Electronics Over Large Flexible Substrates: A Review*. IEEE Sensors Journal, 2015. **15**(6): p. 3164-3185.
- [33] S. Ma, F. Ribeiro, K. Powell, J. Lutian, C. Moller, T. Large, and J. Holbery, *Fabrication of Novel Transparent Touch Sensing Device via Drop-on-Demand Inkjet Printing Technique*. ACS Appl Mater Interfaces, 2015. **7**(39): p. 21628-33.
- [34] G. Mattana and D. Briand, *Recent advances in printed sensors on foil*. Materials Today, 2016. **19**(2): p. 88-99.
- [35] W. Wu, *Inorganic nanomaterials for printed electronics: a review*. Nanoscale, 2017. **9**(22): p. 7342-7372.

- [36] R. F. Hossain, I. G. Deaguero, T. Boland, and A. B. Kaul, *Biocompatible, large-format, inkjet printed heterostructure MoS₂-graphene photodetectors on conformable substrates*. npj 2D Materials and Applications, 2017. **1**(1).
- [37] J. Kukkola, M. Mohl, A.-R. Leino, G. Tóth, M.-C. Wu, A. Shchukarev, A. Popov, J.-P. Mikkola, J. Lauri, M. Riihimäki, J. Lappalainen, H. Jantunen, and K. Kordás, *Inkjet-printed gas sensors: metal decorated WO₃ nanoparticles and their gas sensing properties*. Journal of Materials Chemistry, 2012. **22**(34): p. 17878.
- [38] D. Thuau, K. Kallitsis, F. D. Dos Santos, and G. Hadziioannou, *All inkjet-printed piezoelectric electronic devices: energy generators, sensors and actuators*. Journal of Materials Chemistry C, 2017. **5**(38): p. 9963-9966.
- [39] X. Liu, T.-J. Tarn, F. Huang, and J. Fan, *Recent advances in inkjet printing synthesis of functional metal oxides*. Particuology, 2015. **19**: p. 1-13.
- [40] B. H. Kim, M. S. Onses, J. B. Lim, S. Nam, N. Oh, H. Kim, K. J. Yu, J. W. Lee, J. H. Kim, S. K. Kang, C. H. Lee, J. Lee, J. H. Shin, N. H. Kim, C. Leal, M. Shim, and J. A. Rogers, *High-resolution patterns of quantum dots formed by electrohydrodynamic jet printing for light-emitting diodes*. Nano Lett, 2015. **15**(2): p. 969-73.
- [41] M. Layani, P. Darmawan, W. L. Foo, L. Liu, A. Kamyshny, D. Mandler, S. Magdassi, and P. S. Lee, *Nanostructured electrochromic films by inkjet printing on large area and flexible transparent silver electrodes*. Nanoscale, 2014. **6**(9): p. 4572-6.
- [42] B. Cook, Q. Liu, M. Gong, D. Ewing, M. Casper, A. Stramel, A. Elliot, and J. Wu, *Printing High-Performance Tungsten Oxide Thin Film Ultraviolet Photodetectors on ZnO Quantum Dot Textured SiO₂ Surface*. IEEE Sensors Journal, 2018. **18**(23): p. 9542-9547.

- [43] B. Derby, *Inkjet Printing of Functional and Structural Materials: Fluid Property Requirements, Feature Stability, and Resolution*. Annual Review of Materials Research, 2010. **40**: p. 395-414.
- [44] G. D. Martin, S. D. Hoath, and I. M. Hutchings, *Inkjet printing - the physics of manipulating liquid jets and drops*. Journal of Physics: Conference Series, 2008. **105**: p. 012001.
- [45] B. Derby, *Additive Manufacture of Ceramics Components by Inkjet Printing*. Engineering, 2015. **1**(1): p. 113-123.
- [46] B. Derby, *Inkjet printing ceramics: From drops to solid*. Journal of the European Ceramic Society, 2011. **31**(14): p. 2543-2550.
- [47] J. Bico, U. Thiele, and D. Quéré, *Wetting of textured surfaces*. Colloids and Surfaces: A, 2002. **206**: p. 41-46.
- [48] D. Murakami, H. Jinnai, and A. Takahara, *Wetting transition from the Cassie-Baxter state to the Wenzel state on textured polymer surfaces*. Langmuir, 2014. **30**(8): p. 2061-7.
- [49] S. Suzuki and K. Ueno, *Apparent Contact Angle Calculated from a Water Repellent Model with Pinning Effect*. Langmuir, 2017. **33**(1): p. 138-143.
- [50] G. Wolansky and A. Marmur, *Apparent contact angles on rough surfaces: the Wenzel equation revisited*. Colloids and Surfaces: A, 1999. **156**: p. 381-388.
- [51] M. Gong, Q. Liu, R. Goul, D. Ewing, M. Casper, A. Stramel, A. Elliot, and J. Z. Wu, *Printable Nanocomposite FeS₂-PbS Nanocrystals/Graphene Heterojunction Photodetectors for Broadband Photodetection*. ACS Appl Mater Interfaces, 2017. **9**(33): p. 27801-27808.

- [52] M. Gong, R. Sakidja, Q. Liu, R. Goul, D. Ewing, M. Casper, A. Stramel, A. Elliot, and J. Z. Wu, *Broadband Photodetectors Enabled by Localized Surface Plasmonic Resonance in Doped Iron Pyrite Nanocrystals*. *Advanced Optical Materials*, 2018. **6**(8): p. 1701241.
- [53] B. Cook, M. Gong, D. Ewing, M. Casper, A. Stramel, A. Elliot, and J. Wu, *Inkjet Printing Multicolor Pixelated Quantum Dots on Graphene for Broadband Photodetection*. *ACS Applied Nano Materials*, 2019. **2**(5): p. 3246-3252.
- [54] M. Padmanabhan, R. Meyen, and K. Houghton, *Facile fabrication of ZnO—graphite composite thin films for ultraviolet photodetection*. *Materials Research Express*, 2018. **5**(9): p. 095606.
- [55] Q. Liu, M. Gong, B. Cook, D. Ewing, M. Casper, A. Stramel, and J. Wu, *Transfer-free and printable graphene/ZnO-nanoparticle nanohybrid photodetectors with high performance*. *Journal of Materials Chemistry C*, 2017. **5**(26): p. 6427-6432.
- [56] Q. Nian, L. Gao, Y. Hu, B. Deng, J. Tang, and G. J. Cheng, *Graphene/PbS-Quantum Dots/Graphene Sandwich Structures Enabled by Laser Shock Imprinting for High Performance Photodetectors*. *ACS Appl Mater Interfaces*, 2017. **9**(51): p. 44715-44723.
- [57] B. Cook, Q. Liu, M. Gong, D. Ewing, M. Casper, A. Stramel, and J. Wu, *Quantum Dots-Facilitated Printing of ZnO Nanostructure Photodetectors with Improved Performance*. *ACS Appl Mater Interfaces*, 2017. **9**(27): p. 23189-23194.
- [58] B. Cook, M. Gong, A. Corbin, D. Ewing, A. Tramble, and J. Wu, *Inkjet-Printed Imbedded Graphene Nanoplatelet/Zinc Oxide Bulk Heterojunctions Nanocomposite Films for Ultraviolet Photodetection*. *ACS Omega*, 2019. **4**(27): p. 22497-22503.

- [59] B. Cook, Q. Liu, J. Butler, K. Smith, K. Shi, D. Ewing, M. Casper, A. Stramel, A. Elliot, and J. Wu, *Heat-Assisted Inkjet Printing of Tungsten Oxide for High-Performance Ultraviolet Photodetectors*. ACS Appl Mater Interfaces, 2018. **10**(1): p. 873-879.
- [60] B. Cook, Q. Liu, J. Liu, M. Gong, D. Ewing, M. Casper, A. Stramel, and J. Wu, *Facile zinc oxide nanowire growth on graphene via a hydrothermal floating method: towards Debye length radius nanowires for ultraviolet photodetection*. J. Mater. Chem. C, 2017. **5**(38): p. 10087-10093.
- [61] J. Liu, R. Lu, G. Xu, J. Wu, P. Thapa, and D. Moore, *Development of a Seedless Floating Growth Process in Solution for Synthesis of Crystalline ZnO Micro/Nanowire Arrays on Graphene: Towards High-Performance Nanohybrid Ultraviolet Photodetectors*. Advanced Functional Materials, 2013. **23**(39): p. 4941-4948.
- [62] Q. Liu, M. Gong, B. Cook, D. Ewing, M. Casper, A. Stramel, and J. Wu, *Fused Nanojunctions of Electron-Depleted ZnO Nanoparticles for Extraordinary Performance in Ultraviolet Detection*. Advanced Materials Interfaces, 2017. **4**(6): p. 1601064.
- [63] C.-C. Lin and Y.-Y. Li, *Synthesis of ZnO nanowires by thermal decomposition of zinc acetate dihydrate*. Materials Chemistry and Physics, 2009. **113**(1): p. 334-337.
- [64] Z. Jincheng, S. Chengwu, C. Junjun, Y. Chao, W. Ni, and W. Mao, *Pyrolysis preparation of WO₃ thin films using ammonium metatungstate DMF/Water solution for efficient compact layers in planar perovskite solar cells*. Journal of Semiconductors, 2016. **37**(3): p. 1-5.
- [65] S.-H. Lee, X. H. Nguyen, Y. Gim, and H. S. Ko, *Study on electrohydrodynamic jetting performance of organic solvents*. Journal of Mechanical Science and Technology, 2015. **29**(11): p. 4767-4774.

- [66] H. Ogawa, M. Nishikawa, and A. Abe, *Hall measurement studies and an electrical conduction model of tin oxide ultrafine particle films*. Journal of Applied Physics, 1982. **53**(6): p. 4448-4455.
- [67] A. Rothschild and Y. Komem, *The effect of grain size on the sensitivity of nanocrystalline metal-oxide gas sensors*. Journal of Applied Physics, 2004. **95**(11): p. 6374-6380.
- [68] H. Q. Bian, S. Y. Ma, Z. M. Zhang, J. M. Gao, and H. B. Zhu, *Microstructure and Raman scattering of Ag-doping ZnO films deposited on buffer layers*. Journal of Crystal Growth, 2014. **394**: p. 132-136.
- [69] Y. Huang, M. Liu, Z. Li, Y. Zeng, and S. Liu, *Raman spectroscopy study of ZnO-based ceramic films fabricated by novel sol-gel process*. Materials Science and Engineering B, 2003. **97**: p. 111-116.
- [70] A. Das, S. Pisana, B. Chakraborty, S. Piscanec, S. K. Saha, U. V. Waghmare, K. S. Novoselov, H. R. Krishnamurthy, A. K. Geim, A. C. Ferrari, and A. K. Sood, *Monitoring dopants by Raman scattering in an electrochemically top-gated graphene transistor*. Nat Nanotechnol, 2008. **3**(4): p. 210-5.
- [71] W. X. Wang, S. H. Liang, T. Yu, D. H. Li, Y. B. Li, and X. F. Han, *The study of interaction between graphene and metals by Raman spectroscopy*. Journal of Applied Physics, 2011. **109**(7): p. 07C501.
- [72] Y. Yak and K. Yong, *Controlled Growth of Well-Aligned ZnO Nanorod Array Using a Novel Solution Method*. Journal of Physical Chemistry B, 2005. **109**: p. 19263-19269.
- [73] L. Bokobza, J.-L. Bruneel, and M. Couzi, *Raman Spectra of Carbon-Based Materials (from Graphite to Carbon Black) and of Some Silicone Composites*. C, 2015. **1**(1): p. 77-94.

- [74] Y. S. Ponosov, A. V. Ushakov, and S. V. Streltsov, *Electronic Raman scattering in graphite and single-layer and few-layer graphene*. Physical Review B, 2015. **91**(19).
- [75] K. Rahimi, A. Yazdani, and M. Ahmadi-rad, *Graphene quantum dots enhance UV photoresponsivity and surface-related sensing speed of zinc oxide nanorod thin films*. Materials & Design, 2018. **140**: p. 222-230.
- [76] A. Matavž, R. C. Frunză, A. Drnovšek, V. Bobnar, and B. Malič, *Inkjet printing of uniform dielectric oxide structures from sol–gel inks by adjusting the solvent composition*. Journal of Materials Chemistry C, 2016. **4**(24): p. 5634-5641.
- [77] E. Haro-Poniatowski, M. Jouanne, J. F. Morhange, C. Julien, R. Diamant, M. Fernandez-Guasti, G. A. Fuentes, and J. C. Alonso, *Micro-Raman characterization of WO₃ and MoO₃ thin films obtained by pulsed laser irradiation*. Applied Surface Science, 1988. **127**: p. 674-678.
- [78] I. Moreels, K. Lambert, D. Smeets, D. Muynck, T. Nollet, J. Martins, F. Vanhaecke, A. Vantomme, C. Delerue, G. Allan, and Z. Hens, *Size-Dependent Optical Properties of Colloidal PbS Quantum Dots*. ACS Nano, 2009. **3**: p. 3023-3030.
- [79] J. S. Lee, K. Y. Shin, O. J. Cheong, J. H. Kim, and J. Jang, *Highly sensitive and multifunctional tactile sensor using free-standing ZnO/PVDF thin film with graphene electrodes for pressure and temperature monitoring*. Sci Rep, 2015. **5**: p. 7887.
- [80] V. Quang Dang, D. I. Kim, L. Thai Duy, B. Y. Kim, B. U. Hwang, M. Jang, K. S. Shin, S. W. Kim, and N. E. Lee, *Piezoelectric coupling in a field-effect transistor with a nanohybrid channel of ZnO nanorods grown vertically on graphene*. Nanoscale, 2014. **6**(24): p. 15144-50.

- [81] N. Yogeswaran, W. T. Navaraj, S. Gupta, F. Liu, V. Vinciguerra, L. Lorenzelli, and R. Dahiya, *Piezoelectric graphene field effect transistor pressure sensors for tactile sensing*. Applied Physics Letters, 2018. **113**(1): p. 014102.
- [82] T. Lee, W. Lee, S.-W. Kim, J. J. Kim, and B.-S. Kim, *Flexible Textile Strain Wireless Sensor Functionalized with Hybrid Carbon Nanomaterials Supported ZnO Nanowires with Controlled Aspect Ratio*. Advanced Functional Materials, 2016. **26**(34): p. 6206-6214.
- [83] S. Chun, Y. Choi, and W. Park, *All-graphene strain sensor on soft substrate*. Carbon, 2017. **116**: p. 753-759.
- [84] H. Gullapalli, V. S. Vemuru, A. Kumar, A. Botello-Mendez, R. Vajtai, M. Terrones, S. Nagarajaiah, and P. M. Ajayan, *Flexible piezoelectric ZnO-paper nanocomposite strain sensor*. Small, 2010. **6**(15): p. 1641-6.
- [85] S. Goniszewski, M. Adabi, O. Shaforost, S. M. Hanham, L. Hao, and N. Klein, *Correlation of p-doping in CVD Graphene with Substrate Surface Charges*. Sci Rep, 2016. **6**: p. 22858.
- [86] Y. Li, J. K. Cooper, W. Liu, C. M. Sutter-Fella, M. Amani, J. W. Beeman, A. Javey, J. W. Ager, Y. Liu, F. M. Toma, and I. D. Sharp, *Defective TiO₂ with high photoconductive gain for efficient and stable planar heterojunction perovskite solar cells*. Nat Commun, 2016. **7**: p. 12446.
- [87] V. Lordi, P. Erhart, and D. Åberg, *Charge carrier scattering by defects in semiconductors*. Physical Review B, 2010. **81**(23).
- [88] K. Huang, Q. Zhang, F. Yang, and D. He, *Ultraviolet photoconductance of a single hexagonal WO₃ nanowire*. Nano Research, 2010. **3**(4): p. 281-287.

- [89] G. Konstantatos, L. Levina, A. Fischer, and E. H. Sargent, *Engineering the temporal response of photoconductive photodetectors via selective introduction of surface trap states*. Nano Lett, 2008. **8**(5): p. 1446-50.
- [90] Z. Hai, M. K. Akbari, C. Xue, H. Xu, L. Hyde, and S. Zhuiykov, *Wafer-scaled monolayer WO₃ windows ultra-sensitive, extremely-fast and stable UV-A photodetection*. Applied Surface Science, 2017. **405**: p. 169-177.
- [91] Y. M. Juan, S. J. Chang, H. T. Hsueh, T. C. Chen, S. W. Huang, Y. H. Lee, T. J. Hsueh, and C. L. Wu, *Self-powered hybrid humidity sensor and dual-band UV photodetector fabricated on back-contact photovoltaic cell*. Sensors and Actuators B: Chemical, 2015. **219**: p. 43-49.
- [92] P. P. González-Borrero, F. Sato, A. N. Medina, M. L. Baesso, A. C. Bento, G. Baldissera, C. Persson, G. A. Niklasson, C. G. Granqvist, and A. Ferreira da Silva, *Optical band-gap determination of nanostructured WO₃ film*. Applied Physics Letters, 2010. **96**(6): p. 061909.
- [93] G. Konstantatos, M. Badioli, L. Gaudreau, J. Osmond, M. Bernechea, F. P. Garcia de Arquer, F. Gatti, and F. H. L. Koppens, *Hybrid graphene-quantum dot phototransistors with ultrahigh gain*. Nature Nanotechnology, 2012. **7**: p. 363-368.
- [94] Z. Sun, Z. Liu, J. Li, G.-a. Tai, S.-P. Lau, and F. Yan, *Infrared Photodetectors Based on CVD-Grown Graphene and PbS Quantum Dots with Ultrahigh Responsivity*. Advanced Materials, 2012. **24**: p. 5878-5883.
- [95] D. Zhang, L. Gan, Y. Cao, Q. Wang, L. Qi, and X. Guo, *Understanding Charge Transfer at PbS-Decorated Graphene Surfaces toward a Tunable Photosensor*. Advanced Materials, 2012. **24**: p. 2715-2720.

- [96] W. Guo, S. Xu, Z. Wu, N. Wang, M. M. T. Loy, and S. Du, *Oxygen-Assisted Charge Transfer Between ZnO Quantum Dots and Graphene*. *Small*, 2013. **9**: p. 3031-3036.
- [97] Q. Liu, B. Cook, K. Shi, J. Butler, K. Smith, M. Gong, D. Ewing, M. Casper, A. Stramel, A. Elliot, and J. Wu, *Interface Nanojunction Engineering of Electron-Depleted Tungsten Oxide Nanoparticles for High-Performance Ultraviolet Photodetection*. *ACS Applied Nano Materials*, 2017. **1**(1): p. 394-400.